

Experimental and Theoretical Studies on Two-Phase Flows

Thesis by

Christopher James Koh

in Partial Fulfillment of the Requirements
for the Degree of
Doctor of Philosophy

California Institute of Technology
Pasadena, California

1991

(Submitted February 4, 1991)

To Mom and Judy



Acknowledgement

THANK YOU! to all of you who deserve more than mere words of appreciation; for without you, this journey could never have been accompanied by so many delightful[†] moments...

Specifically, I would like to express my sincere gratitude

to Professor Gary Leal, for allowing me to meander through the *no man's land* of research while providing enough guidance so that I emerge as a more independent (and hopefully better) researcher

to Drs. Enrique Geffroy-Aguilar, In Seok Kang, Dave Mead and Moshe Shapira, for their many insightful discussions (scientific and otherwise)

to Dr. Phil Hookham, for initiating the LDA suspension experiment

to Chic Nakawatase, Floyd Litreal, Tony Stark and Ray Garcia, master craftsmen

to Kathy, for taking care of things at Caltech while I am in Santa Barbara

to Chak, Ricky(world class athlete), Thu(poet, Buddhist, philosopher), Ken(the crazy guy), Alex, Art, Chuan, Bill, Sitaram and Dmitri(“πρυBem, another backgammon game?”)

to T.K. and his gang

and above all, to Judy, for her patience, understanding, support and love

[†]Okay, and may be some not so delightful ones.

Abstract

This thesis, comprised of two parts, deals with the flow of suspensions. Part I concerns specifically with the stability of a single drop translating through a quiescent, unbounded suspending fluid at low Reynolds number. The evolution of the shape of an initially nonspherical drop as it translates is studied numerically and experimentally. For finite capillary numbers, it is shown that the drop reverts to a sphere provided that the initial deformation is small enough. However, beyond certain critical initial deformation, the drop deforms continuously. For initially prolate shapes, the drop elongates with the formation of a tail; for initially oblate shapes, the drop flattens with the formation of a cavity at its rear. Experiments extend the numerical results. It is found that initially unstable prolate drops break up into multiple droplets, while initially unstable oblate drops deform in double-emulsion drops.

Part II of this thesis considers the flow of high concentration solid suspensions through a rectangular channel. By adapting the well-known Laser Doppler Anemometry, an experimental technique is developed to measure the velocity as well as particle volume fraction of the suspension. A crucial element in these experiments is the reduction of the optical turbidity of the suspension. To accomplish this goal, a systematic method based on refractive-index-matching of the two phases is employed. Experimental results show that the velocity profile is blunted while the concentration profile has a maximum near the center. The qualitative features of the experimental data compare reasonably well with theoretical predictions based on the shear-induced particle migration theory.

Contents

Dedication	ii
Acknowledgement	iii
Abstract	iv
I The Stability of Drop Shapes in Creeping Flow	1
1 The Stability of Drop Shapes for Translation at Zero Reynolds Number through a Quiescent Fluid—Numerical Simulation	2
1.1 Introduction	5
1.2 Problem Formulation	6
1.3 Results	7
References	13
Figures	16
Appendix A	27
2 An Experimental Investigation on the Stability of Viscous Drops Translating through a Quiescent Fluid	34
2.1 Introduction	37
2.2 Experimental Procedure	38
2.3 Results	40
References	44
Figures	47
Table	59

II	Flow of Concentrated Suspensions	60
3	An Experimental Investigation of Concentrated Suspension Flows in a Rectangular Channel	61
3.1	Introduction	64
3.2	Experimental Technique	70
3.2.1	Refractive Index Match	71
3.3	Experimental Setup	76
3.3.1	Calculation of average particle velocity and volume fraction .	79
3.3.2	Test of experimental system	80
3.4	Experimental Procedure	82
3.5	Experimental Results and Discussion	83
3.6	Comparison with theory	89
	References	93
	Tables	123
	Appendix A	125
	Appendix B	132
	Appendix C	133
	Appendix D	136
	Appendix E	140
	Appendix F	162
4	Thesis Summary	169

Part I

The Stability of Drop Shapes in Creeping Flow

Chapter 1

The Stability of Drop Shapes for Translation at Zero Reynolds Number through a Quiescent Fluid—Numerical Simulation

The Stability of Drop Shapes for Translation at Zero Reynolds Number through a Quiescent Fluid—Numerical Simulation¹

Christopher J. Koh²
California Institute of Technology
Department of Chemical Engineering

and

L. Gary Leal³
University of California, Santa Barbara
Department of Chemical and Nuclear Engineering

¹The basic text in this chapter consists of an article which appeared in *Phys. Fluid A*, 1 No.8, 1309(1989).

²California Institute of Technology, Chemical Engineering, mail code 210-41, 1201 E. California Blvd., Pasadena, CA 91125, USA.

³To whom correspondence should be addressed: University of California, Chemical and Nuclear Engineering Dept., Santa Barbara, CA 93106, USA. Tel:(805)893-8510, Fax:(805)893-4731.

The Stability of Drop Shapes for Translation at Zero Reynolds Number through a Quiescent Fluid—Numerical Simulation

Abstract

Boundary integral calculations are used to investigate the evolution of the shape of an initially nonspherical drop that translates at zero Reynolds number through a quiescent, unbounded fluid. For finite capillary numbers, it is shown that the drop reverts to a sphere, provided the initial deformation is not too large. However, drops that are initially deformed to a greater extent are shown to deform continuously, forming an elongated shape with a tail when initially prolate, and a flattened shape with a cavity at the rear when initially oblate. The critical degree of deformation decreases as the capillary number increases and appears to be consistent with the results of Kojima, *et al.* (1984) who showed that the spherical drop is unstable to infinitesimal disturbances in the limit $Ca \equiv \infty$.

Chapter 1

The Stability of Drop Shapes for Translation at Zero Reynolds Number through a Quiescent Fluid—Numerical Simulation

1.1 Introduction

The motion of a viscous drop translating under the action of buoyancy through an unbounded and otherwise quiescent fluid is a classical problem with a very long history in fluid mechanics. Besides being a fundamentally important problem, the dynamics of viscous drops also provide us with a framework for studying the deformation of biological cells as well as the behavior of aggregates of small particles. A solution in the creeping flow limit was obtained many years ago, attributed to Hadamard[1] and Rybczynski[2], and based upon the assumption that the shape is spherical. Later, Taylor and Acrivos[3] considered small inertia effects and showed that the drop deforms slightly to an oblate ellipsoid shape for small Reynolds number, but that the sphere is an exact steady solution for arbitrary Capillary number (Ca) in the limit $Re \equiv 0$. The Capillary number is the ratio of the viscous force compared to the interfacial tension and is defined as

$$Ca \equiv \frac{u_c \nu a}{\sigma} \quad (1.1)$$

where a is the equivalent radius of the drop, σ is the interfacial tension, and ν is the kinematic viscosity of the ambient fluid. u_c is the translational velocity of a

spherical drop of the same volume, *i.e.*,

$$u_c = \frac{1}{3} \frac{a^2 g}{\nu_2} \left| \frac{\rho_1}{\rho_2} - 1 \right| \left(\frac{1 + \lambda}{1 + \frac{3}{2\lambda}} \right) \quad (1.2)$$

The stability of the steady, spherical shape to infinitesimal disturbances of shape was studied more recently by Kojima, *et al.*[4]. These authors showed that the sphere was a stable solution for arbitrarily small disturbances of shape for all finite capillary number, but was unstable in the limit $Ca \equiv \infty$. The instability was predicted to appear at the rear of the drop as a growing tail for an initially prolate shape, and as a growing indentation or cavity for an initially oblate shape, with a characteristic growth rate that scales as $(1 + \lambda)^{-1}$ with changes in the viscosity ratio λ (*i.e.*, $\lambda \equiv \mu_{\text{drop}}/\mu_{\text{suspending fluid}}$). In contrast, the magnitude of the initial disturbance at the front of the drop was predicted by the linear theory to decay rapidly to zero, so that the front of the drop returns rapidly to hemispherical shape. The obvious question that we pursue here is whether the *stability* of the spherical shape for nonzero capillary numbers carries over to *finite* initial deformations.

This investigation is based upon numerical solutions of the free boundary, creeping flow problem of an initially deformed drop rising through a quiescent fluid, using the well-known boundary-integral method. For brevity's sake, the details regarding the implementation of this technique can be found in Appendix A. We will simply pose the problem and describe the results, with only a few remarks to establish those details of the simulation that would be necessary to reproduce the results that are reported here (*e.g.*, the number of surface elements in the discretization).

1.2 Problem Formulation

We consider the translational motion of a viscous drop through an unbounded and otherwise quiescent fluid in the creeping flow approximation. The two fluids are Newtonian, immiscible, and the interface is characterized by a finite and constant interfacial tension. Thus, the governing equations and boundary conditions are

$$0 = -\nabla p_1 + \nabla^2 \mathbf{u}_1 \quad (1.3)$$

$$0 = -\nabla p_2 + \nabla^2 \mathbf{u}_2 \quad (1.4)$$

$$\mathbf{u}_2 \rightarrow 0 \quad \text{as} \quad \|\mathbf{x}\| \rightarrow \infty \quad (1.5)$$

$$\mathbf{u}_1 = \mathbf{u}_2 \quad \text{at drop interface} \quad (1.6)$$

$$\lambda \mathbf{n} \cdot \mathbf{T}_1 - \mathbf{n} \cdot \mathbf{T}_2 = -\frac{\mathbf{n}}{\text{Ca}} \nabla \cdot \mathbf{n} - \mathbf{n} z \frac{3(1 + \frac{3}{2\lambda})}{1 + \lambda} \quad \text{at drop interface} \quad (1.7)$$

(subscript 1 denotes the drop phase, and 2 denotes the suspending phase) where we have non-dimensionalized the velocity with respect to u_c . The stresses are non-dimensionalized with respect to $\mu_1 u_c/a$ in Fluid 1 and $\mu_2 u_c/a$ in Fluid 2.

In the present study, the shape of the drop is specified initially as nonspherical, and we are interested in calculating the evolution of drop shapes as a function of time after the initial moment. The drop is assumed to translate under the action of a constant body force. Hence, as the shape of the drop changes, the translational velocity changes in accord with the change in hydrodynamic mobility. Our present interest is to determine whether the shape of an initially nonspherical drop returns to a sphere or deforms further as a function of time. In the latter case, we say that the initial drop shape is unstable.

The problem formulated above is solved by the boundary-integral method through numerical implementation. As stated earlier, the details of the numerical simulation can be found in Appendix A. In this present work, we typically use 50 ring-shaped elements on the surface of the drop which is axisymmetric in shape, but this number is varied depending upon the evolution of shapes and the need for adequate resolution in regions of large curvature.

1.3 Results

First of all, in order to check the numerical code, we compute the velocity of a rising spherical drop and compare the results with the Hadarmard-Rybczynski solution. Typically, the computed velocity of each of the surface elements is at least within 0.05% of the exact solution when the surface of the drop is divided into 50 elements.

Specifically, this accuracy is attained for the cases of $\lambda = 0.1$, 1.0 , and 5.0 and is improved when using more surface elements.

In the present study, our primary objective is an investigation of the evolution of drop shapes as a function of the degree of initial deformation for a number of fixed, nonzero values of the capillary number, Ca . The initial shape of the drop is characterized by the parameter Δ defined as

$$\Delta \equiv (L - B)/(L + B) \quad (1.8)$$

As shown in Figure 1.1, L corresponds to the length along the axis of rotation of the ellipsoid, and B to the breadth in the perpendicular direction. Using this definition, Δ ranges from -1 to 1 ; specifically, a prolate ellipsoid has a positive Δ value while an oblate ellipsoid has a negative Δ value. A set of typical results is shown in Figure 1.2 for a fixed initial shape, $\Delta = 1/3$, $\lambda = 0.5$, and various Ca . The drop shapes are shown at several specific points in time (non-dimensionalized by a/u_c). The position of the drop is incremented in the figure by the exact amount of its numerically calculated displacement.

What we can see, qualitatively, from Figure 1.2 is that the drop returns to a steady spherical shape for $Ca \leq 1.25$; but for this initial shape, the initial deformation increases for $Ca \geq 1.5$ continuously in time, with the front of the drop returning to a hemispherical shape, while the rear of the drop develops a tail which increases in length as a function of time. Eventually, in the cases shown in Figure 1.2, the tail begins to pinch and it appears likely that the drop will break as the tail separates from the main parent drop (though, of course, the boundary-integral method can only be pushed to a very thin neck, but cannot be carried to the point of actual pinch-off). Thus, for $\lambda = 0.5$ and $\Delta = 1/3$, Ca_{crit} lies between 1.25 and 1.5 .

If we consider other values of Δ , similar results are obtained. In particular, solutions for initially prolate shapes are shown in Figure 1.3 for $\Delta = 1/21$, and $\lambda = 0.5$, and Figure 1.4 for $\Delta = 0.6$ and $\lambda = 0.5$. Again, we see that for small enough Ca ,

the drop returns to a steady spherical shape, but above some critical value of Ca the drop develops an increasingly elongated tail with increase of time. Comparison of Figures 1.1, 1.3 and 1.4 shows, however, that the critical Ca for instability increases as Δ is decreased. This would seem qualitatively consistent with the prediction from linear stability theory that the drop is unstable to infinitesimal disturbances for $Ca = \infty$, but is stable to such disturbances for finite values of Ca . It may also be noted that the present predictions for finite Ca are qualitatively similar to the linear stability theory for $Ca = \infty$, in the sense that the initially prolate shape is predicted, for $Ca > Ca_{crit}$, to develop a tail at the rear and a hemispherical shape at the front.

We have also carried out a similar investigation of the magnitude of initial deformation for a series of oblate initial shapes for several fixed values of the capillary number. Typical numerical results for this series of numerical experiments is represented in Figure 1.5. Qualitatively, the stability behavior is similar to that demonstrated above for initially prolate shapes. Specifically, for each nonzero capillary number, there is a critical initial deformation beyond which the drop shape is unstable in the sense that the drop does not return to a spherical steady-state shape, but continues to deform with increase in time. As in the case of prolate initial shapes, we see that as the degree of initial deformation increases, Ca_{crit} decreases. However, instead of a tail, the initially oblate shape develops a cavity at the rear. As before, the front of the drop rapidly reverts to a hemispherical shape for all of the initial conditions that we have considered.

It may be noted that the formation of a cavity from an initially oblate shape is again qualitatively consistent with the predictions of the linear stability theory. In fact, a comparison of the solution given by Kojima, *et al.*[4] ($\lambda = 5$, $Ca = \infty$) and our numerical solution ($\lambda = 5$, $Ca = 100$) is shown in Figure 1.6. We can see that the evolutions of the drop shape are very similar, especially in the earlier stage of the simulation. The difference is attributed to different Ca and their assumption of small deviation from sphericity.

Several other details of the problem described above can be examined easily via the boundary-integral technique. One factor that we have considered is the role of the viscosity ratio λ . We illustrate one representative case in Figure 1.7, where we show results for a fixed value of $\Delta = 1/3$ and a fixed $\text{Ca} = 2.0$, but two values of $\lambda = 0.5$ and 5.0 , respectively. The results shown in Figure 1.7 are not plotted at equal values of time, t , as in the previous figures, but at equal values of $\bar{t} \equiv t/(1 + \lambda)$, which is the scaling with λ that is suggested by the linear stability analysis. We see that the results are initially almost identical, thus corroborating the prediction from the linear theory that the viscosity ratio enters primarily via the time scale of deformation. Not surprisingly, however, for large times and large deformations, there are modest qualitative differences for the two values of λ .

A second point that we consider via the numerical results shown in Figure 1.8 is the robustness of the behavior described above to variation in the details of the initial shape. In the results illustrated here, we show the time-dependent evolution of drop shape for two quite dramatically different initial conditions, *i.e.*,

$$r_s^{(1)} = 1 - 0.285P_2(\cos\theta) \quad (1.9)$$

and

$$r_s^{(2)} = 1 - 0.5P_2(\cos\theta) - 0.176P_3(\cos\theta) \quad (1.10)$$

where the P_n are the Legendre polynomials. The drop in the latter case has a very pronounced initial indentation on the front surface, though it is still globally oblate. The numerical solution shows that this indentation rapidly decays and the upper surface of the drop again reverts to a hemisphere. Beyond this, there is continued cavity growth at the rear of the drop which is very similar to that obtained in the absence of the initial deformation.

One other interesting feature which appears for at least one case, when the drop develops a very elongated tail, is the appearance of a capillary wave instability that will presumably cause the tail to break into a large number of roughly equal-sized satellite drops. This phenomena is illustrated in Figure 1.9, where we show the

continuation of the case $Ca = 2.0$, $\Delta = 1/3$ and $\lambda = 5.0$ (shown in Figure 1.7) for larger times. It is well to note that this phenomenon was not observed for the deformation of prolate drops at lower viscosity ratios (*i.e.*, $\lambda = 0.1$ and $\lambda = 0.5$).

Evidently, the breakup of an initially unstable, prolate-shaped drop will occur by one of two possible mechanisms. When the drop is not very viscous, the tail thins dramatically at one point directly behind the parent drop, and we infer that pinch-off will occur in these cases in such a way that the drop breaks into two parts: the parent and a single satellite. On the other hand, as the tail elongates for a very viscous drop, pinch-off at a point is inhibited. As the drop continues to rise, it elongates and thins out more or less uniformly along the whole tail at the same time. Meanwhile, the amplitude of the capillary waves become finite which eventually leads to breakup. This transition from pinch-off of the tail at a single point, to pinch-off at many points due to finite amplitude capillary waves, is highly analogous to the transition in breakup modes for an elongated drop in a quiescent fluid from end pinching in which a drop breaks by a sequence of single pinch-off at the ends of the drop, to a capillary wave breakup mechanism when the drop is more highly elongated (Stone and Leal[5]).

As it turns out, wave-like behavior is also present in the deformation of initially oblate drops. Although we have not made a comprehensive study, it is apparent, at least for the cases we studied, that viscous drops are less susceptible to the development of wavy shapes. Figure 1.10 compares the deformation of two drops with the same initial shape and capillary number, but different viscosity ratios. We can see that the wavy structure is quite pronounced for the less viscous drop but virtually nonexistent for the more viscous one. We should note that the development of these "waves" does not alter the overall qualitative behavior of the development of a cavity at the rear of the drops.

As stated initially, the primary objective of the study reported here is to establish the conditions for instability of an initially nonspherical drop at finite capillary number. The results reported above are summarized in Figure 1.11. Here, we plot

the lower and upper bounds of the critical value of Ca for several fixed values of Δ . Results for three different λ values, namely 0.1, 0.5 and 5.0, are reported for both prolate and oblate initial shapes. There are several features that can be extracted from this figure. First, we can see that for the same initial shape, a more viscous prolate drop is more stable than a less viscous one (*i.e.*, it has a higher Ca_{crit}). However, the contrary is true for initially oblate drops. Second, it is apparent that the dependence of the Ca_{crit} on λ is much smaller for prolate drops than for the oblate ones. Finally, this plot reemphasizes the point made earlier that drops at nonzero Ca can be unstable to finite initial deformations; the deformation grows when Ca exceeds the critical value of Ca , and Ca_{crit} increases monotonically as Δ is decreased. This behavior seems qualitatively consistent with the predicted linear instability for the limit $Ca \rightarrow \infty$.

Acknowledgment: This work was supported by a grant from the Fluid Mechanics Program of the National Science Foundation. C.J.K. wishes to thank Dr. I. S. Kang for his helpful comments and discussion.

Bibliography

- [1] J.S. Hadamard; *CR Acad. Sci.*, **152**,1735(1911).
- [2] W. Rybczynski; *Bull. Acad. Sci. Cracovi*, **A**,40(1911).
- [3] T.D. Taylor and A. Acrivos; *J. Fluid Mech.*, **18**,466(1964).
- [4] M. Kojima, E.J. Hinch and A. Acrivos; *Phys. Fluids*, **27**,19(1984).
- [5] H.A. Stone and L.G. Leal; *J. Fluid Mech.*, **198**,399(1989).

Figure Captions

1. Sketch showing the definition of Δ .
2. Evolution of prolate drops with same initial shapes but different Ca. Time between intermediate shapes = 2.0.
3. Evolution of prolate drops with same initial shapes but different Ca. Time between intermediate shapes = 2.0.
4. Evolution of prolate drops with same initial shapes but different Ca. Time between intermediate shapes = 2.0.
5. Evolution of oblate drops with same initial shapes but different Ca. Time between intermediate shapes = 2.0.
6. Comparison of the present work with the results of Kojima, *et al.*
7. Using the scaling $\bar{t} \equiv t/(1 + \lambda)$ as suggested by the linear stability analysis, the drop shapes are almost identical, especially during the initial stage of the deformation.
8. Comparison of two different initial conditions to show the robustness of the drop evolution to variation in the details of the initial shape. Time between intermediate shapes = 3.0.
9. Development of capillary waves on an elongated tail.
10. Wavy structure is apparent on the less viscous drop ($\lambda = 0.5$) but the contrary on the more viscous drop ($\lambda = 5.0$). Note that the positions of the drops do *not* correspond to the exact amount of the numerically calculated displacement.

11. Ca_{crit} vs. Δ for both oblate and prolate drops. The symbols represent the lower and upper bounds of Ca_{crit} . The lines do *not* correspond to the exact value of Ca_{crit} but are drawn to show the trend.

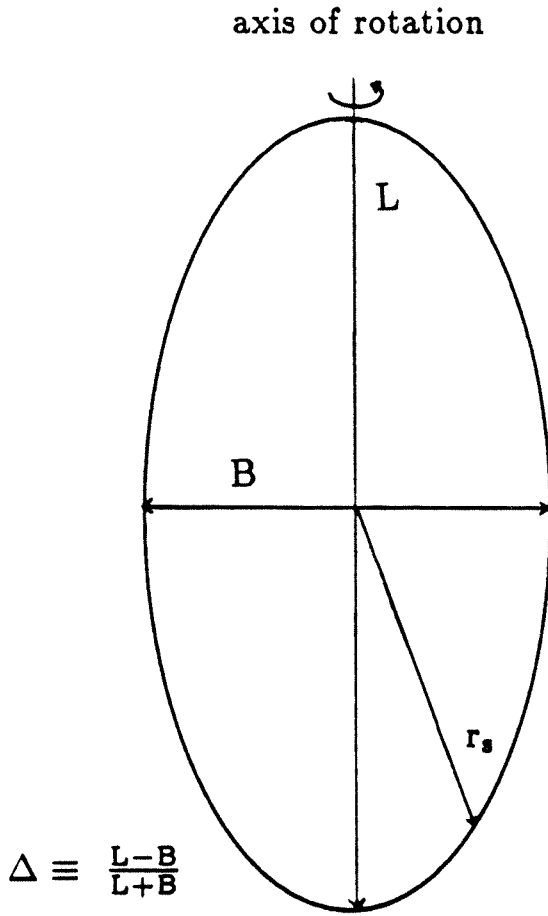
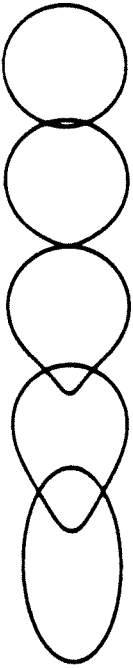


Figure 1.1

Ca=1.25

t = 8.0



t=0

Ca = 1.5

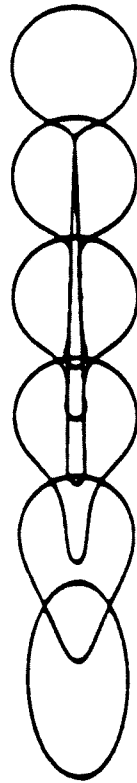
t=8.2



t=0

Ca = 2.0

t=9.8

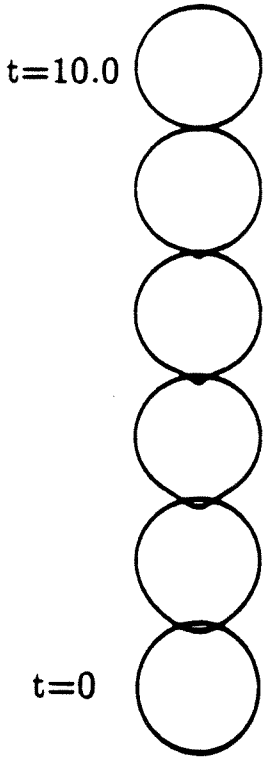
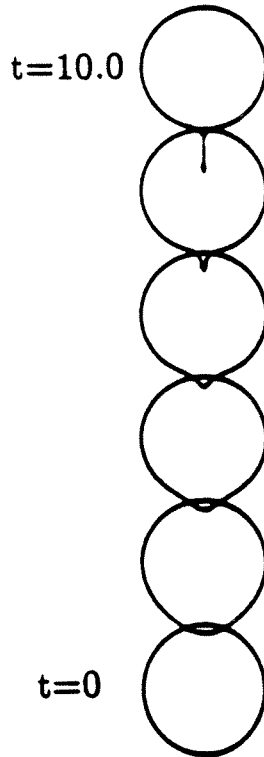
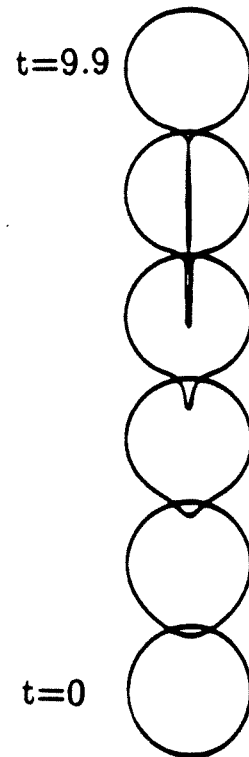


t=0

$$\lambda = 0.5$$

$$\Delta \equiv \frac{L-B}{L+B} = \frac{1}{3}$$

Figure 1.2

$Ca = 4.5$  $Ca = 5.0$  $Ca = 8.0$ 

$$\lambda = 0.5$$

$$\Delta \equiv \frac{L-B}{L+B} = \frac{1}{21}$$

Figure 1.3

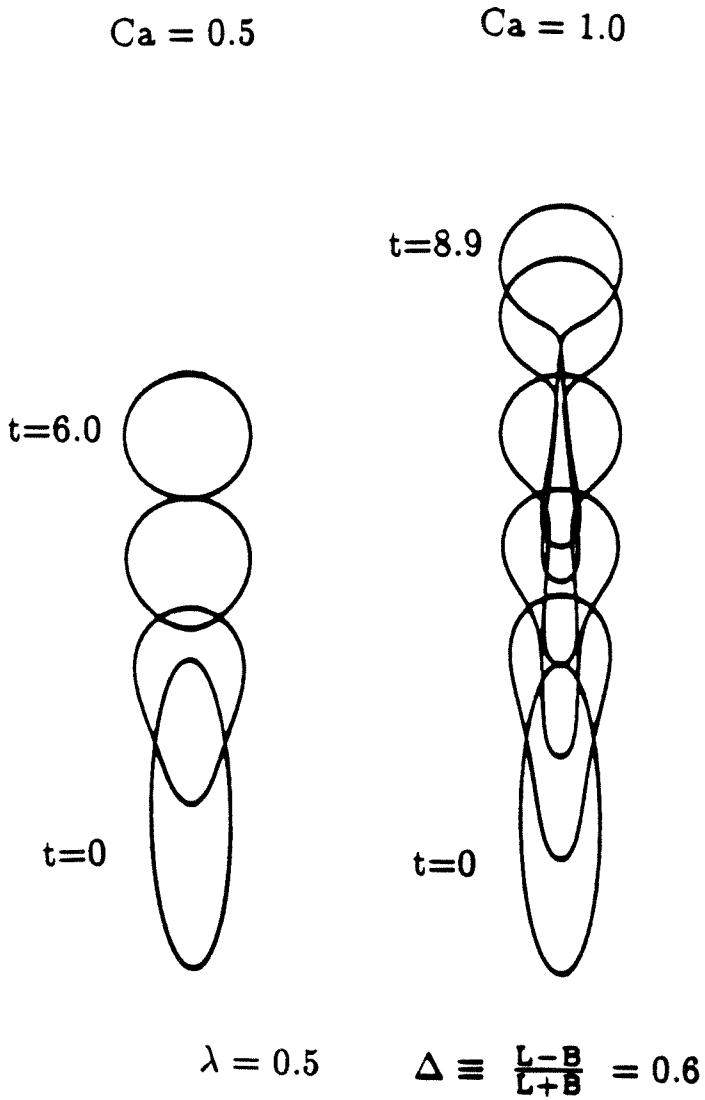


Figure 1.4

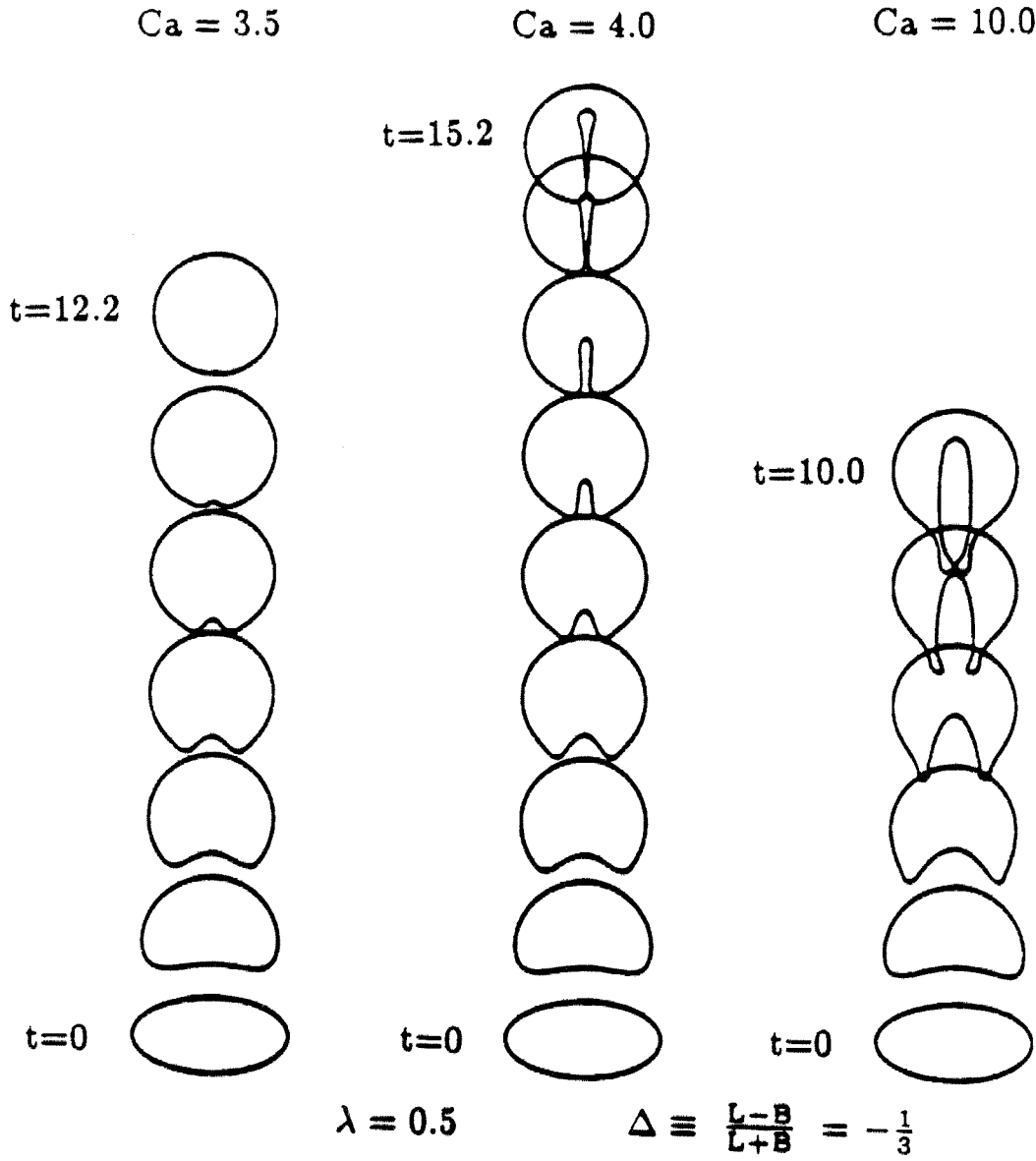


Figure 1.5

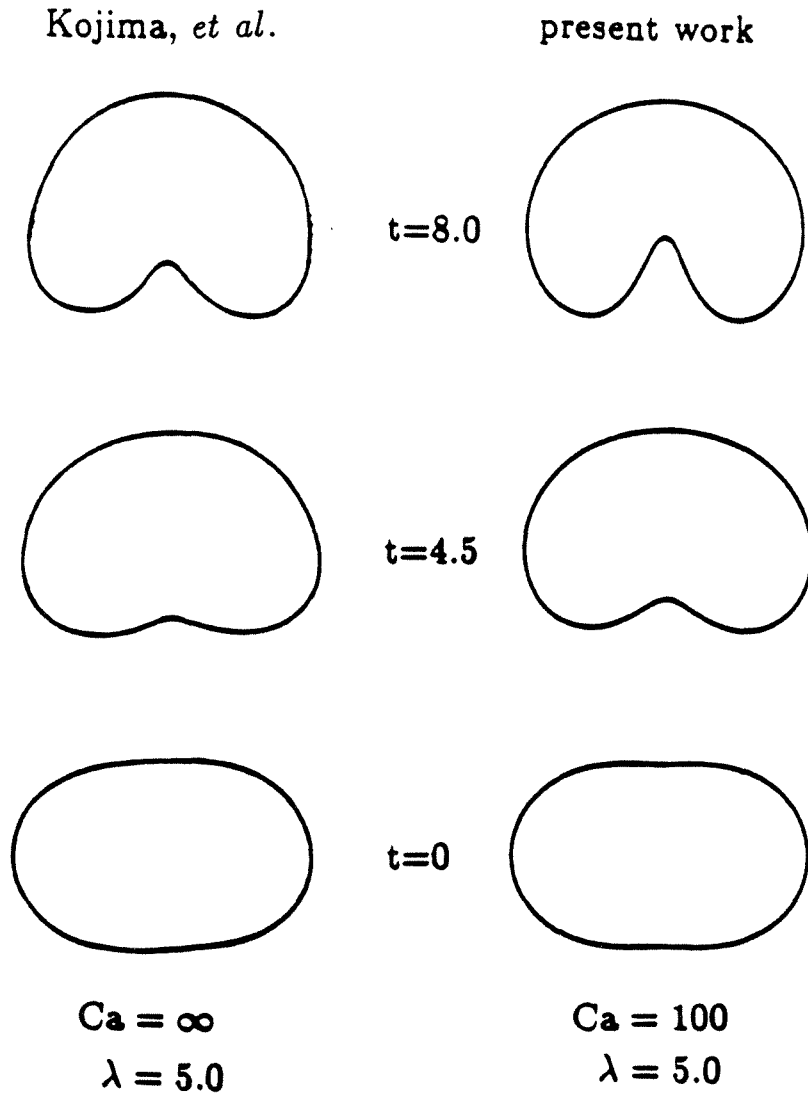


Figure 1.6

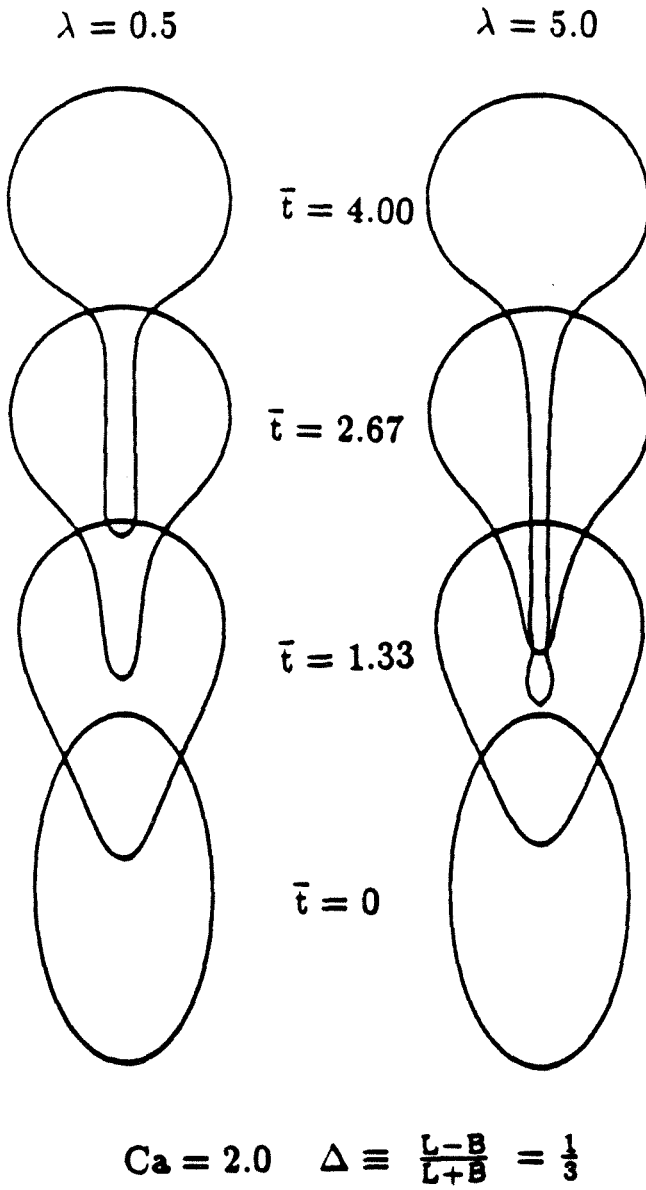


Figure 1.7

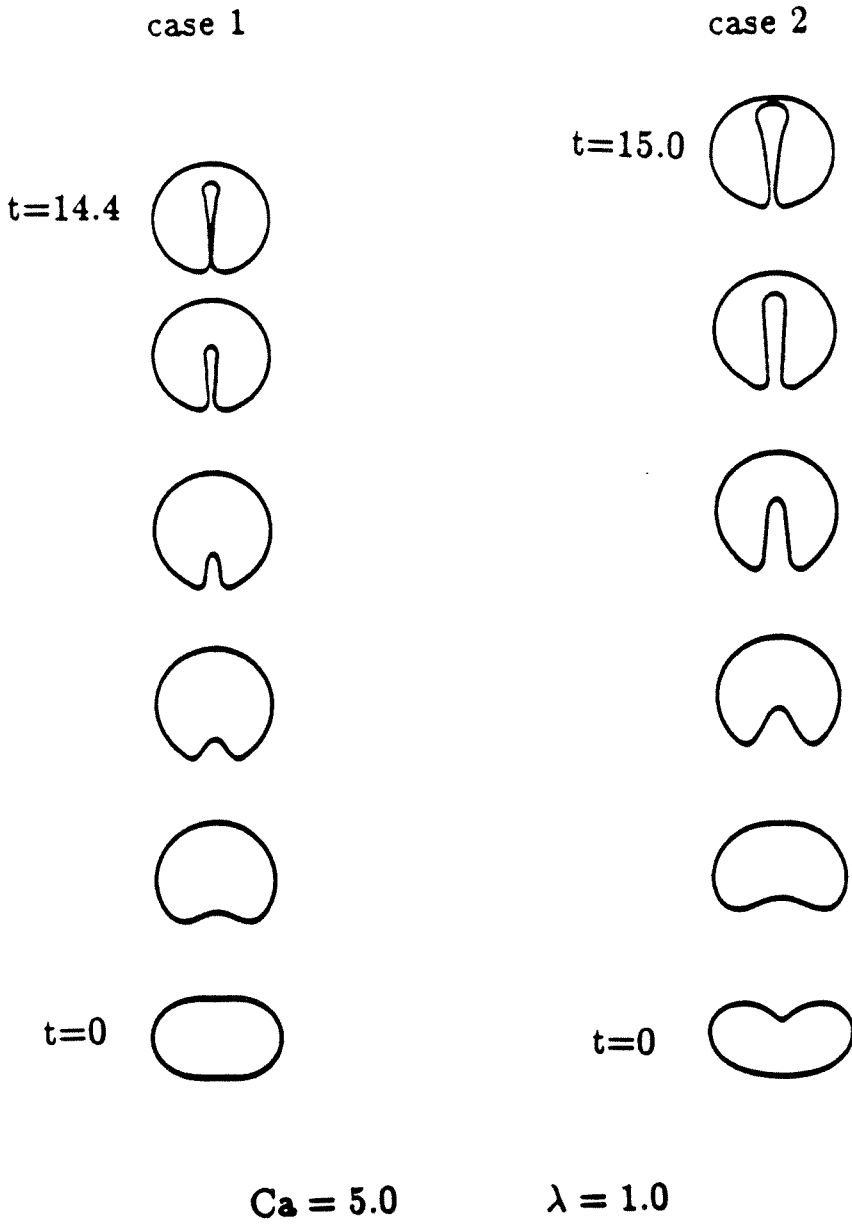


Figure 1.8

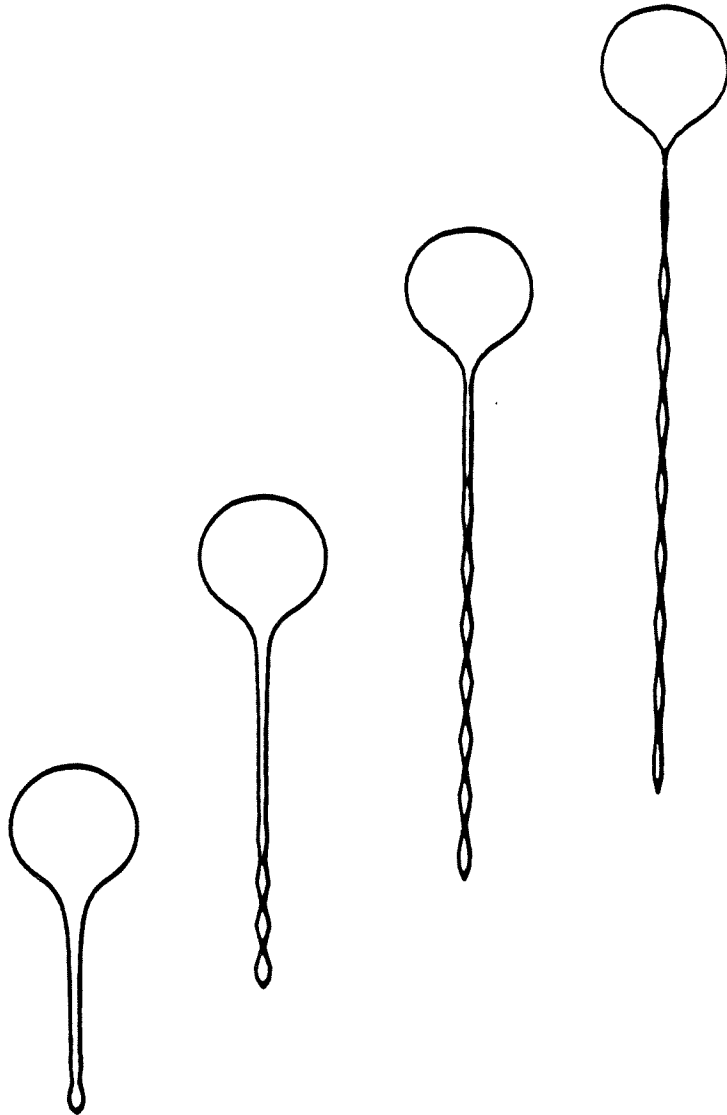
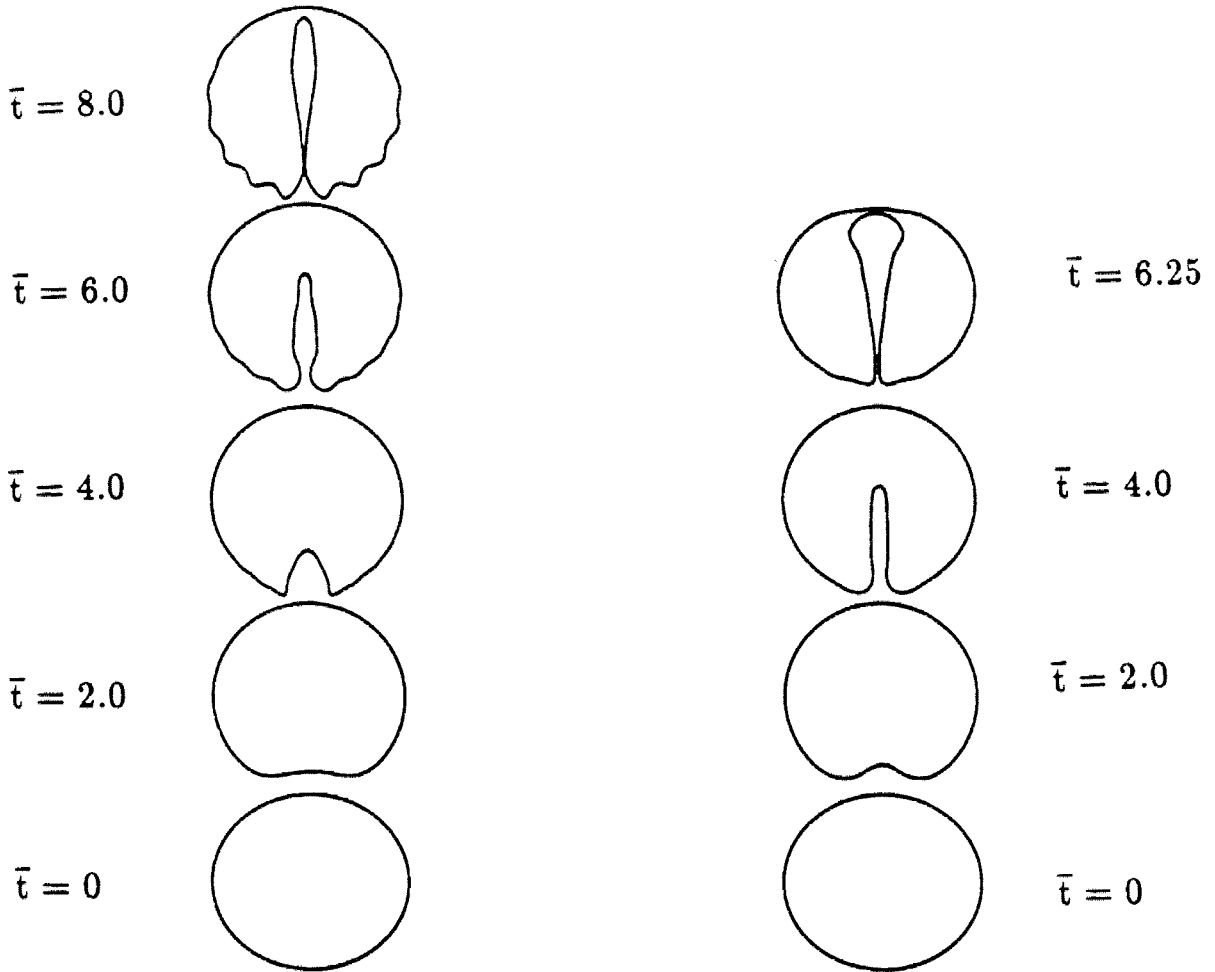
$t=24.0$ $t=28.0$ $t=32.0$ $t=35.2$  $\lambda = 5.0$ $Ca = 2.0$

Figure 1.9

$\lambda = 0.5$ $\lambda = 5.0$ 

$$\Delta \equiv \frac{L-B}{L+B} = -\frac{1}{21} \quad \text{Ca}=100.0$$

Figure 1.10

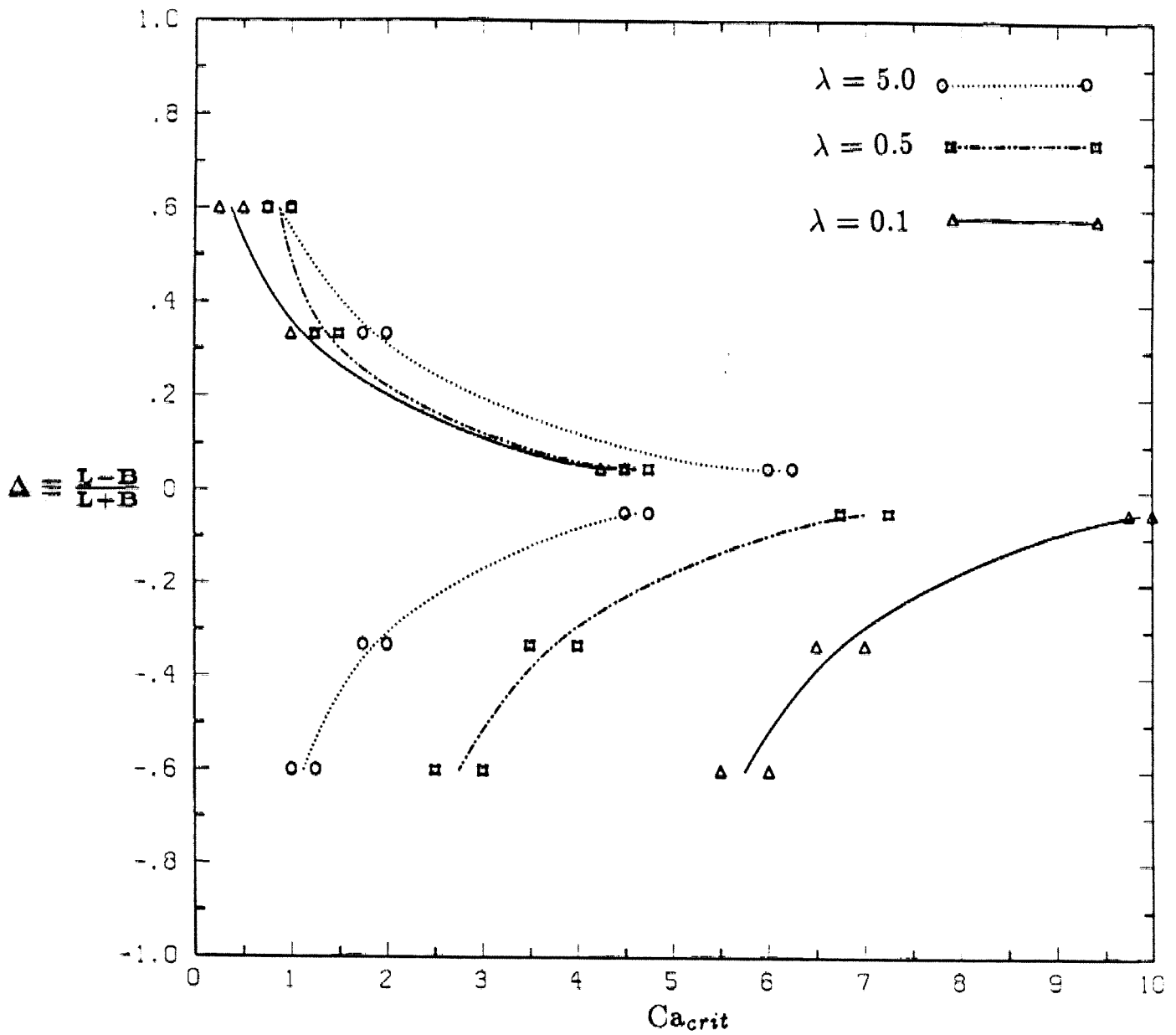


Figure 1.11

Appendix A

In this appendix, we will discuss the details of the implementation of the boundary-integral method for the drop stability problem. We begin by stating the governing equations and boundary conditions:

$$0 = -\nabla p_1 + \nabla^2 \mathbf{u}_1 \quad (\text{A1})$$

$$0 = -\nabla p_2 + \nabla^2 \mathbf{u}_2 \quad (\text{A2})$$

$$\mathbf{u}_2 \rightarrow 0 \quad \text{as} \quad \|\mathbf{x}\| \rightarrow \infty \quad (\text{A3})$$

$$\mathbf{u}_1 = \mathbf{u}_2 \quad \text{at drop interface} \quad (\text{A4})$$

$$\lambda \mathbf{n} \cdot \mathbf{T}_1 - \mathbf{n} \cdot \mathbf{T}_2 = -\frac{\mathbf{n}}{\text{Ca}} \nabla \cdot \mathbf{n} - n_z \frac{3(1 + \frac{3}{2\lambda})}{1 + \lambda} \quad \text{at drop interface} \quad (\text{A5})$$

where subscript 1 denotes the drop phase, and 2 denotes the suspending phase (see Figure A1).

Here, we have non-dimensionalized the velocity with respect to the translational velocity of a spherical drop of equivalent volume:

$$u_c = \frac{1}{3} \frac{a^2 g}{\nu_2} \left| \frac{\rho_1}{\rho_2} - 1 \right| \left(\frac{1 + \lambda}{1 + \frac{3}{2\lambda}} \right) \quad (\text{A6})$$

The stresses are non-dimensionalized with respect to $\mu_1 u_c / a$ in fluid 1 and $\mu_2 u_c / a$ in fluid 2. Furthermore, $\lambda = \mu_1 / \mu_2$, and $\text{Ca} = \mu_2 u_c / \gamma$ with γ being the interfacial tension of the system.

The problem as posed by Equations A1 and A2 is nonlinear due to the boundary condition A5. This type of problem can be conveniently solved by the boundary-integral technique. Since this method has been applied for many similar problems (see, *e.g.*, [1], [2] or [3] for a more comprehensive description), we will only highlight the principal ideas and the method of numerical implementation.

Consider the Stokes equation:

$$0 = -\nabla p + \nabla^2 \mathbf{u} \quad (\text{A7})$$

and its corresponding stress tensor

$$\mathbf{T} \equiv -p\mathbf{I} + (\nabla\mathbf{u} + (\nabla\mathbf{u})^T) \quad (\text{A8})$$

We shall define the adjoint equation to the Stokes equation as follows:

$$\delta(\mathbf{x} - \mathbf{x}_o) = \nabla q + \nabla^2 \mathbf{u} \quad (\text{A9})$$

and its corresponding stress tensor as

$$\mathbf{\Sigma} \equiv q\mathbf{I} + (\nabla\mathbf{v} + (\nabla\mathbf{v})^T) \quad (\text{A10})$$

The adjoint equation can be solved analytically under the boundary conditions that both q and \mathbf{v} vanish at the far-field with solution

$$v_i^j = -\frac{1}{8\pi} \left(\frac{\delta_{ij}}{r} + \frac{r_i r_j}{r^3} \right) \quad (\text{A11})$$

$$q^j = \frac{1}{4\pi} \left(\frac{r_j}{r^3} \right) \quad (\text{A12})$$

$$\Sigma_{kl}^j = \frac{3}{4\pi} \left(\frac{r_k r_l r_j}{r^5} \right) \quad (\text{A13})$$

where $\mathbf{r} = (\mathbf{x} - \mathbf{x}_o)$. Here, v_i^j corresponds to the i^{th} component of the velocity at \mathbf{x} due to a unit force (stokeslet) located at \mathbf{x}_o in the direction of \mathbf{e}_j .

Using simple vector identities, it is straightforward to derive the following equation:

$$\nabla \cdot (\mathbf{v} \cdot \mathbf{T} - \mathbf{u} \cdot \mathbf{\Sigma}) = \mathbf{v} \cdot (-\nabla p + \nabla^2 \mathbf{u}) - \mathbf{u} \cdot (\nabla q + \nabla^2 \mathbf{u}) \quad (\text{A14})$$

Using Equations A7 and A9, Equation A14 becomes:

$$\nabla \cdot (\mathbf{v} \cdot \mathbf{T} - \mathbf{u} \cdot \mathbf{\Sigma}) = -\mathbf{u} \cdot \delta(\mathbf{x} - \mathbf{x}_o) \quad (\text{A15})$$

Integrating Equation A15 over the volume of the domain and applying the divergence theorem to the resulting volume integrals gives:

$$\mathbf{u}(\mathbf{x}_o) = - \int_S \mathbf{n} \cdot \mathbf{T}(\mathbf{x}) \cdot \mathbf{v}(\mathbf{x} - \mathbf{x}_o) dS + \int_S \mathbf{n} \cdot \mathbf{\Sigma}(\mathbf{x} - \mathbf{x}_o) \cdot \mathbf{u}(\mathbf{x}) dS \quad (\text{A16})$$

$\mathbf{x}_o \in \mathbf{D}$

The first integral is usually known as the single layer potential while the second one is known as the double layer potential. Since we are interested in obtaining the velocity on the surface of the drop, we need to obtain the limit of Equation A16 as $\mathbf{x}_o \rightarrow \mathbf{x}_s \in S$. The single layer potential is continuous at the boundary while the double layer potential suffers a jump condition:

$$\lim_{\mathbf{x}_o \rightarrow \mathbf{x}_s} \int_S \mathbf{n} \cdot \Sigma(\mathbf{x} - \mathbf{x}_o) \cdot \mathbf{u}(\mathbf{x}) dS = \frac{1}{2} \mathbf{u}(\mathbf{x}_s) + \int_S \mathbf{n} \cdot \Sigma(\mathbf{x} - \mathbf{x}_o) \mathbf{u}(\mathbf{x}) dS \quad (\text{A17})$$

Therefore, taking the limit of Equation A16 as $\mathbf{x}_o \rightarrow \mathbf{x}_s$ and using jump condition A17 gives

$$\frac{1}{2} \mathbf{u}(\mathbf{x}_s) = - \int_S \mathbf{n} \cdot \mathbf{T}(\mathbf{x}) \cdot \mathbf{v}(\mathbf{x} - \mathbf{x}_s) dS + \int_S \mathbf{n} \cdot \Sigma(\mathbf{x} - \mathbf{x}_s) \cdot \mathbf{u}(\mathbf{x}) dS \quad (\text{A18})$$

$\mathbf{x}_s \in S$

At this point, we have converted the Stokes equation into an integral equation as given by Equation A18. The unknowns are $\mathbf{u}(\mathbf{x}_s)$ and $\mathbf{T}(\mathbf{x}_s)$, while \mathbf{v} and Σ are given by Equations A11 and A13. By applying Equation A18 to both phases 1 and 2, eliminating the stress difference with boundary condition A5 and substituting the explicit form of \mathbf{v} and Σ given by Equations A11 and A13, we obtain

$$\frac{1}{2}(1 + \lambda \mathbf{u}(\mathbf{x}_s)) = \frac{1}{8\pi} \int_S \left(\frac{\mathbf{I}}{\mathbf{r}} + \frac{\mathbf{r}^2}{r^3} \right) \cdot \mathbf{Q} dS - \frac{3}{4\pi} (1 - \lambda) \int_S \frac{\mathbf{r}^3}{r^5} \cdot \mathbf{u} \cdot \mathbf{n} dS \quad (\text{A19})$$

$\mathbf{x}_s \in S$

For simplicity, we assume axisymmetry in the problem. Thus, it is convenient to integrate Equation A19 in the azimuthal direction analytically. Upon such integration, the surface integrals in Equation A18 are converted to line integrals:

$$\frac{1}{2}(1 + \lambda) \begin{bmatrix} u_r(\mathbf{x}_s) \\ u_z(\mathbf{x}_s) \end{bmatrix} = \frac{1}{8\pi} \int_S \mathbf{B}(\mathbf{x}, \eta) \cdot \begin{bmatrix} Q_r(\eta) \\ Q_z(\eta) \end{bmatrix} dl - \frac{3}{4\pi(1 - \lambda)} \int_S \mathbf{C}(\mathbf{x}, \eta) \cdot \begin{bmatrix} Q_r(\eta) \\ Q_z(\eta) \end{bmatrix} dl \quad (\text{A20})$$

Here, \mathbf{B} and \mathbf{C} are matrices whose elements are composed of various elliptic integrals (see Lee and Leal[1]).

Equation A20 is then discretized over the interface of the drop. This results in a set of linear and coupled algebraic equations. The velocity of each of the elements is assumed constant. The shape of the drop is described by the arclength parametrization method (Ascoli[4]). For cylindrical coordinates (r, z) , the collocation points in the discretization scheme are represented by $r(s)$ and $z(s)$, in which s is the normalized measure of the arclength ($0 \leq s \leq 1$).

Using cubic splines for $r(s)$ and $z(s)$, most drop shapes can be represented accurately with a modest number of elements in the discretization. For most of the cases examined, 50 elements are used and found to be satisfactory.

The set of algebraic equation is solved, using Gaussian elimination, to obtain the velocities for each of the elements on the interface. Knowing the velocities, the interfacial elements are “moved” after each time step (typically, $0.05 \leq \Delta t \leq 0.1$) to give the new drop shape. In addition to providing the new shape, this method of time incrementation also gives the actual amount of movement of the center of mass of the drop.

Bibliography

- [1] S.H. Lee and L.G. Leal; *J. Colloid Interface Sci.*, **87**,81(1982).
- [2] H.A. Stone and L.G. Leal; *J. Fluid Mech.*, **198**,399(1989).
- [3] O.A. Ladyzhenskaya; *The Mathematical Theory of Viscous Incompressible Flow*, Gordon and Breach, New York(1963).
- [4] E.P. Ascoli; *Ph.D. Thesis*, California Institute of Technology, Pasadena(1988).

Figure Captions

1. Schematic diagram of the general problem.

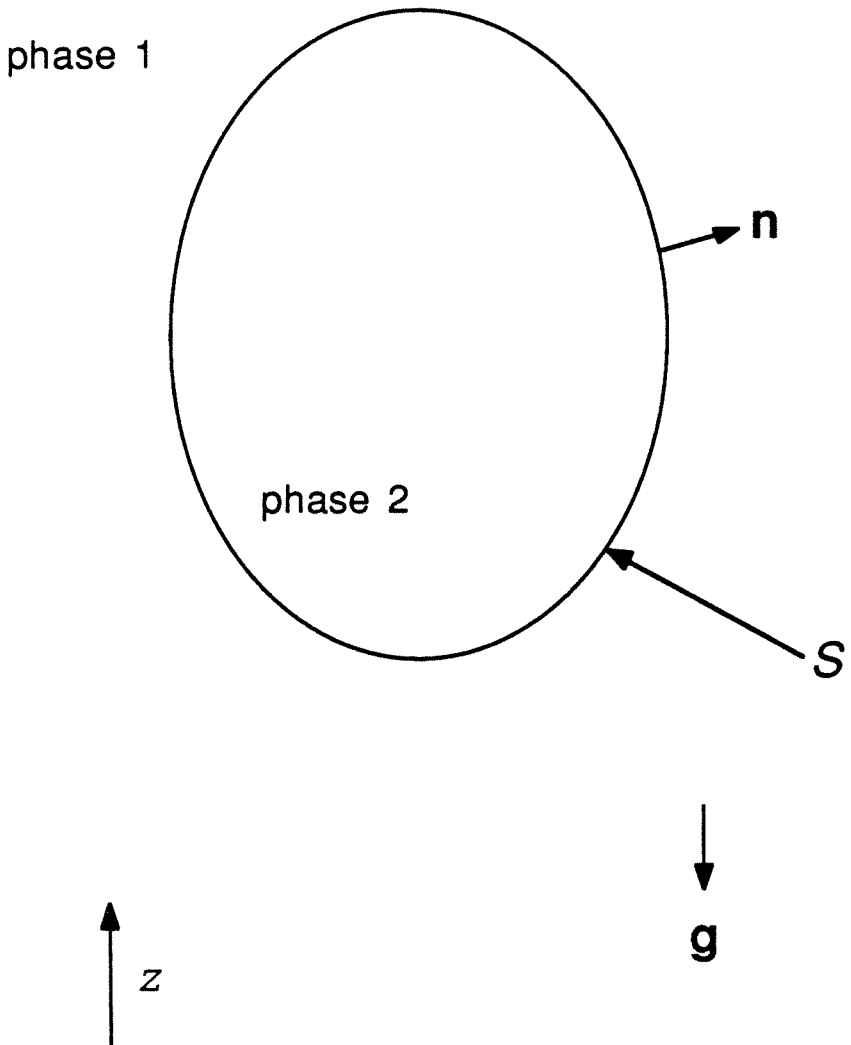


Figure A1

Chapter 2

An Experimental Investigation on the Stability of Viscous Drops Translating through a Quiescent Fluid

An Experimental Investigation on the Stability of Viscous Drops Translating through a Quiescent Fluid¹

Christopher J. Koh²

California Institute of Technology
Department of Chemical Engineering

and

L. Gary Leal³

University of California, Santa Barbara
Department of Chemical and Nuclear Engineering

¹The basic text in this chapter consists of an article which appeared in *Phys. Fluid A*, 2 No. 12, 2103(1990).

²California Institute of Technology, Chemical Engineering, mail code 210-41, 1201 E. California Blvd., Pasadena, CA 91125, USA.

³To whom correspondence should be addressed: University of California, Chemical and Nuclear Engineering Dept., Santa Barbara, CA 93106, USA. Tel:(805)893-8510, Fax:(805)893-4731.

An Experimental Investigation on the Stability of Viscous Drops Translating through a Quiescent Fluid

Abstract

The evolution of the shape of an initially nonspherical drop translating at low Reynolds number through a quiescent fluid is investigated experimentally. It is found that the drop reverts to a spherical shape when the degree of initial deformation is small enough. However, drops that are highly deformed initially are shown to deform continuously. Specifically, a prolate drop breaks up into multiple droplets as it rises, while an oblate drop deforms into a double-emulsion drop as it translates. The experimental results agree well with results obtained earlier from numerical simulations (Koh and Leal, 1989).

Chapter 2

An Experimental Investigation on the Stability of Viscous Drops Translating through a Quiescent Fluid

2.1 Introduction

In an earlier paper (Koh and Leal[1]), we used the boundary-integral method to investigate the evolution of the shape of an initially nonspherical drop translating in an unbounded and otherwise quiescent fluid at zero Reynolds number. We showed that for finite capillary number,

$$\text{Ca} \equiv \frac{2\Delta\rho a^2 g(1 + \lambda)}{9\sigma(\frac{2}{3} + \lambda)} \quad (2.1)$$

an initially nonspherical translating drop will undergo one of three possible fates. If the initial degree of nonsphericity is small enough, the drop simply reverts back to a spherical shape, *i.e.*, the classical solution of Hadamard and Rybczinski. On the other hand, if the initial deformation is large enough, the degree of deformation continues to increase with time. For initially prolate shapes, the drop elongates with the formation of a tail; subsequently, the numerical results suggest that the tail breaks off into one or more droplets. For initially oblate shapes, the drop develops a rear cavity as it translates. In the latter two cases, we say that the initial drop shape is *unstable* (see also Pozrikidis[2], who showed similar results).

The purpose of the current investigation is to study the behavior of a translating drop at low Reynolds number experimentally. Specifically, the objectives of the

experiment are three-fold. First, we seek confirmation of the two distinct modes of unstable drop deformation mentioned above. Second, the numerical simulations were performed mostly for rather idealized initial conditions, *i.e.*, axisymmetric ellipsoids. It is important to determine if the qualitative behavior of drop deformation as well as the stability criteria obtained numerically are applicable to *real systems* with less ideal initial shapes (*e.g.*, non-ellipsoidal and slightly non-axisymmetric drops.) Finally, the computer simulations were terminated when a thin neck appeared in the prolate cases and when the rear cavity closed up on itself in the oblate cases. Thus, the present experiments also serve to explore the drop dynamics beyond the limit of the numerical simulations.

2.2 Experimental Procedure

The experiments were performed in a Lucite tank of square cross-section (40.6cm \times 40.6cm \times 91.4cm). A Lucite syringe assembly is attached to a circular opening (diameter=5.1cm) located underneath the tank. The Lucite syringe has an I.D. of 5.1cm and length of 15.2cm. As described below, this large syringe is used to “control” the initial shape of the drop. An aluminum tube (I.D.=0.64cm), connected at one end to a small syringe, can be inserted into the Lucite syringe for injection of the drop phase. Figure 2.1 shows the schematic of the experimental setup.

The suspending fluid was Pale 1000 oil (oxidized castor oil available from Caschem, Inc. of Bayonne, NJ). In order to obtain data for a range of viscosity ratio (λ), four different grades of Dow Corning 200 silicone fluid (1,000cs, 10,000cs, 30,000cs and 100,000cs) were used as the drop phase. These fluids were selected so that the Reynolds number was small ($Re < 0.01$ for all the cases investigated), the capillary number in the range $1 < Ca < 5.5$ (at which the numerical study showed modestly deformed drops to be unstable), and the drops large enough for simple photography.

Table 1 summarizes the physical properties of these fluids at the temperature (22°C) under which the experiments were performed. The densities and the vis-

cosities were measured by a pycnometer and various Cannon-Fenske capillary viscometers respectively. The interfacial tensions were calculated from the small deformation theory of Taylor for a drop in a pure-straining flow using data obtained in a computer-controlled four-roll mill described by Bentley and Leal[3].

The drop was injected into the large syringe assembly from the small syringe; it then rose to the tank under gravity. The capillary number was varied by adjusting the amount of drop fluid injected ($Ca \propto a^2$, where a is the equivalent drop radius.) Typically, the size of the drop ranged from 1cc to 10cc. After the drop had completely moved out of the syringe assembly and into the tank, the plunger was pushed up to produce an oblate drop or pulled down to produce a prolate drop. The flow field created by the motion of the plunger deformed the drop; the degree of initial deformation was controlled by the amount of displacement of the plunger. In most cases, the plunger was displaced between 1cm to 5cm.

After the desired initial shape was obtained, photographs of the drop were taken at intervals ranging from 15 seconds to 4 minutes to capture the evolution of drop shapes. (The rate of deformation is lower for a more viscous drop; consequently, the frequency at which pictures were taken depended on the viscosity ratio of the system under investigation.) A Canon A-1 camera equipped with a Canon macro lens (model FD 200mm) was used. The films were Kodak Tri-X pan 400. An exposure time of 1/30 second and automatic aperture control were utilized. A 150-watt spotlight covered with a plastic light diffuser was placed behind the tank to provide background lighting.

The major and minor axes of each of the initial shapes were measured by projecting the negatives onto a screen at approximately $10\times$ magnification. To quantify the initial degree of deformation, the classical "Taylor" parameter was used:

$$\Delta_e \equiv \frac{L - B}{L + B} \quad (2.2)$$

It should be emphasized, however, that the initial shapes were rarely ellipsoidal, as is assumed inherently in Δ_e . Instead, L and B were measured as the maximum

and minimum dimensions as illustrated in Figure 2.2. Thus, Δ_e gives only a crude estimate of the initial deformation since drops with the same Δ_e can have quite different shapes; this will influence our ability to compare *quantitatively* experimental results with the numerical results obtained in our earlier study.

2.3 Results

As suggested by the results of the numerical simulations, the experiments were performed for two types of initial drop shapes, namely, prolate and oblate drops. Let us begin by discussing the experimentally observed behavior from a qualitative point of view.

Figure 2.3 shows typical results for the deformation of a stable prolate drop. Here, $\lambda = 0.26$ ($\lambda = \mu_{\text{drop}}/\mu_{\text{bulk}}$, the viscosity ratio), $\text{Ca} = 2.0 \pm 0.2$ and $\Delta_e = 0.06$. It is clear that as the drop rose, the deformation decreased. Eventually, the drop became spherical, as can be seen at $t=240\text{s}$. On the other hand, Figure 2.4 shows typical results for the evolution of an unstable prolate drop. Here, $\lambda = 0.26$, $\text{Ca} = 2.0 \pm 0.2$ and $\Delta_e = 0.18$. For this larger initial deformation, we can see that as the drop rose, a tail was formed at its rear. The tail elongated and finally broke off from the parent drop around $t=240$. After the breakup, the parent drop became spherical, while the tail broke up through capillary instability as well as an end-pinching process into multiple droplets as seen at $t=420\text{s}$.

As in the prolate case, the oblate drops were found to be stable provided that the initial deformation was small enough. The deformation of a stable oblate drop is shown in Figure 2.5. Here, $\lambda = 0.026$, $\text{Ca} = 2.9 \pm 0.3$ and $\Delta_e = -0.45$. The deformation decreased as the drop rose, and finally reverted back to the steady spherical shape as shown at $t=180\text{s}$. A more interesting result was found for the evolution of unstable oblate drops (Figure 2.6). Here, $\lambda = 0.026$, $\text{Ca} = 3.4 \pm 0.3$ and $\Delta_e = -0.69$. Initially, the cavity at the back of the drop was of moderate size. As the drop rose, the cavity became longer and narrower, and eventually evolved into

a skirt-like structure. Then, the bottom of the drop closed up on itself ($t=307s$) while the middle cylindrical section of the drop elongated and became very thin ($t=422s$). Eventually, the top portion of the drop broke off forming an encapsulated drop, and the bottom portion of the drop broke up into multiple double-emulsion drops (this cannot be seen in the photographs due to lack of resolution).

It is interesting to point out that drop shapes similar to those shown in Figure 2.6 have been observed in other experimental studies. For example, Kojima, Hinch and Acrivos[4] found that *miscible* drops at moderately low Reynolds number ($0.14 < Re < 0.66$) can deform into tori. Also, Bhaga and Weber[5] found that bubbles at *high* Reynolds number can have spherical cap shapes or skirt-like structure (depending on the Eötvös number and the Morton number). However, no direct comparisons with the current experimental results have been made since the range of physical parameters is quite different.

We have also investigated the role played by λ in the evolution of drop shapes. In the broadest sense, *i.e.*, the formation of a tail for unstable prolate drops and a rear cavity for unstable oblate drops, the dynamic behavior of the drops are similar regardless of the viscosity ratio. However, there are some detailed differences, both qualitative and quantitative, among systems of different viscosity ratios. In the prolate cases, the tail of a less viscous drop (see Figure 2.7) was thin and short compared to that of a more viscous drop. This thin and short tail broke off from the parent drop at a relatively early stage of the evolution. On the other hand, as illustrated in Figure 2.8, the tail of a viscous drop was thicker and longer. Moreover, this tail did not break off as early and the total volume of fluid detached from the parent drop was larger compared to that of a less viscous drop. The last photograph of the sequence in Figure 2.8 shows the tail of the drop breaking up into small droplets.

For the oblate cases, the evolution of drops of different viscosity ratios is also different. The behavior of a low viscosity drop (as shown in Figure 2.3) has already been discussed in detail. For high viscosity systems, the rear cavity deepened

without the formation of a skirt-like structure as the drop deformed. Eventually, a single double-emulsion drop was formed. Figure 2.9 shows the evolution of such a drop with $\lambda = 2.6$, $Ca = 1.3 \pm 0.1$ and $\Delta_e = -0.65$. It should be noted this is the only case where an initially unstable drop did not break up as it evolved; in the cases of unstable oblate drops of low viscosity ratio and unstable prolate drops (regardless of viscosity ratio), drop breakup was always observed.

It is apparent that the qualitative experimental behavior of drop deformations agree quite well with that predicted by the numerical simulations. However, it is necessary to be sure that certain experimental conditions, such as the finite size of the tank, the effects of the plunger flow on the initial condition, and the possibility of surfactant effects due to impurities in the bulk fluid, have negligible influence on the deformation of the drop. Consequently, we have computed the drop evolution of two specific cases using actual experimental initial drop shapes. In order to compare the drop shapes at different stages of the experiment, it is necessary to non-dimensionalize the actual time with t_c ($t_c \equiv a/u_c$, where u_c is the translational velocity of a spherical drop with the same volume, and a is the equivalent radius).

In Figure 2.10, we compare the experimental evolution of an unsteady prolate drop ($Ca = 2.1 \pm 0.2$, $\lambda = 0.74$, and $t_c = 32 \pm 2s$) with the numerical simulation using the same initial drop shape and physical parameters. We can see clearly that the simulation compares well with the actual experiment. The small difference in the drop shapes, especially in the latter stages of the experiment, is most likely due to the uncertainty in estimating the various physical parameters and the initial shape.

As shown in Figure 2.11, we have also performed numerical simulation to compare with the unsteady experimental deformation of an oblate drop ($Ca = 3.4 \pm 0.3$, $\lambda = 0.026$, and $t_c = 22 \pm 1s$). Again, we can see that there is good agreement between the drop shapes obtained from experiment and numerical simulation. The last photograph from the experiment was obtained at $t=8.2$. However, due to numerical difficulties (*i.e.*, when opposing surface elements become closer than some

predetermined value, as seen in the “skirt-like” structure near the bottom half of the drop), the computer program was terminated at $t=6.4$. From these comparisons (Figures 2.10 and 2.11), we are confident that the drop behavior observed in the experiment is not caused by the “extraneous” experimental conditions mentioned above.

As we have stated earlier, one of the objectives of this study is to determine if the stability criteria obtained numerically are applicable to drops with initial shapes different from the idealized ones used in the numerical study. To this end, we have summarized the stability behavior of initially nonspherical drops obtained from the experiment in Figure 2.12. Here, we denote initial shapes that revert back to a sphere as being stable, while those which do not are termed unstable. The open symbols in Figure 2.12 refer to stable initial drop shapes while the shaded symbols are for unstable drops. For each of the four viscosity ratios investigated, we expect the neutral stability curve to lie between the shaded and open symbols. This figure basically confirms the numerical results (see Figure 1.11). The critical value of the capillary number increases monotonically as the degree of initial deformation is decreased. Furthermore, it is quite apparent that the stability criteria for prolate drops depend only weakly on the viscosity ratio. The stability curves, for the range of viscosity ratio investigated, all lie within the shaded region as shown on the upper half of the graph. On the other hand, the λ -dependence of the stability of oblate drops is much more pronounced, and it is evident that a more viscous drop is found to be less stable for the same initial deformation. To summarize, it is remarkable that all the qualitative behavior of drop deformation observed in the numerical studies (for perfect ellipsoids) is preserved in the experiment. This means that the details of the initial drop shape play a minor role in drop deformation—only the general shape of the drop (as measured by Δ_e) dictates the overall behavior in the evolution of initially nonspherical drops.

Acknowledgment: This work was supported by a grant from the Fluid Mechanics Program of the National Science Foundation.

Bibliography

- [1] C.J. Koh and L.G. Leal; *Phys. Fluids A*, **1**, No.8, 1309(1989).
- [2] C. Pozrikidis; *J. Fluid Mech.*, **210**, 1(1990).
- [3] B.J. Bentley and L.G. Leal; *J. Fluid Mech.*, **167**, 219(1986).
- [4] M. Kojima, E.J. Hinch and A. Acrivos; *Phys. Fluids*, **27**, 19(1984).
- [5] D. Bhaga and M.E. Weber; *J. Fluid Mech.*, **105**, 61(1981).

Figure Captions

1. Schematic diagram showing the experimental setup.
2. Sketch showing the definition of Δ_e for a prolate drop and an oblate drop.
3. Evolution of a stable prolate drop. $\lambda = 0.26$, $\text{Ca} = 2.0 \pm 0.2$, and $\Delta_e = 0.06$.
4. Evolution of an unstable prolate drop. $\lambda = 0.26$, $\text{Ca} = 2.0 \pm 0.2$, and $\Delta_e = 0.18$.
5. Evolution of a stable oblate drop. $\lambda = 0.026$, $\text{Ca} = 2.9 \pm 0.3$, and $\Delta_e = -0.45$.
6. Evolution of an unstable oblate drop. $\lambda = 0.026$, $\text{Ca} = 3.4 \pm 0.3$, and $\Delta_e = -0.69$.
7. Evolution of a low viscosity prolate drop.
8. Evolution of a high viscosity prolate drop.
9. Evolution of a high viscosity oblate drop. $\lambda = 2.6$, $\text{Ca} = 1.3 \pm 0.1$, and $\Delta_e = -0.65$.
10. Comparison of the evolution of an unsteady prolate drop with numerical simulation.
11. Comparison of the evolution of an unsteady oblate drop with numerical simulation.
12. Ca_{crit} vs. Δ_e for both oblate and prolate drops. Open symbols refer to stable initial drop shapes while shaded symbols are for unstable drops. The stability curves for prolate drops lie within the shaded region. The stability curves for oblate drops do *not* correspond to the exact value of Ca_{crit} but are drawn to indicate the trend.

Table Captions

1. Viscosities, densities and interfacial tensions of the fluids used in the experiment. ^aValues at room temperature (22°C). ^bInterfacial tension between the silicone fluid and Pale 1000 oil. ^cSilicone Fluid.

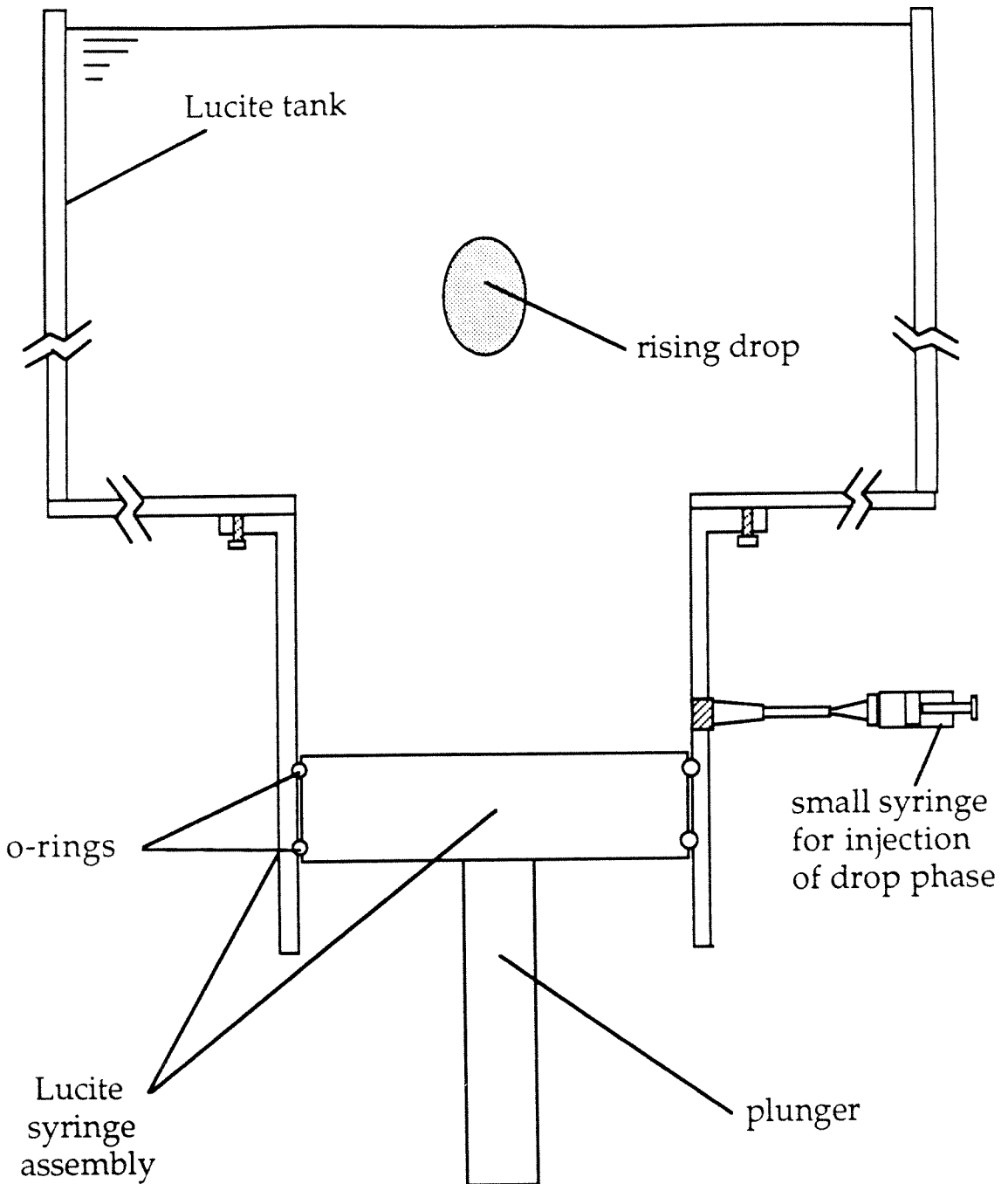
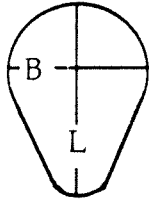
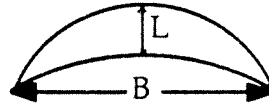


Figure 2.1



Prolate drop



Oblate drop

Figure 2.2

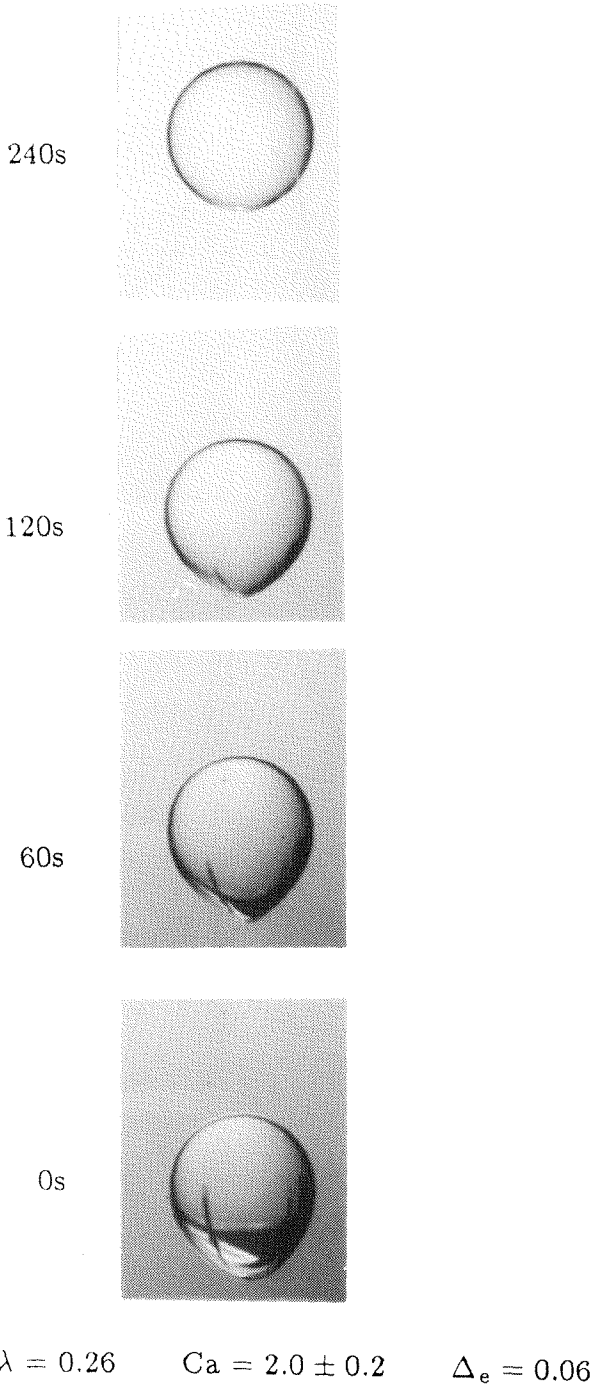
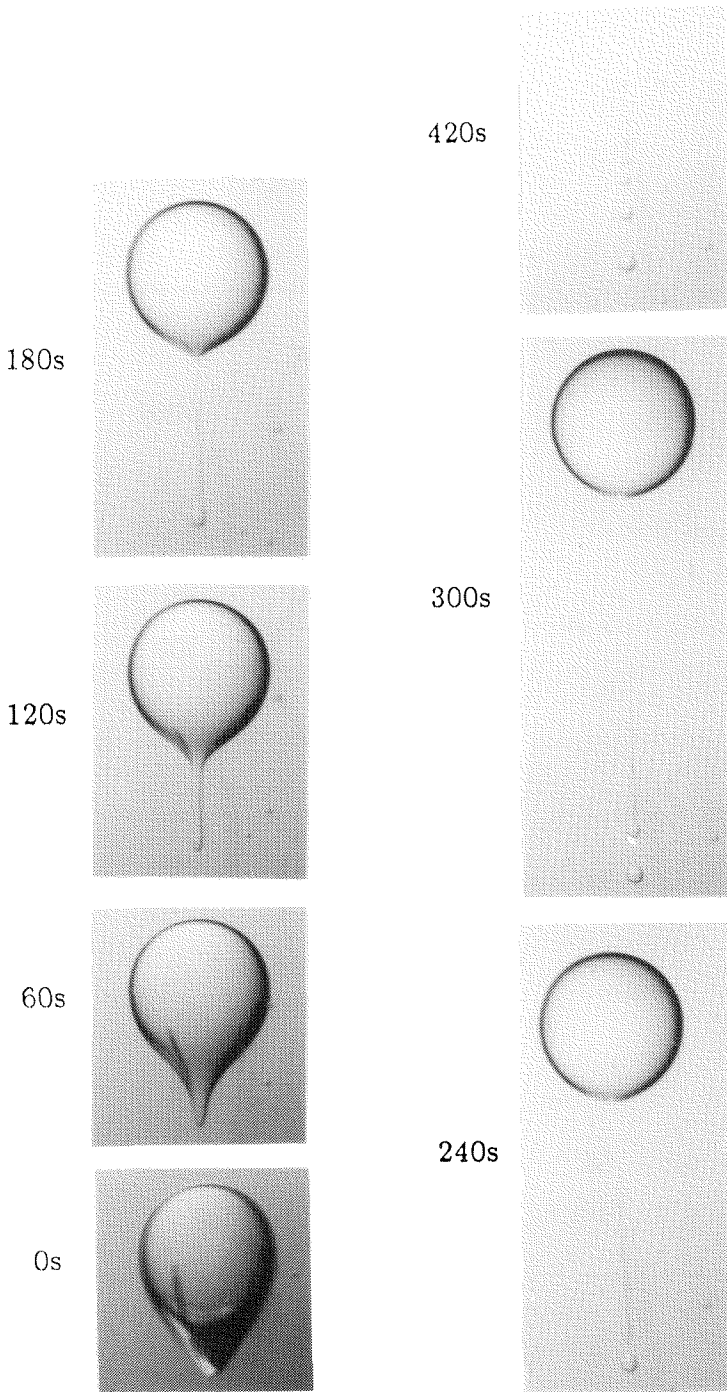


Fig 2.3



$$\lambda = 0.26$$

$$Ca = 2.0 \pm 0.2$$

$$\Delta_e = 0.18$$

Fig 2.4

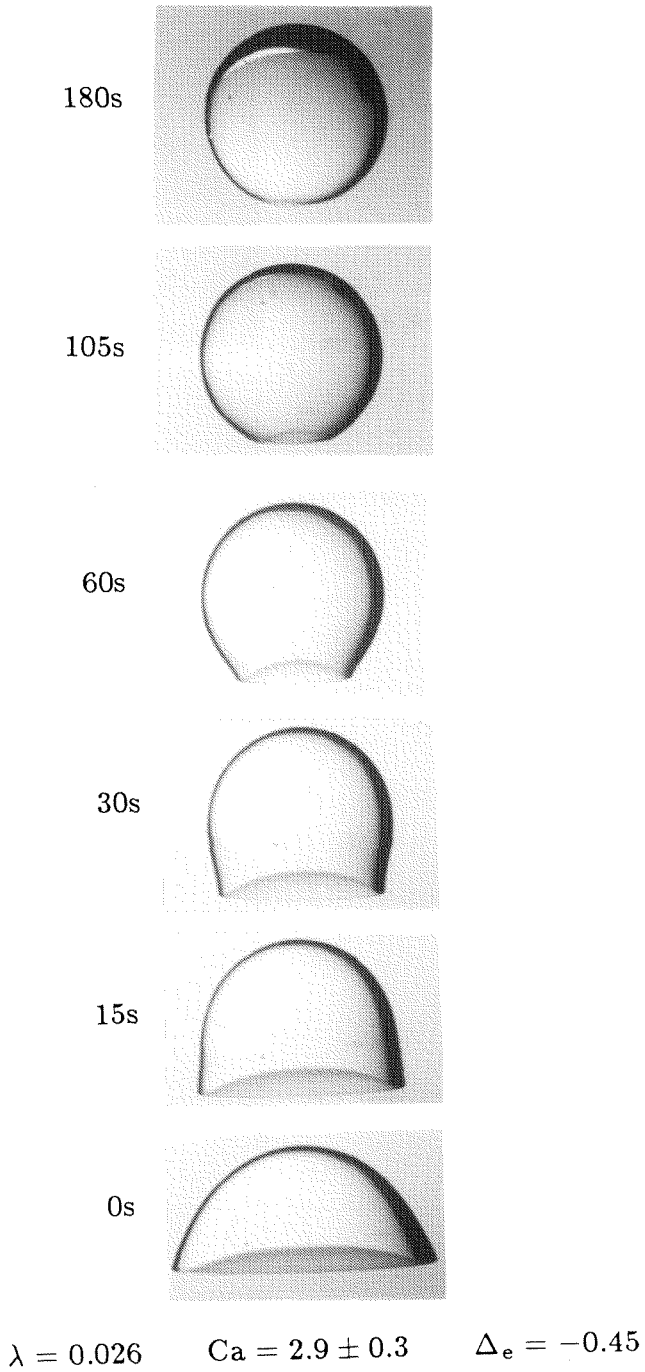


Fig 2.5

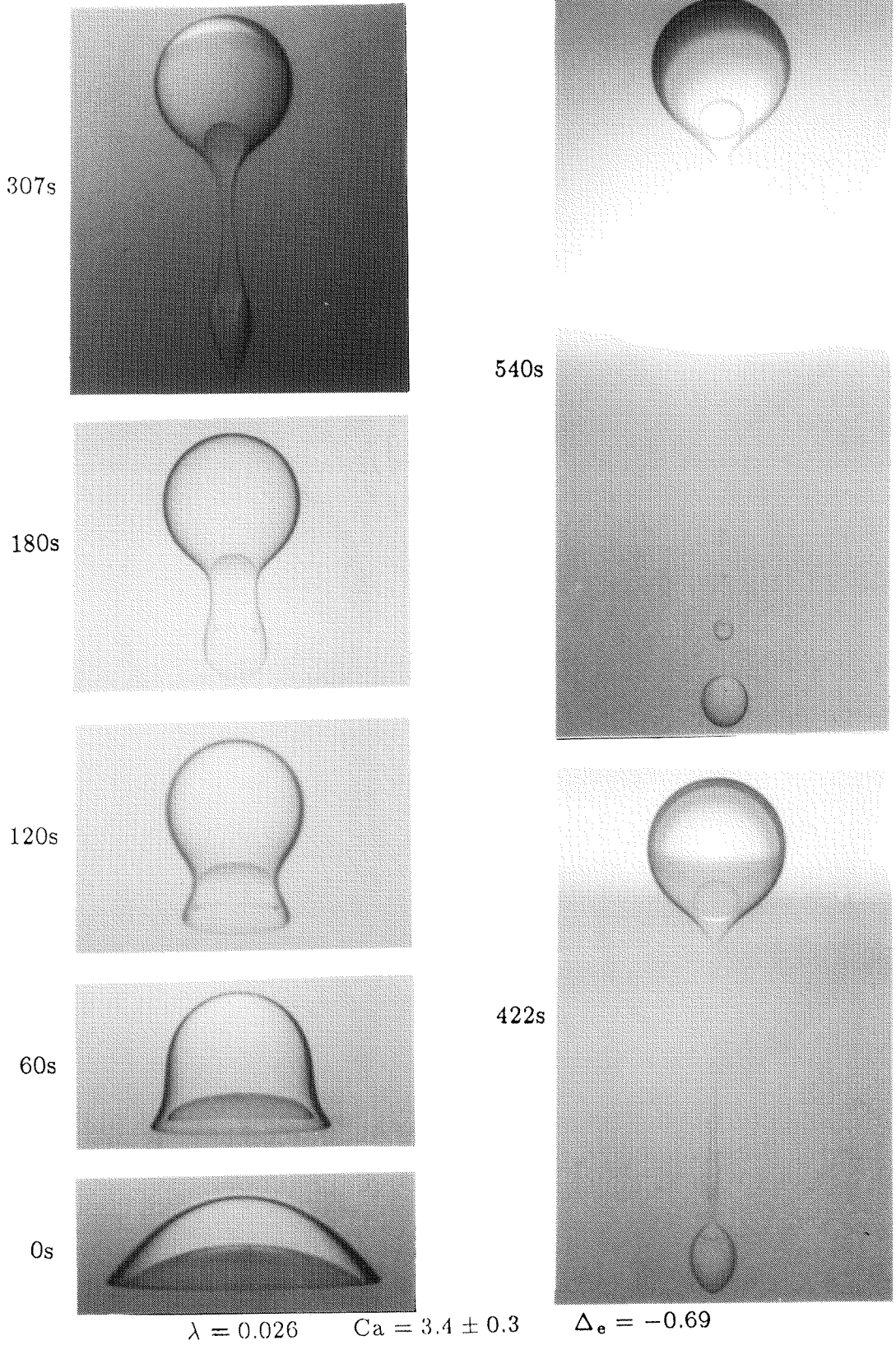
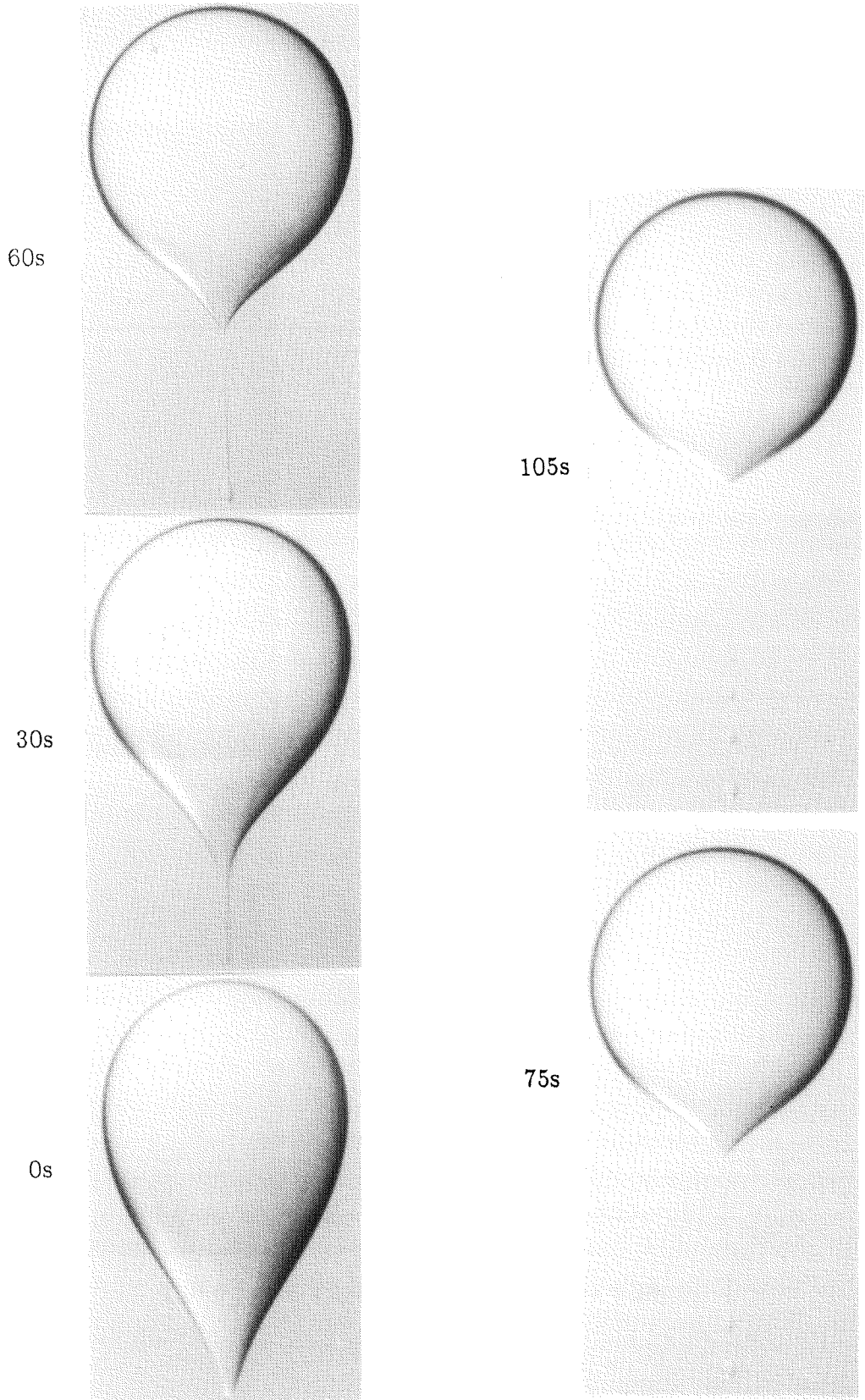


Fig 2.6

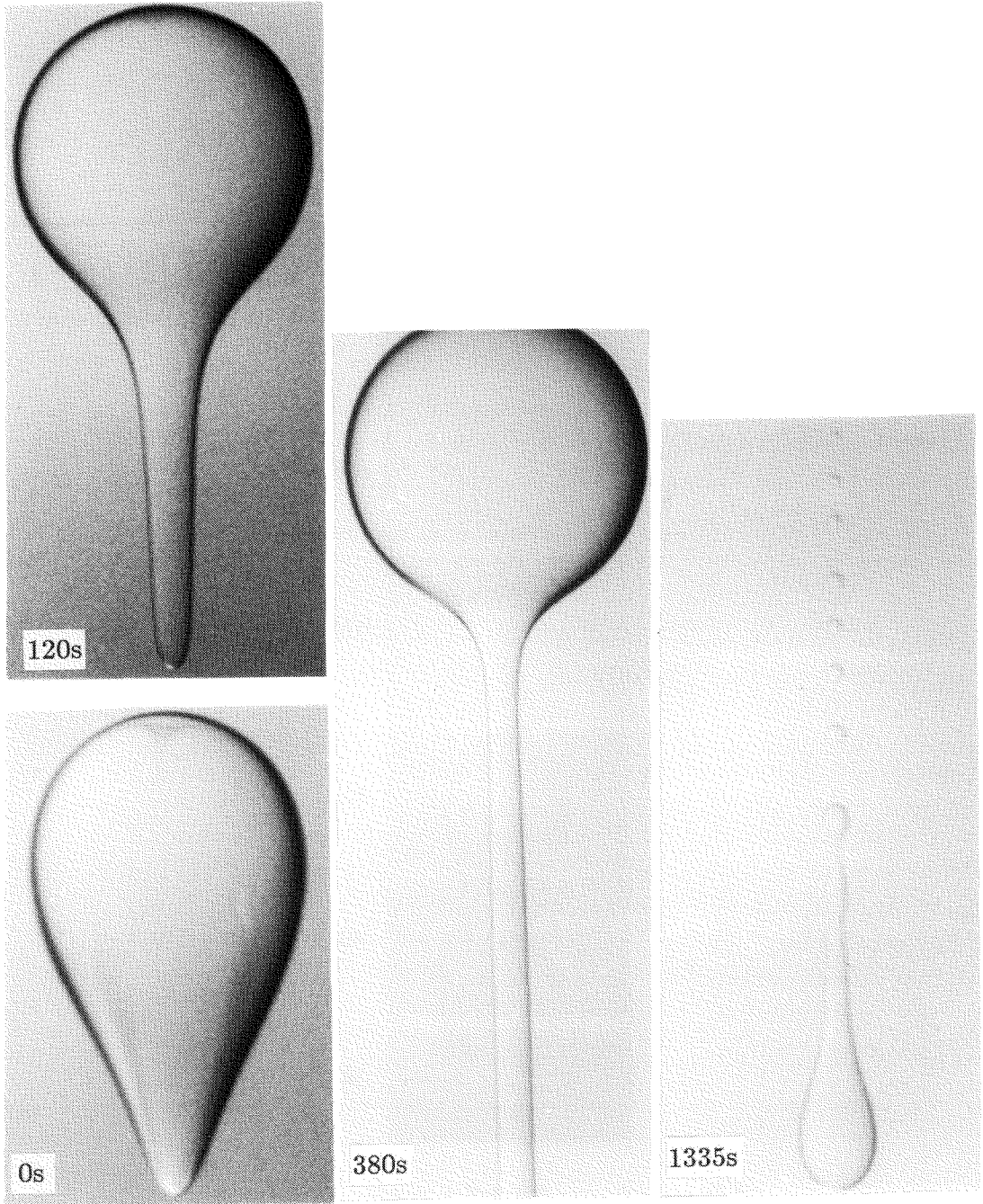


$\lambda = 0.026$

$Ca = 2.2 \pm 0.2$

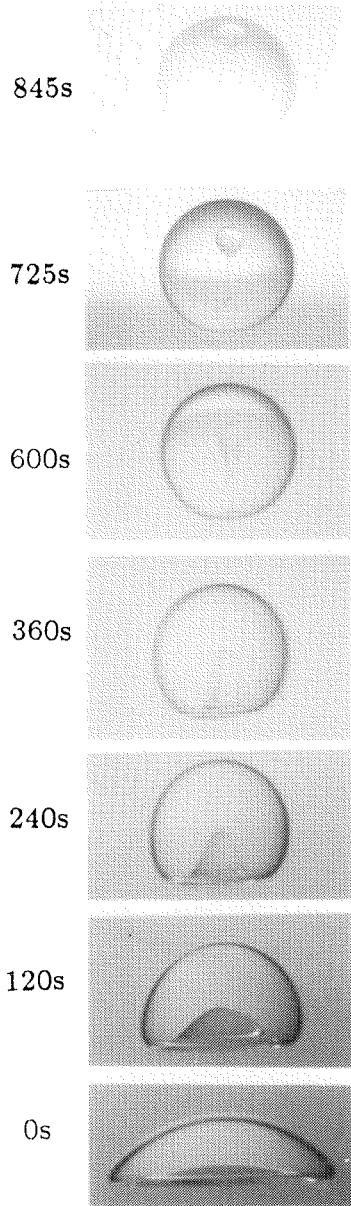
$\Delta_e = 0.25$

Fig 2.7



$\lambda = 0.74$ $Ca = 2.0 \pm 0.2$ $\Delta_e = 0.28$

Fig 2.8



$\lambda = 2.6$ $Ca = 1.3 \pm 0.1$ $\Delta_e = -0.65$

Fig 2.9

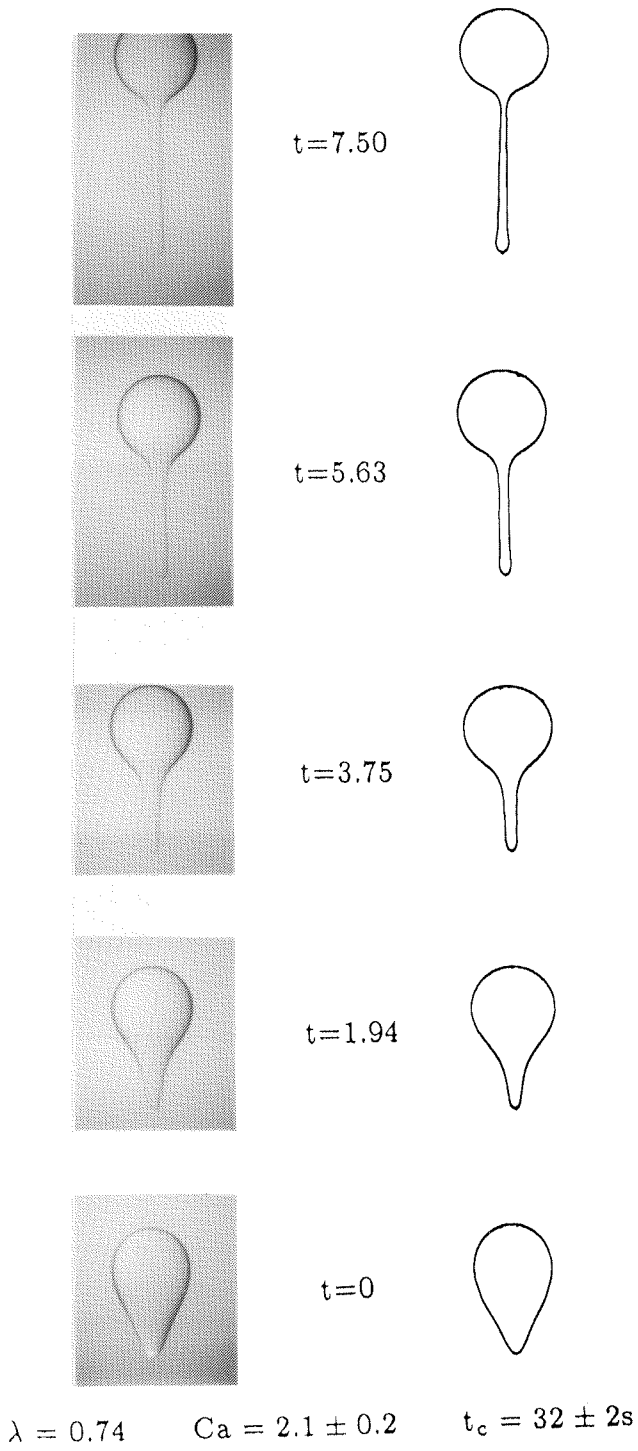
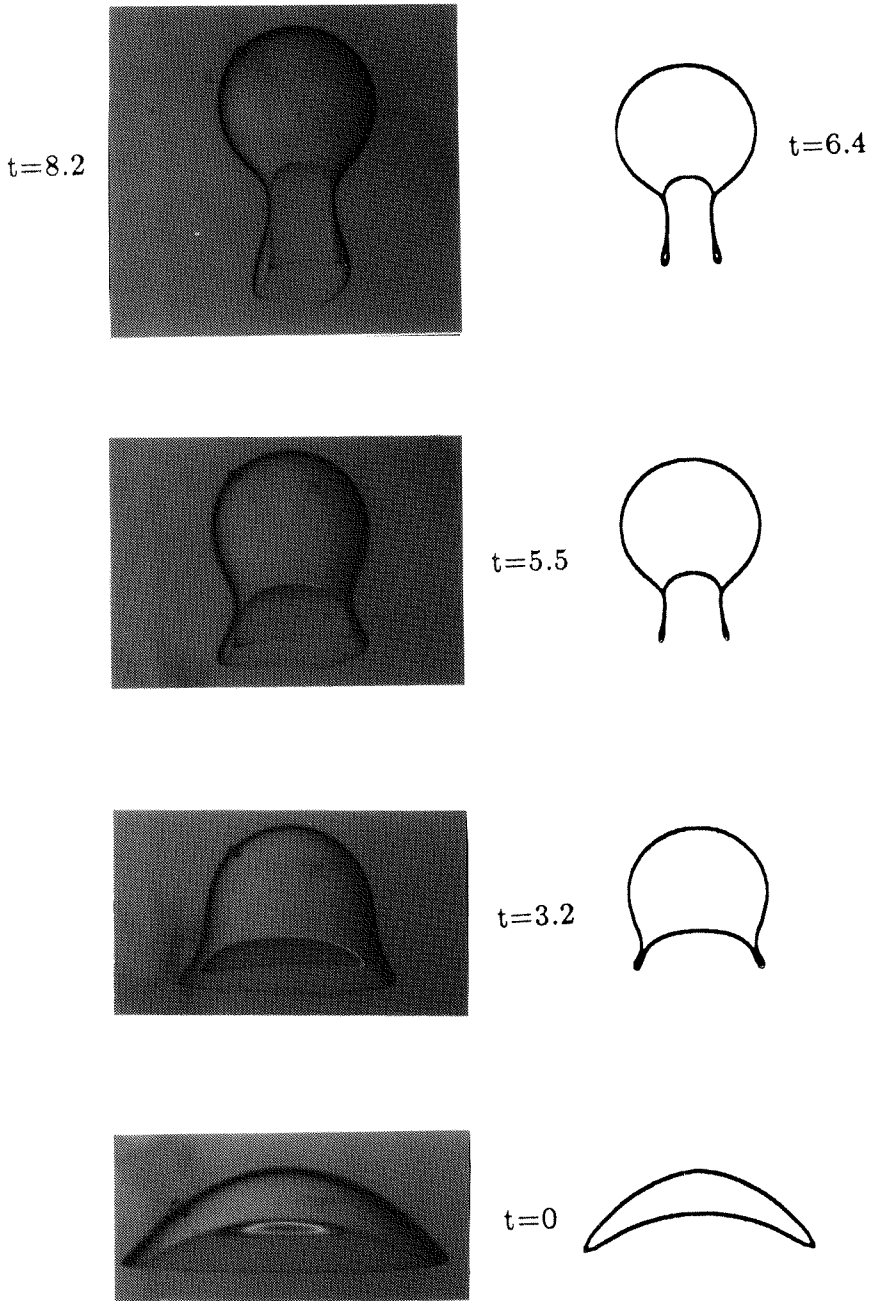


Fig 2.10



$\lambda = 0.26$ $Ca = 3.4 \pm 0.3$ $t_c = 22 \pm 1s$

Fig 2.11

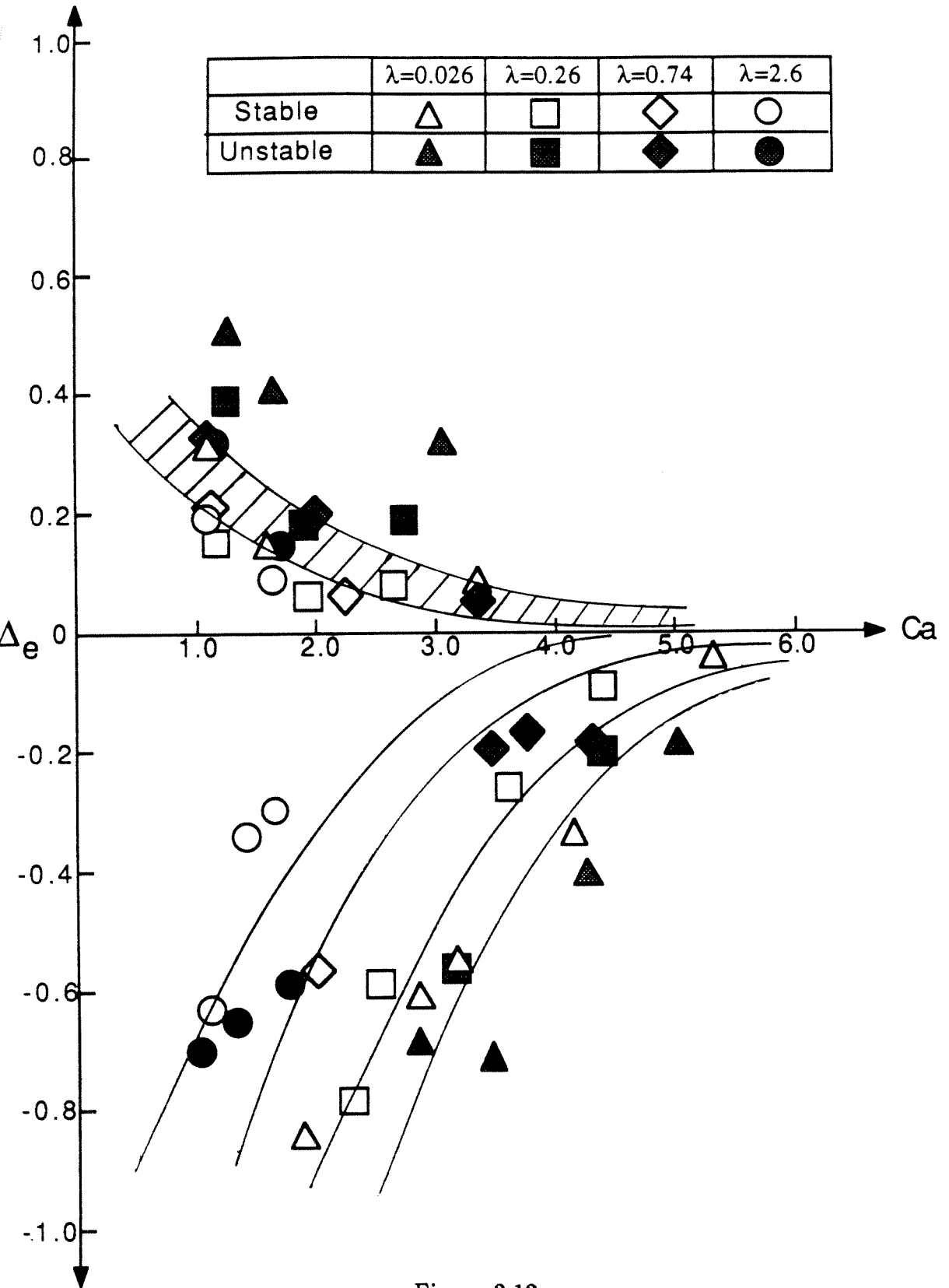


Figure 2.12

Fluids	Viscosity ^a (P)	Density ^a (g/cm ³)	Interfacial tension ^b (dyne/cm)
Pale 1000 oil	391	1.021	—
1,000 cs SF ^c	10.2	0.972	5.8
10,000 cs SF	101	0.972	6.0
30,000 cs SF	291	0.972	5.8
100,000 cs SF	1.02×10^3	0.975	5.8

Table 1

Part II

Flow of Concentrated Suspensions

Chapter 3

An Experimental Investigation of Concentrated Suspension Flows in a Rectangular Channel

An Experimental Investigation of Concentrated Suspension Flows in a Rectangular Channel

Christopher J. Koh¹
California Institute of Technology
Department of Chemical Engineering

and

L. Gary Leal²
University of California, Santa Barbara
Department of Chemical and Nuclear Engineering

¹California Institute of Technology, Chemical Engineering, mail code 210-41, 1201 E. California Blvd., Pasadena, CA 91125, USA.

²To whom correspondence should be addressed: University of California, Chemical and Nuclear Engineering Dept., Santa Barbara, CA 93106, USA. Tel:(805)893-8510, Fax:(805)893-4731.

An Experimental Investigation of Concentrated Suspension Flows in a Rectangular Channel

Abstract

An experimental adaptation of the well-known Laser Doppler Anemometry technique is developed for measuring the velocity and concentration profiles in concentrated suspension flows. To circumvent the problem of optical turbidity, the refractive indices of the solid and liquid phases are closely matched. The residual turbidity, due to small mismatches of the refractive indices, as well as impurities in the particles, allows a Doppler signal to be detected when a particle passes through the scattering volume. By counting the number of Doppler signals in a period of time, the local particle volume fraction is also measured.

This new technique is utilized to study concentrated suspension flows in a rectangular channel. The general behavior of the suspension is that the velocity profile is blunted while the concentration profile has a maximum near the center. Comparisons are made with theoretical predictions based on the shear-induced particle migration theory.

Chapter 3

An Experimental Investigation of Concentrated Suspension Flows in a Rectangular Channel

3.1 Introduction

The flow of suspensions is relevant to a wide variety of both natural and industrial processes. Among the most common naturally occurring examples are blood flow in which the particulate phase is comprised of blood cells, and flows in the sedimentation of muddy water and sand storms. Industrial applications can also be found in abundance—coal slurry flows and fluidized beds are but two examples.

Suspensions, especially concentrated ones, can show interesting, non-Newtonian behavior because of the interplay among the particles, the surrounding fluid and the boundaries of the flow. This interaction is governed predominantly by three kinds of forces. The first one is colloidal force, which can be attractive (*e.g.*, London-van de Waals force) or repulsive (*e.g.*, electrostatic force). Depending on the strength of these forces, the particulate phase can either be flocculated or dispersed. The second is the well-known Brownian force, due to random collisions of the surrounding fluid molecules with the particles. It affects the spatial distribution of all particles, and in the case of nonspherical particles, the orientation distribution as well. The influence of this randomizing force is strongly particle size dependent, and can usually be neglected for particles larger than $1\mu\text{m}$.

When the suspension is at rest, the two aforementioned forces dictate its struc-

ture. However, when the suspension is subject to flow, hydrodynamic forces become important (*e.g.*, when the Péclet number $Pe = \dot{\gamma}a^2/D_0 \gg 1$, where Pe is the ratio of shear force compared to Brownian force, $\dot{\gamma}$ is the magnitude of the shear rate and D_0 is the diffusion coefficient of a single particle due to Brownian motion.) In this study, we will only deal with suspensions of spherical particles that are sufficiently large so that colloidal and Brownian forces are negligible, but small enough so that inertia forces can also be neglected.

Some significant experimental investigations[2, 3] have been made of the flow of dilute suspensions, where interactions between particles are negligible. The best-known phenomenon identified in these studies is probably the “tubular pinch effect.” For example, Segré and Silberberg[3] found, in the flow of a low concentration suspension through a tube, that solid particles migrate to a preferred location somewhere between the tube axis and the tube wall while the velocity profile remains parabolic. Numerous theoretical studies [4, 5, 6] have shown conclusively that this particle migration phenomenon is a consequence of weak inertia effect in the interaction of the particle and the suspending fluid.

The first major experimental study for concentrated suspension flow in a tube was performed by Karnis, Goldsmith and Mason[7]. By using cinematography, these researchers found that the velocity profiles of the particles are increasingly blunted at the center as either the particle size or the bulk particle concentration is increased. By counting tracer particles crossing a plane, they also reported that, within their experimental accuracy, the particle concentration was uniform across the tube.

Much more recently, Kowalewski[8] used Ultrasound Doppler Anemometry to measure the velocity profile for concentrated suspensions of solid and liquid particles in tube flows. In the case of solid suspensions, he found that the blunting of the velocity profile can be characterized by the empirical formula $v = v_0(1 - r^b)$, with b increasing with the concentration of the suspension and the relative size of the particles (*i.e.*, a power-law fluid, with $b=2$ being a Newtonian fluid). For the case

of droplet suspensions, b also depends on the viscosity ratio of the two phases. The ultrasonic experimental method is very useful, but it cannot distinguish between particle and fluid velocities; the measured velocity profile is presumably a mass or volume averaged value. However, no particle concentration data is given.

Most recently, Hookham[9] used a modified laser Doppler technique to measure the velocity and concentration profiles for the flow of concentrated suspensions in a rectangular channel. He measured the Doppler signals from a trace amount of fluorescent-dyed particles and found that the velocity profiles are similar to the ones given by previous researchers (*i.e.*, blunted near the center). The degree of blunting increases as the bulk particle concentration or the particle size-to-gap ratio increases. By counting the number of fluorescent Doppler signals, he also found that there are more particles near the centerline of the channel so that the concentration profile has a maximum near the center. However, the concentration data have a relatively large degree of scatter and can only provide a qualitative picture of the particle distribution within the flow channel.

From an analytical point of view, numerous advancements have been made for dilute systems by analyzing the suspension at the length scale of the particles. The most celebrated result is that due to Einstein, who showed for a dilute suspension of solid spheres,

$$\mu = \mu_0 \left(1 + \frac{5}{2} \Phi \right) \quad (3.1)$$

where μ is the suspension viscosity, μ_0 is the suspending fluid viscosity, and Φ is the volume fraction of the particles. Since this pioneering work, many researchers have extended Einstein's results for more general cases. Among these, the most relevant for the present study is the application to more concentrated suspensions, where particle interactions must be taken into account. For example, Frankel and Acrivos[10] used lubrication theory to calculate the energy dissipated in the neighborhood of small gaps between spheres to deduce the viscosity of a closely-packed

suspension. Also, by considering extensional flow, Batchelor[11] showed that

$$\mu = \mu_0 \left(1 + \frac{5}{2} \Phi + 6.2 \Phi^2 \right) \quad (3.2)$$

Others have proposed phenomenological relations for higher concentrations, such as that of Krieger and Dougherty[12]:

$$\mu = \mu_0 \left(1 - \frac{\Phi}{\Phi_m} \right)^{[\eta] \Phi_m} \quad (3.3)$$

where Φ_m is the maximum packing volume fraction and $[\eta]$ is the intrinsic viscosity (also known as the shape factor).

From the brief discussion above, it is clear that the volume fraction of particles (Φ) is critical in determining suspension properties. Of course, in most situations, the *bulk* particle volume fraction (Φ_{bulk}) is known. However, there could be *local* variations in the particle volume fraction (*e.g.*, due to particle migration). Consequently, one of the intrinsic problems of applying constitutive equations of the type mentioned above, is the requirement of *a priori* knowledge of the local particle volume fraction. Clearly, a comprehensive theory should predict the distribution of the particles simultaneously with the rheological and flow properties of the suspension.

A more satisfactory approach is the so-called Stokesian dynamics pioneered by Bossis and Brady[13]. Through numerical experiments, this method can dynamically simulate the motion of a suspension by accurately accounting for the hydrodynamic, as well as other possible interactions (such as electrostatic) between the particles. The advantage of this method is that it can relate the microscopic structure directly to the macroscopic properties such as the viscosity of the suspension. Many researchers have successfully applied this technique to elucidate the behaviors of various suspensions (*e.g.*, the rheology of a monolayer of particles[14, 15]). It should be pointed out that the simulations are usually computationally expensive, especially when a large number of particles are involved. Thus, this approach is not very practical for the study of suspension flows in complicated flow geometries, such as those encountered in industrially important processes.

Recently, Leighton and Acrivos[16], motivated by the anomalous experimental findings of Gadala-Maria and Acrivos [17], proposed a mechanism that can predict particle distribution of suspensions in shear flows. Specifically, these researchers found that the measured viscosity of a concentrated suspension of spherical particles in a Couette viscometer increases initially and then slowly decreases to a steady-state value. They attribute this variation of viscosity to the diffusive migration of particles, both in the direction normal to the plane of shear and normal to the direction of fluid motion within the plane of shear. The premise of their argument for such shear-induced particle migration is that the collisions of particles are irreversible. (Irreversible collisions can occur for two-particle collisions of spheres with finite amount of surface roughness or via three-body collisions.) By using scaling arguments, they suggest that the diffusion coefficients in the directions normal and within the plane of shear in a shear flow can be estimated as

$$D_{\perp} = K_{\perp} \frac{\Phi^2}{\mu} \frac{d\mu}{d\Phi} \dot{\gamma} a^2 \quad (3.4)$$

and

$$D_{\parallel} = K_{\parallel} \frac{\Phi^2}{\mu} \frac{d\mu}{d\Phi} \dot{\gamma} a^2 \quad (3.5)$$

where K_{\perp} and K_{\parallel} can be determined from experimental data. Since the suspension viscosity depends on the local particle concentration, Leighton and Acrivos successfully show that shear-induced particle migration can account for the aforementioned experimentally observed viscosity variation in a Couette viscometer. In fact, they have proposed that such particle migration effects can provide a new explanation for phenomena such as the blunting of velocity profiles in flows of concentrated suspensions through tubes due to nonuniform distribution of particles across the tube radius.

Adapting the approach of Leighton and Acrivos, Phillips *et al.*[18] computed the velocity and concentration profiles for concentrated suspensions in Couette and Poiseuille flows. This is accomplished by using Krieger's empirical relationship between suspension viscosity and particle concentration, and assuming the suspension

can be modelled as a Generalized Newtonian Fluid such that

$$\underline{\underline{\tau}} = \mu(\Phi)\underline{\underline{\dot{\gamma}}} \quad (3.6)$$

where $\underline{\underline{\tau}}$ is the deviatoric stress tensor and $\underline{\underline{\dot{\gamma}}}$ is the rate-of-strain tensor. The spatial dependence of particle concentration is then calculated using a diffusion equation developed by following the arguments of Leighton and Acrivos. In the case of Couette flows, Phillips *et al.* find that particle migration causes Φ to increase from the inner, rotating cylinder to the outer, stationary cylinder. These predicted concentration profiles agree very well with concentration profiles obtained from NMR studies of Couette flows for average particle concentration of 50% and 55%[18]. In addition, their calculations predict that the velocity decreases rapidly from the inner cylinder so that there is a relatively large region of almost stagnant suspension near the outer cylinder.

For axisymmetric Poiseuille flows, Phillips *et al.* predict that the particles tend to migrate towards the center so that the particle concentration is a maximum at the center and a minimum at the walls. Since the viscosity of the suspension increases as a function of particle concentration, this particle concentration profile leads to a velocity profile that is flattened near the center. This is in general agreement with the experimental results given by Karnis *et al.*[7] However, no NMR data for Poiseuille flows are given for comparison.

Clearly, to advance our ability to further understand the flow of suspensions, especially in flows of concentrated suspensions where particle-particle interactions are important, it is necessary to understand more about these phenomena through experimental investigation. The insights that we gain from experimental data will guide us towards further theoretical development. In particular, to fully evaluate the applicability of the theory of shear-induced migration of particles to concentrated suspension flow, it is necessary to acquire both concentration and velocity data for a variety of different flows.

Consequently, our objective is to develop an experimental technique that will

allow us to study the flow of concentrated suspensions. Specifically, we seek to measure local particle velocity and concentration (volume fraction) profiles for a suspension flowing in a rectangular channel. This flow configuration is chosen (as opposed to tube flow) because, as discussed later, it simplifies the experimental setup. More importantly, this relatively simple flow geometry facilitates the interpretation of the experimental results and the data can be used to compare with theories such as that of Leighton and Acrivos.

3.2 Experimental Technique

There are various experimental techniques available for the study of the motion of concentrated suspension flows. For example, as mentioned above, Karnis *et al.*[7] employed cinematography to do flow visualization studies of tube flow of suspensions. They were able to measure the velocity by analyzing the projected image of the film. The concentration of particles was measured by counting the number of tracer spheres. This method, being extremely labor intensive, usually cannot provide very accurate concentration data.

Other experimental techniques have been employed to study the motion of concentrated suspensions. For example, Kowalewski[8] used ultrasound Doppler anemometry to measure the velocity of a concentrated suspension flowing in a tube. The disadvantage of this technique is that it is not capable of measuring the concentration of the suspension. McMahon and Parker[20] used a microwave Doppler technique to measure suspension velocity in a tube flow. However, due to the relatively long wavelengths of microwave, the spatial resolution of their apparatus is not sufficient to provide local velocity data.

The specific experimental method that we employ here is Laser Doppler Anemometry (LDA). This technique is chosen over other experimental techniques for various reasons. First of all, it is capable of measuring velocity accurately with comparatively good spatial resolution without physically disturbing the flow. Second, the

LDA technique can be easily adapted to measure the particle volume fraction. Finally, LDA is now a widely available apparatus and can be easily set up in most laboratories.

We now proceed to discuss the fundamental principles of the experimental technique. Subsequently, we will discuss the particular details of the experimental setup in our laboratory for the study of concentrated suspension flows. LDA is now a well-known experimental technique; thus, its operating principles are briefly summarized in Appendix A (see Drain[21], and Durrani and Greated[22] for a detailed account of the principles and operation of LDA. Also, a similar experimental apparatus was used by Hookham[9] to study suspension flows; however, he obtained Doppler signals from fluorescent dye particles).

In order to study high concentration suspension flows using an optical experiment such as LDA, we must overcome the problem of optical turbidity, which is absent in the application of LDA to a pure fluid flow. To circumvent this problem, it is imperative that we minimize the optical turbidity of the suspension—through refractive index matching of the suspending and particulate phases. As we subsequently show, this is a crucial step in LDA measurements in suspension flow.

3.2.1 Refractive Index Match

Optical turbidity presents a major problem in the application of LDA to suspension flow, especially at high particle concentrations where the intensity of the laser beams is strongly attenuated. Since the strength of the Doppler signal is proportional to the intensity of the laser beams, attenuation of beam intensity can lead to lower signal to noise ratios (noise sources include random shot noise of the photomultiplier tube, spurious signals due to stray laser light, random noise generated by post-photomultiplier tube electronics, etc.[23]). Beyond the loss of intensity, multiple scattering can also “deflect” the laser beam from its original optical path; this can lead to ambiguity on the position of the measurement volume. However, these detrimental effects can be minimized by matching the refractive indices of the

particles and the suspending liquid.

Currently, we are interested in studying suspensions of neutrally buoyant spherical particles. The constraints of matching the density and index of refraction of the particles and suspending fluid restrain the type of particles that can be used in the experiment. The most important requirement is that they are transparent (*i.e.*, the imaginary part of the refractive index has to be negligible so that light is not absorbed). Furthermore, the particles have to be spherical and in the density range of the suspending fluid. The particles we have chosen are monodispersed polystyrene (with divinylbenzene cross-linkage) particles in the $30\mu\text{m}$ and $70\mu\text{m}$ size ranges. These particles, supplied by Duolite and Bio-Rad, are normally used for ion-exchange chromatography and therefore are available in bulk quantities commercially. Figure 3.1 shows a typical particle size distribution for these particles (here, the data for the nominally $30\mu\text{m}$ particles is shown).

As mentioned above, it is necessary to match not only the refractive indices but also the densities of the particulate and suspending phases. This dictates the use of a 3-component suspending phase so that the density and the refractive index can be adjusted independently. For the polystyrene particles, the refractive index is approximately 1.6 and the density is $1.05\text{g}/\text{cm}^3$. The liquids chosen for the suspending phase must have properties "bracketing" these values. The densities of most liquids are around the value of $1.05\text{g}/\text{cm}^3$. However, only a small number of liquids, such as the liquid phase of various aromatic compounds, have refractive index values as high as 1.6. Specifically, we have chosen the following liquids, 1-methylnaphthalene (Aldrich catalog number M5,680-8), 1-chloronaphthalene (Aldrich C5,765-0) and UCON-oil (polyalkylene-glycol, Union Carbide product number 75-H-90,000), to constitute the liquid phase. The first two components are aromatic compounds with relatively high refractive index. The UCON-oil is chosen because it is miscible with the naphthalenes and has a density and refractive index that can provide the required properties for this 3-component liquid. The densities and viscosities of these liquids are measured by a pycnometer and various sizes of

Cannon-Fenske viscometer respectively. The values are reported in Table 1.

To match the refractive indices of the two phases, several effects must be considered. First, the refractive index of the liquid used in these experiments depends strongly on temperature, as seen in Figure 3.2. The refractive indices of these liquids are measured by a Bausch & Lomb refractometer in conjunction with a Neslab temperature control unit. The temperature coefficient of the 3-component solution is about $-4.5 \times 10^{-4} \text{°C}$. On the other hand, the temperature dependence of the index of refraction of the polystyrene particles is $-1.42 \times 10^{-4} \text{°C}$ [24]. Thus, the degree to which the refractive indices can be matched depends on how well the temperature of the suspension can be controlled during the experiment.

The second factor is the wavelength dependence of the refractive index. It is crucial that the refractive indices be matched at the particular laser wavelength used in the experiment, namely 488 nm. Thus, it is not sufficient to simply match the refractive indices of the two phases by selecting the "clearest" suspension with the naked eye under ambient lighting. A more accurate and systematic method is necessary.

As far as we know, there is no known method to measure the refractive index of small particles accurately and conveniently. Thus, it is not possible to measure the refractive index of the polystyrene particles first, then find a solution of the correct composition so that it has the same refractive index. Nouri, Whitelaw and Yianneskis[25] demonstrated an ingenious way of matching the refractive indices of Diakon particles and a solution of tetraline and turpentine. They aimed a laser beam into the solution containing a large Diakon rod. By varying the composition of the solution (thus varying its refractive index), the laser beam passed through the system with different degrees of deflection. The point of perfect match was ascertained when the beam passed through the system without any deflection.

Unfortunately, we do not possess any bulk polystyrene sample that has the same molecular structure (hence the same refractive index) of the polystyrene-divinylbenzene particles. Thus, we were not able to match the refractive indices

at the specific laser wavelength using the experimental procedure described above. However, Conaghan and Rosen[26] developed a theory that quantifies the degree of light scattering in a suspension as a function of the refractive indices of the two phases. The transmittance of light through a sample of thickness x is defined as:

$$T \equiv \frac{I}{I_o} = e^{-\tau x} \quad (3.7)$$

where I_o is the intensity of the incident light and I is the intensity of the transmitted light. For a perfectly matched system, $T = 1$; otherwise, $T < 1$.

The turbidity, τ , is given by

$$\tau = \frac{3\phi K}{2d_p} \quad (3.8)$$

where ϕ is the particle volume fraction, d_p is the particle diameter and K is the scattering coefficient. Normally, it is necessary to solve Maxwell's equation to obtain K . However, for large particles ($d_p \gg \lambda$, the wavelength of the incident light), Van De Hulst[26] derived the following relationship

$$K = 2 - \frac{4}{\rho} \sin \rho + \frac{4}{\rho^2} (1 - \cos \rho) \quad (3.9)$$

where

$$\rho = \frac{2\pi d_p n_o}{\lambda} |m - 1| \quad (3.10)$$

and

$$m = \frac{n}{n_o} \quad (3.11)$$

Here, n_o and n are the refractive indices of the particle and the suspending fluid respectively.

We now discuss an experimental procedure that measures the transmittance of suspensions. Figure 3.3 shows the schematic diagram of the experiment. By measuring the intensity of the laser after it passes through the solution and the suspension, we can calculate the transmittance. In order to take into account the inherent turbidity and light absorbance of the solution, I_o is actually the transmitted intensity of the laser after it passes through the particle-free solution. Figure 3.4

shows the experimental results for $\Phi_{\text{bulk}} = 0.1\%$, $d_p = 30\mu\text{m}$, $\lambda = 488\text{nm}$ and various solution refractive indices.

To find the refractive index of the polystyrene particles (n_o), we choose n_o such that the following quantity

$$E \equiv \sum \left[T_e\left(\frac{n}{n_o}\right) - T_t\left(\frac{n}{n_o}\right) \right]^2 \quad (3.12)$$

is minimized. Here, $T_e(n/n_o)$ is the experimental transmittance, $T_t(n/n_o)$ is the theoretical transmittance and n is the refractive index of the solution. As expected, n_o should be the refractive index that the maximum transmittance occurs. The exact value of n_o that minimizes E is 1.5867 (at 20°C). The composition (by weight) of the liquid with this refractive index is 67.7% 1-methylnaphthalene, 10.4% 1-chloronaphthalene and 21.9% UCON-oil.

Using this value of n_o , a theoretical transmittance curve is plotted against the experimental data in Figure 3.5 for comparison. We can see that the experimental data fit the theoretical prediction quite well. It is clear, however, that $T_{e,\text{max}} < T_{t,\text{max}} = 1$. This is due to small but finite mismatch of the refractive indices and possibly a trace amount of impurities within the particles. In fact, it is this residual turbidity that allows a particle to produce a Doppler signal when it passes through the laser beams.

It should be pointed out here that, in the context of LDA, a refractive-index-matched suspension of (relatively) large particles is somewhat different from a fluid seeded with a large number of submicron particles (as in many LDA measurements of fluid flow). In the former, the particle size is of the order of the measurement volume so that the Doppler signal comes from a single particle. In the latter, many small particles could be present in the measurement volume and they all contribute to the signal both coherently and noncoherently (see Drain[27] for a more detailed discussion).

As stated earlier, the temperature coefficients of the refractive index of the solution and the polystyrene particles are different. Therefore, even when the refractive

indices of the two phases are matched (*i.e.*, $n/n_o = 1$) at a specific temperature, say 20°C, n/n_o will deviate from unity as temperature fluctuates during the course of the experiment. If the temperature is controlled to within $\pm 0.5^\circ\text{C}$, then

$$n = 1.5867 \pm 0.0002 \quad (3.13)$$

and

$$n_o = 1.5867 \pm 0.00007 \quad (3.14)$$

As a result, the variation in m becomes

$$m = 1.0 \pm 8 \times 10^{-5} \quad (3.15)$$

Using Equations 3.7 and 3.8, and assuming $\phi = 0.3$ and $x = 1.0\text{mm}$ (a typical gap width of the flow device), we find that the transmittance is reduced from unity to 0.99. Of course, the actual transmittance will be lower than this theoretical figure, due to impurities contained in the particles. In practice, it is found that controlling the temperature of the suspension to within $\pm 1^\circ\text{C}$ is sufficient.

As we have shown, the refractive indices of the two phases are matched at $n=1.5867$ at 20°C. However, the turbidity of the suspension slowly increases over a period of several days. In fact, the refractive index of the filtrate (*i.e.*, the suspending liquid) of an old suspension decreases with the age of the suspension. We believe that the polystyrene-divinylbenzene particles selectively absorb the lower molecular weight 1-methylnaphthalene and 1-chloronaphthalene, thus slowly changing the refractive indices of the suspending liquid *and* the particles. Consequently, the experiments are performed with fresh suspensions within a five-hour period, during which the turbidity of the suspension does not increase significantly.

3.3 Experimental Setup

The experimental setup is shown in Figure 3.6. The whole setup is secured on a pneumatically elevated optical table (Newport Research MST-48) for isolation from

vibration. The laser is a Spectra-Physics model 165 argon ion laser operating at 488 nm. All the optical elements are coated with antireflection coatings (for lenses and optical windows) or maximum reflection coatings (for mirrors), all optimized for the argon ion laser wavelength. After the laser beam exits the laser cavity, it is deflected by various mirrors (e1 and e2) to the appropriate position before entering the beam splitter (element e3). At the output end of e3 are two laser beams of equal intensity. Element e4, an integral optical element consisting of two mirrors and a reflecting prism, allows for easy adjustment of the beam separation through the movement of the prism. The final element (e5) before the beam enters the flow device is a plano-convex lens with a focal length of 120.8 mm. The beam separation distance is approximately 50 mm and the beam intersection angle is measured to be 26.6°. This lens serves to focus the two beams onto the same point (constituting the measurement volume mentioned in Appendix A) in the flow device. The LDA system operates under the forward-scatter mode. Therefore, the light collection optics are located on the other side of the flow device. The collection lens (e6) has a focal length of 50 mm (operating at f5.6). This lens focuses an image of the measurement volume onto the photomultiplier tube (Hamamatsu model R1617 operating at a potential of 0.85 kV). A pinhole is placed in front of the photomultiplier tube to prevent stray light from entering.

To calculate the effective size of the measurement volume, it is necessary to trace the size of the laser beam from the output of the laser. The beam radius at the output of the laser cavity is 0.21 mm and it has a beam divergence angle of 0.78 mrad[28]. The distance between the laser and the focusing lens (e5) is approximately 2.0 m. Thus, the beam radius at the front of lens e5 is 1.2 mm. Using the following equation derived from Gaussian optics[29],

$$r_o = \frac{\lambda f}{\pi r_i} \quad (3.16)$$

(λ is the wavelength, f is the focal length of a lens, r_i is the input beam radius and r_o is the output beam radius at the focal point) the beam radius at the focal point

is $15.6 \mu\text{m}$.

Using Equations A9, A10 and A11, the effective size of the measurement volume is given by

$$\begin{aligned}\Delta x_{eff} &= 109 \mu\text{m} \\ \Delta y_{eff} &= 44 \mu\text{m} \\ \Delta z_{eff} &= 48 \mu\text{m}\end{aligned}\tag{3.17}$$

When a particle passes through this volume, it scatters light that is collected by the collection lens onto the photomultiplier tube. Although the refractive indices of the two phases are closely matched, the small but finite difference allows the particles to scatter laser light at a detectable level for LDA. The photomultiplier tube in turn sends a signal to a TSI Model 1980B Counter-Type Signal Processor (see [30] for details of its operation). This signal processor has a built-in amplifier (with an overall gain that can be varied from -31 dB to +34 dB) to amplify the signal from the photomultiplier tube. As mentioned in Appendix A, the Doppler signal consists of both an ac-term and a dc-term. The dc-term is eliminated with a 1 kHz low limit filter; a 100 kHz high limit filter reduces high frequency noise produced by the photomultiplier tube and the amplifier. The signal processor then measures the time taken for a certain number of cycles in a Doppler signal burst using a high resolution clock with a resolution of $\pm 2\text{ns}$. The exact number of cycles depends on the strength of the signal; the stronger the signal, the higher the number of cycles. Typically, the number of cycles ranges from 10 to 20; also, the signal processor will ignore signals with less than 5 cycles/burst. An IBM PC-AT is interfaced with the signal processor to obtain the raw data (which consist of the number of cycles, n_c , the duration of the signal, t_s , and the time between successive signals, t_d). This data is stored in the computer and converted to useful data at the end of each experiment (see Appendix B for a flow chart of the FORTRAN program that collects and interprets the data).

3.3.1 Calculation of average particle velocity and volume fraction

In a typical experiment, 500 to 1000 data points are obtained for each point in the flow channel. For each Doppler signal processed by the signal processor, the computer receives 3 pieces of information: n_c , t_s and t_d . n_c is the number of cycles in the Doppler burst, t_s is the duration of this signal, and t_d is the time between the current and the previous signal. The Doppler frequency is simply given by

$$f_{\text{Doppler}} = \frac{n_c}{t_s} \quad (3.18)$$

Referring to Equation A7, the Doppler frequency can be converted into the z-component of the velocity as follows

$$v_z(x) = \frac{\lambda}{2 \sin \frac{\alpha}{2}} f_{\text{Doppler}} \quad (3.19)$$

where x denotes a specific point in the flow device. Using $\lambda = 0.488 \mu\text{m}$ and $\alpha = 26.6^\circ$, we obtain

$$v_z(\text{mm/s}) = 1.06 f_{\text{Doppler}}(\text{kHz}) \quad (3.20)$$

The average velocity is given by

$$\overline{v_z(x)} = \frac{\sum_{i=1}^N v_{zi}}{N} \quad (3.21)$$

and the standard deviation of the velocity is also calculated

$$\sigma_{v_z} = \frac{\sum_{i=1}^N [(v_{zi} - \overline{v_z})^2]^{\frac{1}{2}}}{(N - 1)} \quad (3.22)$$

To obtain the particle volume fraction, recall that the size of the measurement volume is of the order of a particle, as shown in Figure 3.7. The local particle concentration is proportional to

$$C(x) \propto \frac{1}{A_{mv} \Delta d} \quad (3.23)$$

where A_{mv} is the cross-sectional area of the measurement volume and Δd is the particle separation. The particle separation can be deduced from the experiment as follows

$$\Delta d = v_z t_d \quad (3.24)$$

The average local concentration is then given by

$$\begin{aligned} \overline{C(x)} &\propto \frac{1}{A_{mv} \overline{v_z} \overline{t_d}} \\ &\propto \frac{N}{A_{mv} \overline{v_z} \Delta t} \end{aligned} \quad (3.25)$$

where we have used

$$\begin{aligned} \overline{t_d} &= \frac{\sum_{i=1}^N t_{d_i}}{N} \\ &\equiv \frac{\Delta t}{N} \end{aligned} \quad (3.26)$$

Thus, if V_p is the volume of a particle, the particle volume fraction is given by

$$\begin{aligned} \overline{\Phi(x)} &\propto \overline{C(x)} V_p \\ &\equiv \frac{k}{\overline{v_z(x)} \Delta t} \end{aligned} \quad (3.27)$$

The proportionality constant, k , is determined by satisfying the following condition

$$\Phi_{\text{bulk}} = \frac{\int \overline{\Phi} dx}{\int dx} \quad (3.28)$$

3.3.2 Test of experimental system

In order to ascertain that the LDA system as well as the data collection system are functioning properly, the velocity profile in a rectangular channel flow of a Newtonian fluid (water) is measured. The flow channel has a gap width of 0.062 inch and an aspect ratio of 1:16. Figure 3.8 shows a schematic of the flow channel. The details of the flow system are explained in Section 3.4; since the aspect ratio of this channel is 1:16, the flow field at the center of the channel across the narrow dimension is approximately parabolic). The Doppler signals are obtained from

5 μm seeding particles. Figures 3.9-3.11 show the experimental data and theoretical (parabolic) profiles for three different pump speeds. For each of the three experiments, the velocity data is non-dimensionalized with the corresponding velocity at the centerline of the flow channel (*i.e.*, the maximum velocity). x is the location in the flow channel non-dimensionalized with half the gap width of the flow channel. In general, there is good agreement between the experimental data and the parabolic profile. However, we can see that the measured velocities are consistently higher than the theoretical values near the walls. We can offer two possible explanations for this observation. First, the signal to noise ratio near the walls is lower due to laser light reflected by the glass walls. This causes extraneous laser light to enter the receiving optics, thus increasing the noise level. More importantly, the TSI signal processor is equipped with a high pass filter to eliminate the d.c. (low frequency) part of the signal (see Section 3.3). This filter eliminates frequencies below 1 kHz, which corresponds to velocity of approximately 1 mm/s. The velocity near the wall is the lowest and the velocity gradient is the highest. Since the low frequency (velocity) signals are eliminated electronically, only the high frequency (velocity) signals are processed. Consequently, the average velocity obtained at a point near the wall is biased toward a higher value. (It should be pointed out that this problem can be resolved by using a Bragg cell to shift the frequency of one of the laser beams [22]. At present, however, our experimental setup is not equipped with a Bragg cell).

As discussed above, we match the refractive indices of the suspending and particulate phases to reduce multiple scattering of the laser. The exact quantitative difference between the Doppler signals obtained from suspensions with or without refractive index matching is difficult to predict. However, we have observed qualitative differences between the two cases. Figure 3.12 shows typical Doppler signals from a refractive-index-matched suspension as observed from a storage oscilloscope. The top trace shows a single Doppler burst that is free of noise and has a well-defined envelope. The bottom trace, obtained at a higher sweep rate, shows

a series of Doppler signals. On the other hand, Figure 3.13 displays Doppler signals from a suspension whose refractive indices are not matched. Here, the refractive index of the solution is 1.5858 (recall that the refractive index of the particles is 1.5867). The bulk volume fraction of the suspension is 15%. From the top trace, we can see that signal does not have a well-defined envelope and that a high frequency noise is present. The bottom trace is obtained at a higher sweep rate; compare to the trace shown in Figure 3.12, it does not show any well-defined Doppler bursts and appears to be noisier.

3.4 Experimental Procedure

In this section, we discuss the procedure for the operation of the experiment. (For readers who are interested in the finer points of performing the experiment, we have provided a step-by-step guide on the detailed operation of the experiment in Appendix C). First, we discuss the flow system employed in the experiment to study suspension flow in a rectangular channel. Figure 3.8 shows the detailed dimensions of the flow channel while Figure 3.14 shows the schematic diagram of the cross-section of the flow channel. The optical quality pyrex glass walls (available from Rolyn Optics, West Covina, California) are coated with a broad band multilayer dielectric coating and have a refractive index of 1.474. Besides the glass, the flow channel is made of black anodized aluminum (the black anodization reduces reflection of stray laser light). The precise gap width of the flow channel is determined by the thickness of the Lucite spacers, machined to within ± 0.001 inch. Two sets of twelve set screws are used to secure the glass plates to the aluminum pieces and to provide pressure to seal the two sides of the channel. To seal the top and bottom of the flow channel, rubber gaskets (1/16 inch thickness) are placed in between the top and bottom of the flow channel and the exit and entry blocks respectively. The exit and entry blocks have openings so that thermocouples can be placed inside to monitor the temperature of the suspension.

Figure 3.15 is a schematic of the overall flow system. A Harvard Apparatus model 951 infusion-withdrawal pump is used to maintain a (nearly) continuous flow through the closed-loop system (the flow is briefly interrupted when each stroke of the pump changes direction). Two precision-bore Robb infusion glass syringes of 50 cm³ capacity each are used for the pump. All the connection tubings are teflon-coated to provide chemical inertness. The reservoir is constantly stirred with a magnetic stirrer for the duration of the experiment.

For a typical experiment, the suspension is prepared by mixing the necessary amount of particles (depending on the desired bulk particle volume fraction of the suspension) in the liquid. Approximately 150 ml of suspension is required for the capacity of the overall flow system. The suspension is stirred manually to assure good mixing. It is then allowed to stand for 15-45 minutes so that any bubbles present in the mixture rise to the top. Since the turbidity of the suspension increases with time, the suspension is discarded after about 4 hours of experimentation.

3.5 Experimental Results and Discussion

To explore different possible phenomena associated with this experiment, we have performed the experiment for a range of values of the various important dimensionless parameters, namely, the bulk particle concentration (Φ_{bulk}), the particle size to gap ratio (κ), and the particle Reynolds number. They are defined as follow:

$$\Phi_{\text{bulk}} \equiv \frac{\text{particle volume}}{\text{particle + liquid volume}} \quad (3.29)$$

$$\kappa \equiv \frac{a}{d} \quad (3.30)$$

and

$$\text{Re}_p \equiv \frac{v_{n,0} \rho a}{\mu_{\text{liquid}}} \quad (3.31)$$

Here, a is the radius of the particle, d is the gap width of the flow channel, $v_{n,0}$ is the centerline (maximum) velocity of a Newtonian fluid under the same flowrate, ρ

is the density of the suspending liquid, and μ_{liquid} is the viscosity of the suspending liquid. The Reynolds number of the overall channel flow (Re) is simply given by:

$$\text{Re} = \frac{\text{Re}_p}{\kappa} \quad (3.32)$$

In Figure 3.16, we show the coordinate system of the experiment. The length scales are non-dimensionalized with half the gap width of the flow channel ($d/2$). All the data reported here were obtained from a point approximately 12.7 cm from the entrance of the flow channel. (Data obtained from approximately 12.7 cm and 7.6 cm from the entrance are identical within experimental error; thus, the data shown here are the steady profiles. Also, to study the evolution of the velocity and concentration profiles, we show preliminary data obtained at various positions downstream from an obstruction in Appendix D.)

To characterize the velocity profiles obtained in this study, we fit the data by the least square method using the empirical formula (see Kowalewski[8])

$$v_z = v_{z,0}(1 - |x|^b) \quad (3.33)$$

Here, $v_{z,0}$ is the particle velocity at the centerline (*i.e.*, $x = 0$). The exponent b is the adjustable parameter which we shall denote the bluntness factor. As with any empirical data fit, there is no *a priori* way of determining whether this formula is appropriate. Its applicability is judged solely by comparing the actual data with the best fit. As we have mentioned earlier, the velocity data deviate from the actual velocity near the wall due to the apparatus' inability to measure velocity below 1 mm/s. The deviation becomes apparent at $x \approx \pm 0.8$ (see Figures 3.9-11). Inclusion of these data points when curve-fitting the data to Equation 3.33 would systematically increase the bluntness factor, especially for the low flowrate cases. To maximize the reliability of the bluntness factor (b), we therefore arbitrarily ignore data obtained for $|x| > 0.8$ when performing the least square data fit.

In Table 2, we list the parameters for each of the experiments reported here. The bulk particle volume fraction ranges from 0.10 to 0.30, κ ranges from 0.010 to

0.057, while Re_p ranges from 2×10^{-3} to 1.2×10^{-2} . At this point, we are only able to obtain reliable data for volume fractions up to 0.3. This limitation exists for several reasons. First, the bulk viscosity of suspensions increases with particle concentration; we found that the syringe pump employed in our experiment cannot provide a smooth flowrate at particle concentrations higher than 0.3. Second, we did not observe (from the oscilloscope) distinct and well defined Doppler bursts at such high particle concentration. As explained earlier, it is necessary to allow the suspension to stand for a period of time so that any small bubbles created after stirring the suspension can rise to the top. We found that, for such high concentration, an exceedingly long duration of standing time is required. Apparently, the quality of the refractive index match degrades beyond an acceptable level within this period for a high concentration suspension. (For this same reason, we did not report any particle volume fraction profiles for the case of $\Phi_{\text{bulk}} = 0.3$ and $\kappa = 0.010$ since we did not observe distinct Doppler bursts from the oscilloscope.) We believe that a new combination of particles and suspending fluid, in which refractive indices of both phases remain constant, should improve this situation.

We will first discuss one specific set of data to highlight the general features. Figure 3.17 shows the particle velocity and volume fraction profiles for the case of $Re_p = 4.0 \times 10^{-3}$, $\kappa = 0.010$ and $\Phi_{\text{bulk}} = 0.10$. On the top half of the figure, the ordinate is the particle velocity non-dimensionalized with $v_{n,0}$. The symbols (o) are the experimental data and the solid curve is obtained from the data curve fit using Equation 3.33. The bottom graph in the same figure displays the particle volume fraction data. The solid line is obtained from a general data curve fit. The error of the volume fraction data is estimated to be about $\pm 10\%$ of its value. (Recall that these data are obtained by measuring the time, $\Delta t(x)$, required to obtain a certain number of Doppler signals at position x in the flow channel. It is observed from the experiments that the volume fraction obtained from two consecutive sets of 1000 data points at the same location can differ up to about 10%).

For completeness, the velocity and volume fraction data obtained from all the

experiments listed in Table 2 are placed in Appendix E. We shall concentrate our effort on understanding the general phenomena exhibited in these experiments with variations of the three aforementioned parameters (Φ_{bulk} , κ , and Re_p). The first and foremost feature of channel flow of suspensions is the blunting of the particle velocity profile, as indicated by the value of the bluntness factor, b . The results are graphically shown in Figure 3.18. Qualitatively, b increases as the bulk particle volume fraction increases. Furthermore, the amount of blunting increases only slightly when Φ_{bulk} increases from 0.1 to 0.2, but more dramatically when Φ_{bulk} increases from 0.2 to 0.3. The blunting also increases when the particle radius to gap width ratio (κ) increases. For the case of $\kappa = 0.010$, b ranges from about 1.9 to 2.6 as Φ_{bulk} increases from 0.1 to 0.3. For $\kappa = 0.057$, b ranges from about 2.5 to 3.5 as Φ_{bulk} increases from 0.1 to 0.3. Finally, for the small range of Reynolds number explored in this experiment, cursory observation of the data shows that the bluntness factor remains approximately constant within experimental error for different flowrates.

In addition to the average velocity, we also report the standard deviation of the velocity. The magnitude of the standard deviation of the velocity is governed by various effects. The variation in velocity measured at each point in the flow channel is partially due to the velocity gradient within the finite-size measurement volume. In some cases the velocity profiles are highly blunted near the center, which indicates the absence of any significant *macroscopic* velocity gradient. However, we can still measure a finite standard deviation of the velocity. This is an indication of the presence of local velocity fluctuations due to interactions (*e.g.*, collisions) among the particles. In fact, some of these interactions (*i.e.*, the irreversible collisions) lead to the particle migration discussed in Section 3.6. Currently, we are in the process of obtaining other statistical information pertaining to the experiment. For example, in addition to velocity fluctuation, a time correlation of t_d (the time between successive valid Doppler signals, *c.f.* Section 3.3.1) would provide a more detailed picture regarding the mechanisms of particle migration due particle-particle

interactions. This will be reported in a future paper.

The next question we wish to address is the volumetric flowrate of the solid and liquid phases through the flow channel. Since a constant volumetric flowrate pump is utilized for the experiment, the dimensionless volumetric flowrate can be given by

$$\begin{aligned} Q &\equiv \int_{-1}^1 (1 - |x|^2) dx \\ &= \frac{4}{3} \end{aligned} \quad (3.34)$$

The particle volumetric flowrate, Q_p , is given by

$$Q_p \equiv \int_{-1}^1 \Phi(x) \overline{v_z(x)} dx \quad (3.35)$$

If the particles are uniformly distributed in the flow channel (*i.e.*, $\Phi(x) = \Phi_{\text{bulk}}$) and the fluid velocity is identical to the particle velocity, then the particle volumetric flowrate is simply

$$Q_p = \Phi_{\text{bulk}} Q \quad (3.36)$$

In Figure 3.19, we show the quantity $Q_p/\Phi_{\text{bulk}}Q$ vs. Φ_{bulk} for various values of κ . We can see that $Q_p/\Phi_{\text{bulk}}Q > 1$ at $\Phi_{\text{bulk}} = 0.1$ and decreases below unity as Φ_{bulk} increases to 0.3. Furthermore, comparing data for various κ shows that $Q_p/\Phi_{\text{bulk}}Q$ is generally higher for smaller values of κ . The reason $Q_p/\Phi_{\text{bulk}}Q$ can be greater than unity is because at low concentration, the particle velocity profile is quite similar to the Newtonian parabolic profile. Since more particles are found near the center of the flow channel where the velocity is highest, the overall transport of the particulate phase becomes higher. However, when the bulk particle concentration increases, the quantity $Q_p/\Phi_{\text{bulk}}Q$ can become as low as 0.6. This means that there is a significant difference between the velocities of the particle and the fluid. We can offer one possible explanation that can contribute to this relatively large slip velocity. In a high concentration suspension, the particles are packed close to each other; because of their close proximity, they can be considered moving together as

a larger entity composed of a group of small particles. We know that the speed of a finite size, neutrally buoyant particle in Poiseuille flow decreases as the ratio of the size of the particle to the radius of the tube (or channel gap width) increases. Thus, it is possible that the ensemble of particles moves together at a slower speed than when the particles are isolated in a more dilute suspension. It should be pointed out here that since $Q_p/\Phi_{\text{bulk}}Q \neq 1$, the reciprocating nature of the syringe pump causes small fluctuation in the particle concentration in the reservoir between each stroke of the pump. However, since the capacity of the syringe is only a small fraction of the overall capacity of the flow system, a simple mass balance shows that this fluctuation is negligible.

The general observation regarding the particle volume fraction is that the particles tend to concentrate near the center of the flow channel. In order to quantify this phenomenon, we plot the quantity $\Phi_0/\Phi_{\text{bulk}}$ as a function of Φ_{bulk} , as shown in Figure 3.20 for four different values of κ . Here, Φ_0 is the particle volume fraction at the centerline of the flow channel. Since more particles are found near the center of the channel, it is obvious that $\Phi_0/\Phi_{\text{bulk}} > 1$ for all the experiments performed. However, the most striking behavior observed in these figures is that $\Phi_0/\Phi_{\text{bulk}}$ has a maximum near $\Phi_{\text{bulk}} = 0.2$ but *decreases* towards $\Phi_{\text{bulk}} = 0.3$. We believe that this apparent anomaly can be explained by the following qualitative argument. For a suspension of monodispersed particles, there is a maximum particle volume fraction (known as the maximum packing fraction) that depends on the structure of the suspension. The maximum packing fraction can range from 0.52 (for a simple cubic structure) to 0.637 (random close packing) to 0.74 (face-centered cubic or hexagonal close pack)[1]. The maximum particle volume fraction measured in the experiments for $\Phi_{\text{bulk}} = 0.3$ ranges approximately from 0.4 up to 0.6. This means that at $\Phi_{\text{bulk}} = 0.3$, the particles near the center of the flow channel are very closely packed and approach some maximum possible packing. Consequently, $\Phi_0/\Phi_{\text{bulk}}$ is lower for $\Phi_{\text{bulk}} = 0.3$ than $\Phi_{\text{bulk}} = 0.2$.

3.6 Comparison with theory

We have applied the approach of Phillips *et al.*[18, 31], based on the sheared-induced particle migration theory of Leighton and Acrivos, to calculate the concentration and velocity profiles in a rectangular channel flow (modelled as flow between two infinite plates). Since the extension from cylindrical Poiseuille flow to rectangular channel flow is straight forward, we will simply state the basic ideas here and refer the readers to the paper of Phillips for more details. They assume that the suspension can be modelled as a Generalized Newtonian fluid such that the deviatoric stress tensor

$$\underline{\underline{\tau}} = \eta(\Phi)\underline{\underline{\dot{\gamma}}} \quad (3.37)$$

where $\underline{\underline{\dot{\gamma}}}$ is the rate-of-strain tensor and η is the viscosity. The dependence of the viscosity on the particle volume fraction is given by Krieger's empirical formula[19]

$$\frac{\eta}{\eta_0} = \left(1 - \frac{\Phi}{\Phi_m}\right)^{-1.82} \quad (3.38)$$

where Φ_m is the maximum packing volume fraction, assumed to be about 0.68.

Using the theory of Leighton and Acrivos, Phillips *et al.* derived a diffusion equation for the particles

$$K_c \Phi \nabla(\dot{\gamma} \Phi) + K_\eta (\dot{\gamma} \Phi^2) \frac{1}{\eta} \frac{d\eta}{d\Phi} \nabla \Phi = 0 \quad (3.39)$$

Here, $\dot{\gamma}$ is the local shear rate, K_c is a proportionality constant related to the flux of particles caused by particle concentration variation in the suspension, while K_η is related to the flux of particles due to viscosity variation of the suspension (see [18] for a more detailed discussion on the derivation of Equation 3.39). Applying Equation 3.39 to the simple geometry of our problem (see Figure 3.21), it is easy to show that

$$\frac{\dot{\gamma} \Phi}{\dot{\gamma}_w \Phi_w} = \left(\frac{\eta_w}{\eta}\right)^{\frac{K_\eta}{K_c}} \quad (3.40)$$

Here, the subscript w refers to values evaluated at the wall and K_η and K_c are proportionality constants. From experimental data obtained from Couette flows, Phillips *et al.*[18] found that $K_c/K_\eta = 0.66$.

Using the momentum equation and Equation 3.37, we can show that

$$\dot{\gamma} = \frac{x}{\eta} \quad (3.41)$$

Combining Equations 3.40 and 3.41, and using the simplifying assumption that $1.82(1 - K_\eta/K_c) \approx -1$, we find

$$\Phi = \frac{\Phi_m}{1 + \alpha x} \quad (3.42)$$

where

$$\alpha = \frac{\Phi_m - \Phi_w}{\Phi_w} \quad (3.43)$$

and it is related to the bulk volume fraction (Φ_{bulk}) as

$$\begin{aligned} \Phi_{\text{bulk}} &= \int_0^1 \Phi dx \\ &= \frac{\Phi_m}{\alpha} \ln(1 + \alpha) \end{aligned} \quad (3.44)$$

Equation 3.42 predicts the particle distribution in the flow channel. Combining this equation with the momentum equation and Krieger's viscosity formula, we obtain

$$\frac{dv}{dx} = kx \left(\frac{x}{1 + \alpha x} \right)^{1.82} \quad (3.45)$$

Equation 3.45 is solved by the fourth-order Runge-Kutta method and k is a proportionality constant determined by the volumetric flowrate requirement

$$\int_0^1 v dx = \frac{2}{3} \quad (3.46)$$

Figures 3.22-24 show the theoretical predictions as well as the experimental data for three bulk particle concentrations ($\Phi_{\text{bulk}} = 0.1, 0.2,$ and 0.3) for the case of $\kappa = 0.019$. We have already discussed in the previous section the qualitative difference in the behavior of suspension flow for different values of κ . (For completeness, however, we have also included plots of comparison with data for other κ values in Appendix F.) The top half of each graph displays the velocity data and the bottom half shows the particle volume fraction data. We first discuss about the

velocity predictions and data. The *dotted-line* shows the theoretical velocity profile as calculated by Equation 3.45. It is apparent that it does not agree with the experimental data. As we have discussed earlier, we find that the particles are moving, on the average, slower than the fluid. However, the theory here assumes that the suspension can be treated as a Generalized Newtonian fluid and makes no distinction between particle and fluid velocities. We know that, from theoretical studies of single neutrally buoyant particle travelling in Poiseuille flow[32], there is a slip velocity between the particle and the fluid. For isolated particles, the slip velocity is of the order of the ratio of the particle size to gap width (or tube radius); for the relatively small particles used in the current experiment, it is only a few percent of the particle velocity. However, from the experimental results obtained here, it is clear that the slip velocity in the case of concentrated suspensions can be much higher. Thus, a more comprehensive theory should also take this phenomenon into account.

We now turn our attention to the bottom part of the graphs. Here, we show the particle volume fraction data compared to the theoretical prediction (*i.e.*, Equation 3.42). One observation is that the predicted Φ always equals the maximum value, Φ_m ($=0.68$) at the center. As discussed in detail in Phillips' paper, the diffusion of particles is based on the idea of particle collisions. The model assumes that the particles diffuse in the direction of lower shear rate with an opposing flux proportional to $\dot{\gamma}\nabla\Phi$. In our current geometry, the particles tend to diffuse toward the center of the gap. However the opposing flux vanishes at the center because the shear rate, $\dot{\gamma}$, also vanishes there. This effect is a manifestation of characterizing the particles as points instead of finite size entities which leads to the unrealistic assumption of no particle collisions at the center. This can be improved with refinement of the theory by taking into account the finite dimensions of the particles[18]. By doing so, the theory would allow for particle collisions even when the shear rate vanishes; thus, there would still be an opposing flux at the center of the flow channel. This would lead to a lower particle concentration near the center and a particle

concentration profile more similar to those obtained from experimental data.

To summarize, we find that the flow of concentrated suspensions in a rectangular channel is characterized by a blunting of the particle velocity profile. The magnitude of this blunting increases with the increase of either the bulk particle concentration of the suspension or the ratio of the particle size to the gap width of the channel. We are also able to measure the local particle volume fraction. It is found that the local particle volume fraction is not uniform across the gap width of the flow channel; in general, the particles tend to concentrate near the center of the flow channel. In certain instances (*i.e.*, $\Phi_{\text{bulk}} = 0.3$) the local particle concentration at the center approaches some maximum packing value near 0.65. One of the most interesting phenomena found in this study is that there exists a relatively large slip velocity between the particle and the fluid, as indicated by the calculation of the particle volumetric flowrate (*cf.* Figure 3.19). This slip velocity increases as the bulk particle concentration increases. Consequently, it is important that any comprehensive theory for the flow of suspension should take this phenomenon into account.

Bibliography

- [1] H.A. Barnes, J.F. Hutton and K.Walters; *An Introduction to Rheology*, Elsevier Science Publisher, Amsterdam, 1989.
- [2] R. Fahraeus and T. Lindquist; *Am. J. Physiol.*, **96**, 562, 1931.
- [3] S. Segré and A. Silberberg; *J. Colloid Sci.*, **18**, 312, 1963.
- [4] B.P. Ho and L.G. Leal; *J. Fluid Mech.*, **65**, 365, 1974.
- [5] S.I. Rubinow and J.B. Keller; *J. Fluid Mech.*, **11**, 447, 1961.
- [6] P.G. Saffman; *J. Fluid Mech.*, **22**, 385, 1965.
- [7] A. Karnis, H.L. Goldsmith and S.G. Mason; *J. Colloid Sci.*, **22**, 531, 1966.
- [8] T.A. Kowalewski; *Arch. Mech.*, **32**, 857, 1980.
- [9] P.A. Hookham; Ph.D. Thesis, California Institute of Technology, 1985.
- [10] N.A. Frankel and A. Acrivos; *Chem. Eng. Sci.*, **22**, 847, 1967.
- [11] G.K. Batchelor; *J. Fluid Mech.*, **83**, 97, 1977.
- [12] I.M. Krieger and T.J. Dougherty; *Trans. Soc. Rheol.*, **3**, 137, 1959.
- [13] J.F. Brady and G. Bossis; *Ann. Rev. Fluid Mech.*, **20**, 111, 1988.
- [14] G. Bossis and J.F. Brady; *J. Chem. Phys.*, **80**, 5141, 1984.
- [15] J.F. Brady and G. Bossis; *J. Fluid Mech.*, **155**, 105, 1985.

- [16] D. Leighton and A. Acrivos; *J. Fluid Mech.*, **181**, 415, 1987.
- [17] F. Gadala-Maria and A. Acrivos; *J. Rheol.*, **24**, 799, 1980.
- [18] R.J. Phillips, R.C. Armstrong, R.A. Brown, A. Graham and J.R. Abbot; "A Generalized Newtonian Constitutive Model for Concentrated Suspensions that Accounts for Shear-Induced Particle Migration", submitted to *Phys. Fluid A*.
- [19] I.M. Krieger, *Advan. Colloid Interface Sci.*, **3**, 111, 1972.
- [20] T.A. McMahon and R.R. Parker, *Trans. Soc. Rheol.*, **19**, 445, 1975.
- [21] L.E. Drain; *The Laser Doppler Technique*, John Wiley and Sons, 1980.
- [22] T.S. Durrani and C.A. Greated; *Laser Systems in Flow Measurement*, Plenum Press, New York, 1977.
- [23] R.J. Adrian, *TSI publication*, **IV**, Issue 1, 1978.
- [24] J. Timmermans; *Physico-chemical constants of pure organic compounds, volume 2*, Elsevier Publishing Company, 1965.
- [25] J.M. Nouri, J.H. Whitelaw and M. Yianneskis; *Third Int. Symp. on Applications of Laser Anemometry to Fluid Mech.*, Portugal, 1986.
- [26] B.F. Conaghan and S.L. Rosen; *Polymer Engineering and Science*, **2**, 12, 1972.
- [27] L.E. Drain; *J. Phys. D: Appl. Phys.*, **5**, 481, 1972.
- [28] *Spectra-Physics Model 165 Instruction Manual*, Spectra-Physics Inc., Mountain View, California.
- [29] A. Yariv; *Optical Electronics*, CBS College Publishing, New York, 1985.
- [30] *TSI Model 1980B Counter Type Signal Processor Instruction Manual*, Thermosystems Inc., St. Paul, 1982.

[31] Private communication.

[32] J. Happel and H. Brenner; *Low Reynolds Number Hydrodynamics*, Prentice-Hall, New Jersey, 1965.

Figure Captions

1. Particle size distribution curve for the nominally $30\ \mu\text{m}$ particles.
2. Temperature dependence of refractive indices.
3. Schematic diagram of turbidity experiment.
4. Experimental results from a typical turbidity experiment: $\Phi_{\text{bulk}} = 0.1\%$, $d_p = 30\ \mu\text{m}$, $\lambda = 488\text{nm}$.
5. Comparison of theoretical transmittance curve with experimental data assuming $n_o = 1.5867$.
6. Schematic diagram of LDA experiment.
7. Illustration for explanation of calculating the particle volume fraction.
8. Schematic diagram of flow channel.
9. Comparison between experimental data and parabolic velocity profile. $V_{\text{max}} = 8.0\ \text{mm/s}$ and channel gap width = 0.062 inch.
10. Comparison between experimental data and parabolic velocity profile. $V_{\text{max}} = 15.9\ \text{mm/s}$ and channel gap width = 0.062 inch.
11. Comparison between experimental data and parabolic velocity profile. $V_{\text{max}} = 31.5\ \text{mm/s}$ and channel gap width = 0.062 inch.
12. Oscilloscope traces obtained from a refractive-index-matched suspension.
13. Oscilloscope traces obtained from a suspension whose refractive indices are not matched.

14. Schematic diagram of cross-section of the flow channel.
15. Schematic diagram of flow system.
16. Coordinate system of the experiment.
17. Particle velocity and volume fraction data for $Re_p = 4.0 \times 10^{-3}$, $\kappa = 0.010$ and $\Phi_{\text{bulk}} = 10\%$.
18. Bluntness factor (b) vs. Φ_{bulk} for $\kappa = 0.010, 0.019, 0.032$ and 0.057 .
19. $Q_p/\Phi_{\text{bulk}}Q$ vs. Φ_{bulk} for $\kappa = 0.010, 0.019, 0.032$ and 0.057 .
20. $\Phi_o/\Phi_{\text{bulk}}$ vs. Φ_{bulk} for $\kappa = 0.010, 0.019, 0.032$ and 0.057 .
21. Geometry for solving the diffusion problem.
22. Comparison between predicted and experimental velocity and concentration data for $\Phi_{\text{bulk}} = 0.1$
23. Comparison between predicted and experimental velocity and concentration data for $\Phi_{\text{bulk}} = 0.2$
24. Comparison between predicted and experimental velocity and concentration data for $\Phi_{\text{bulk}} = 0.3$

Table Captions

1. Viscosities and densities of the fluids used in the experiment at various temperatures.
2. List of experiments performed.

PARTICLE SIZE DISTRIBUTION

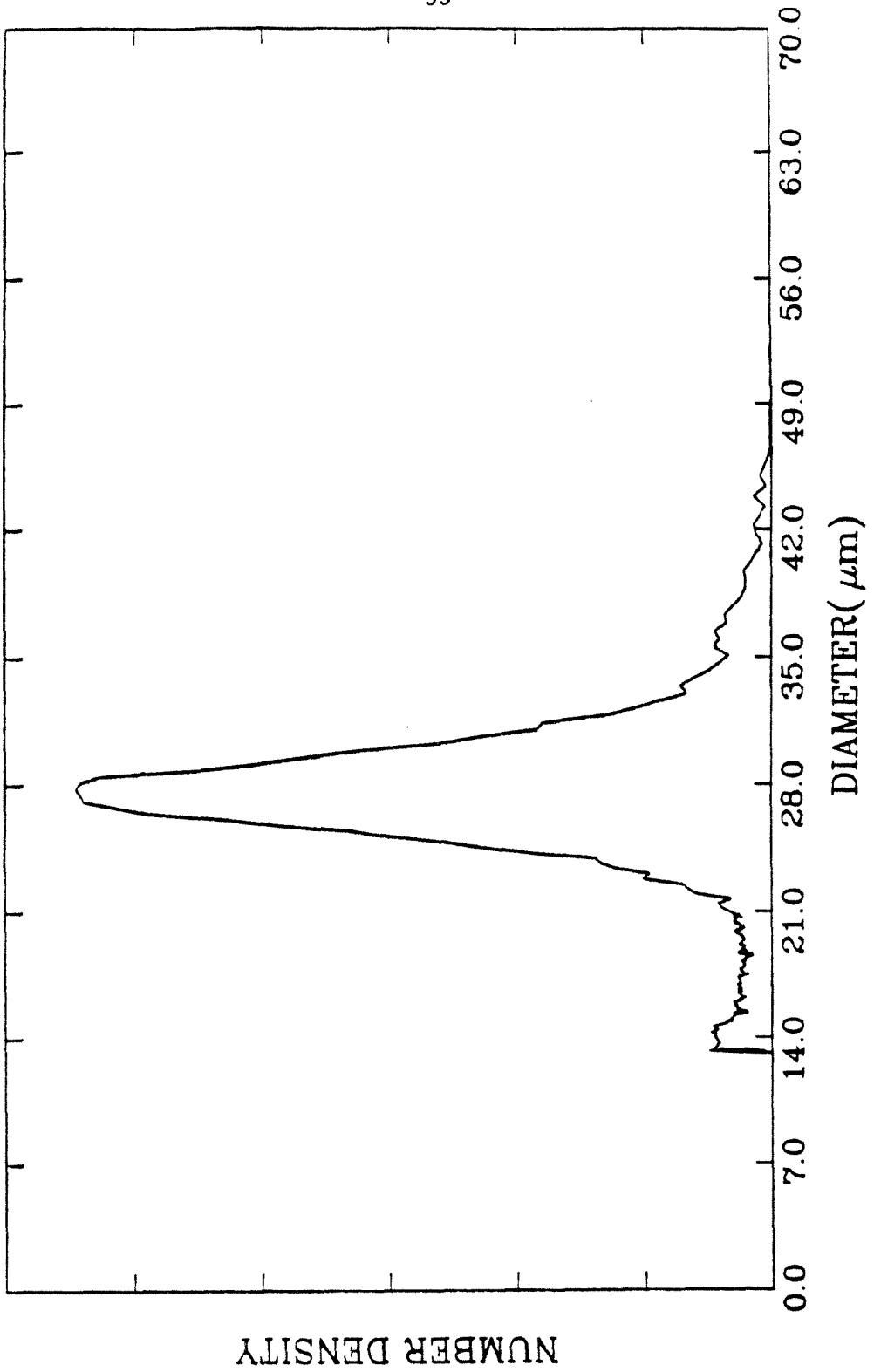


Figure 3.1

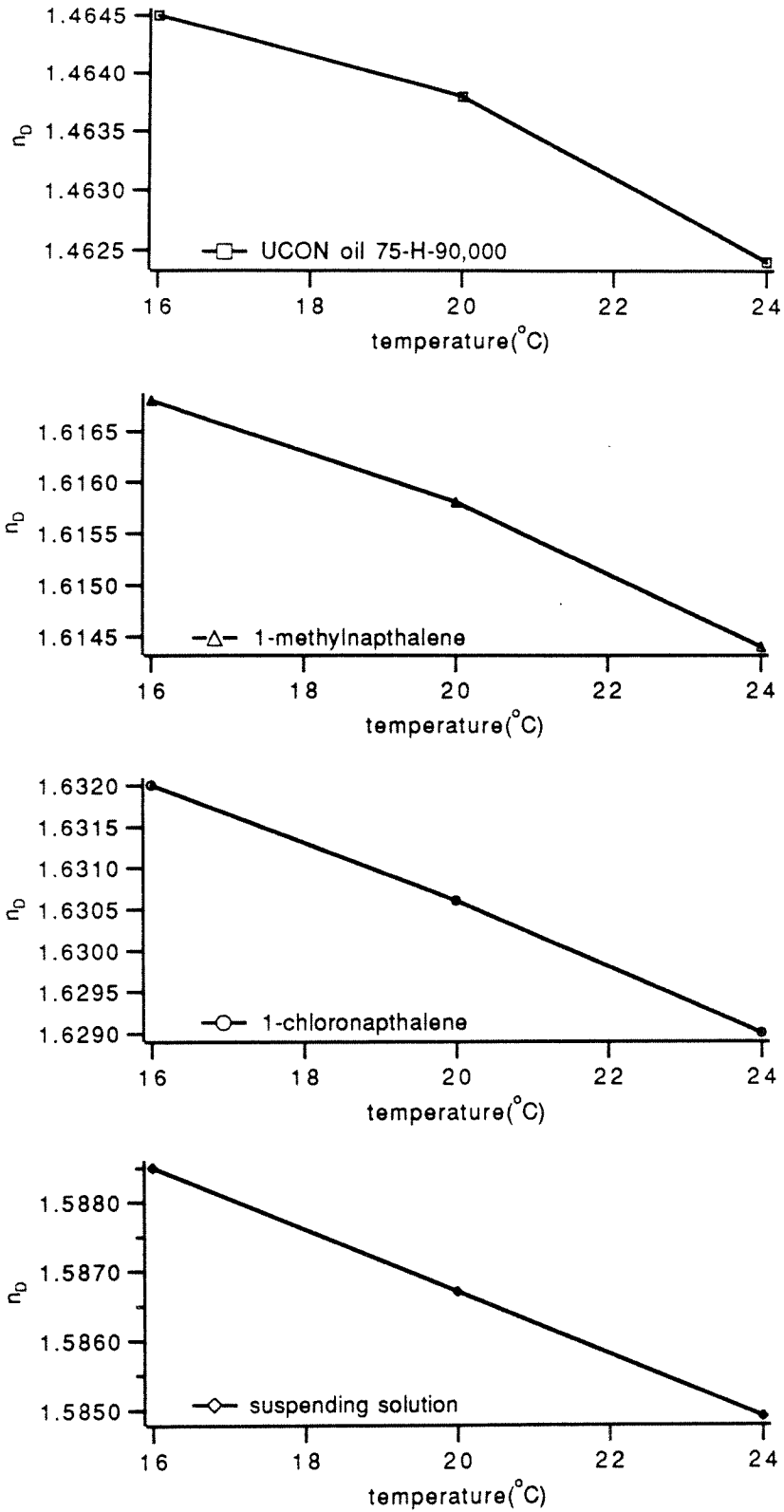


Figure 3.2

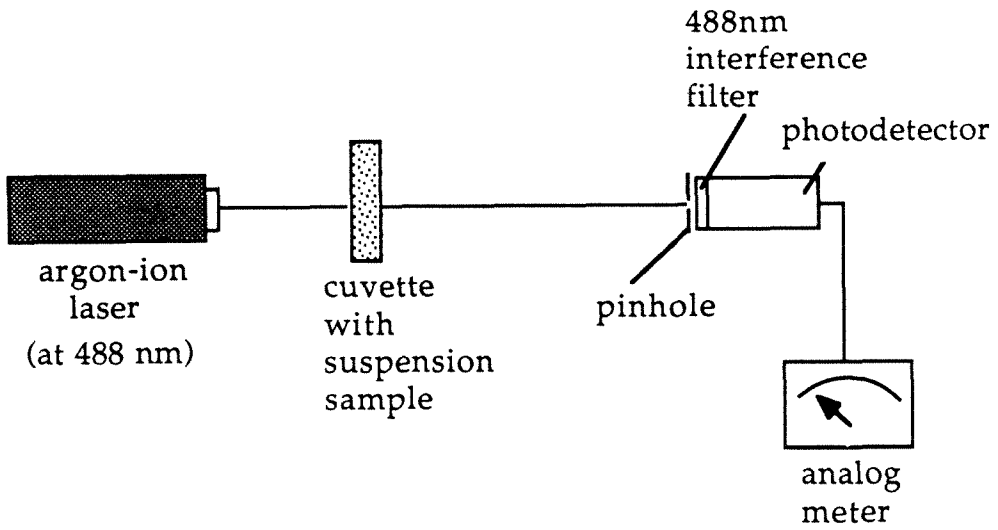


Figure 3.3

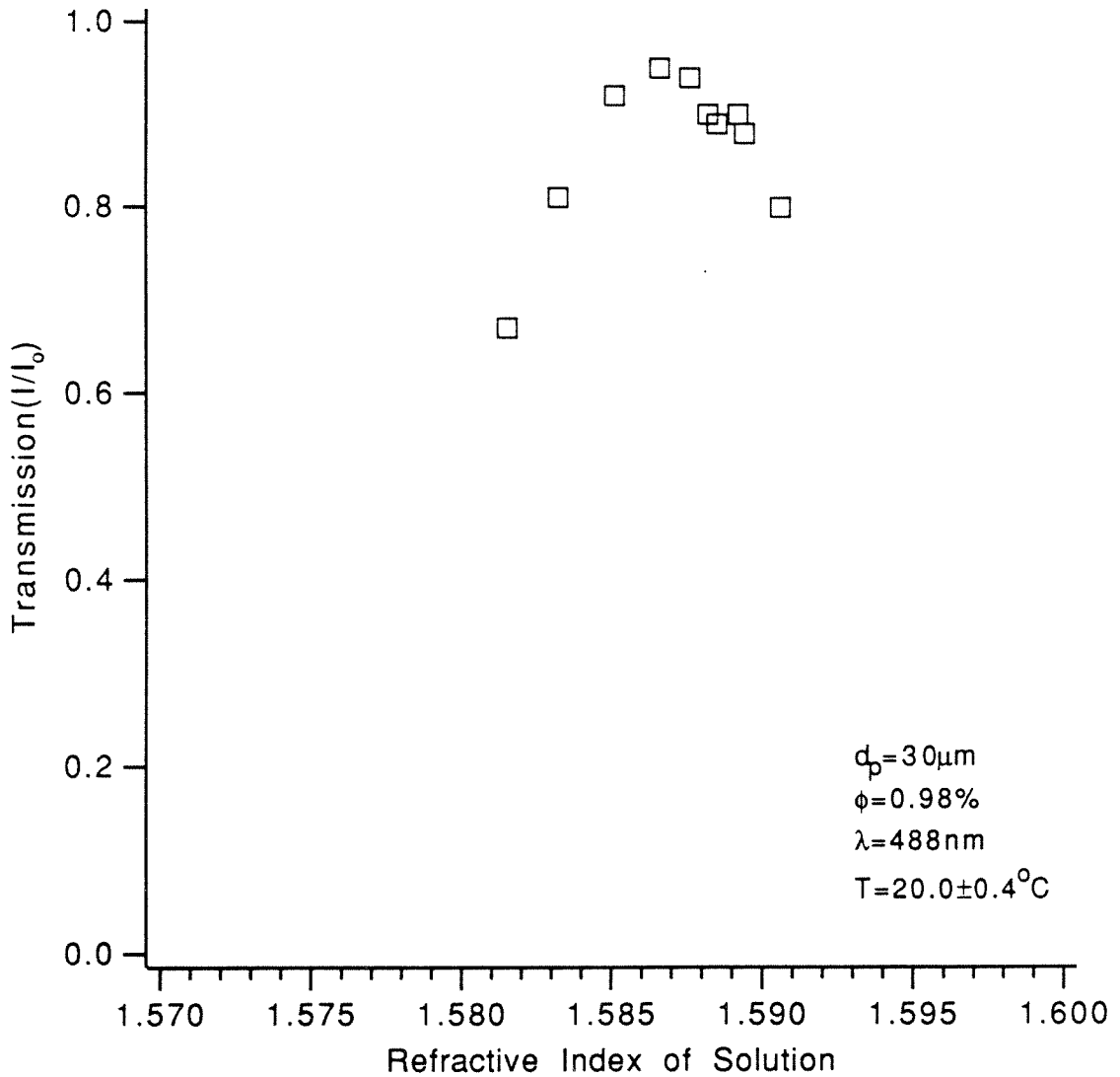


Figure 3.4

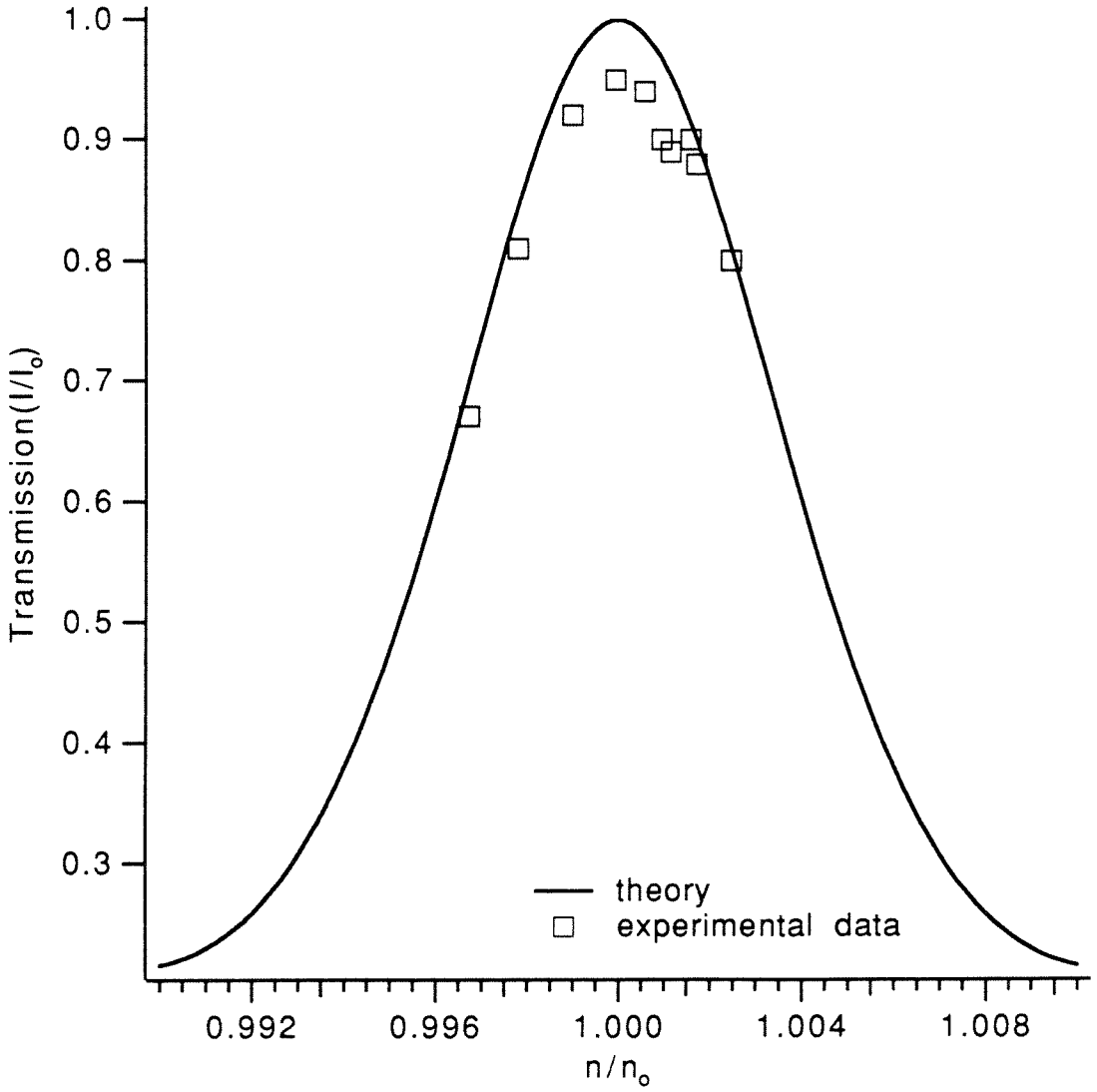


Figure 3.5

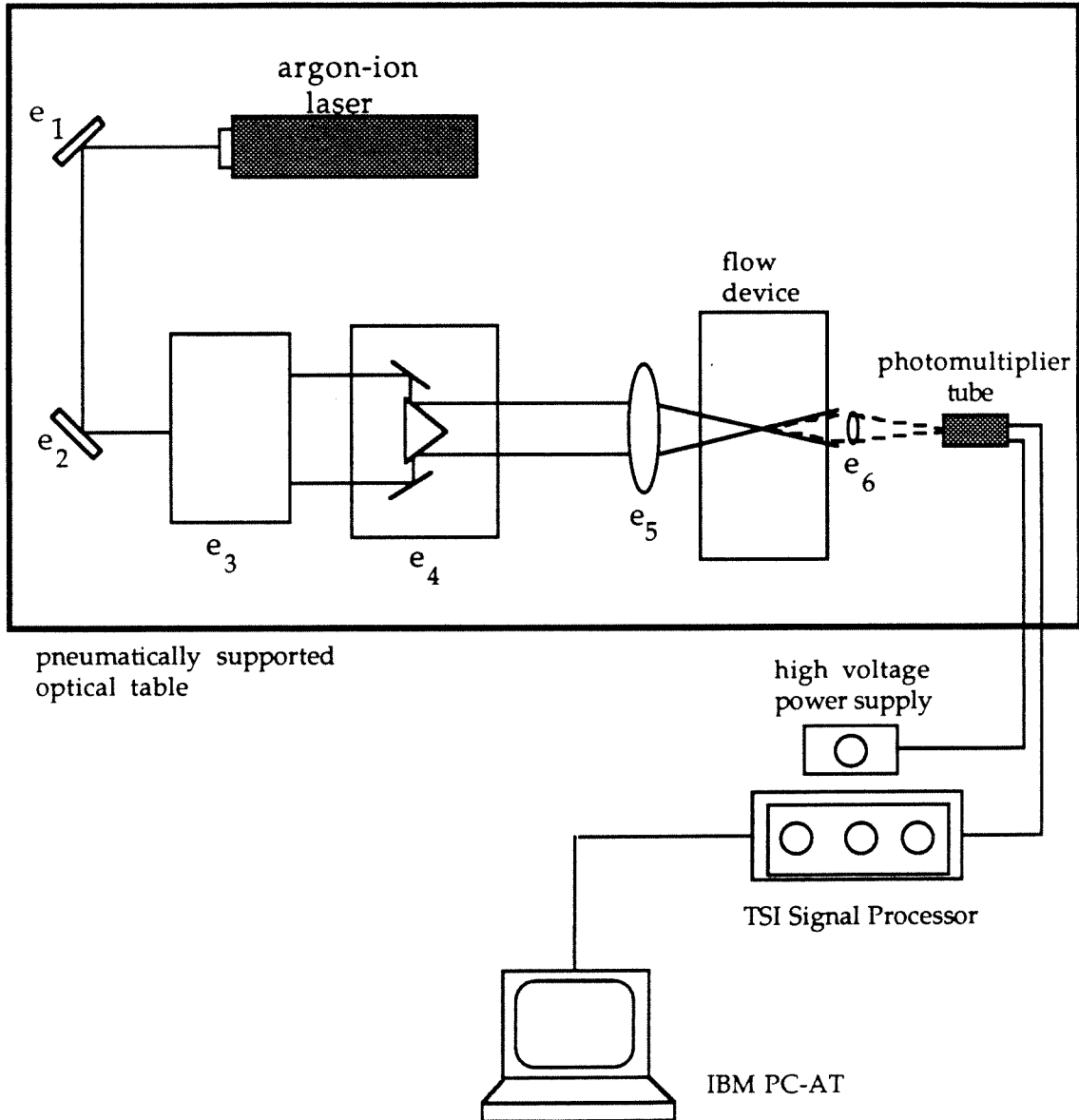


Figure 3.6

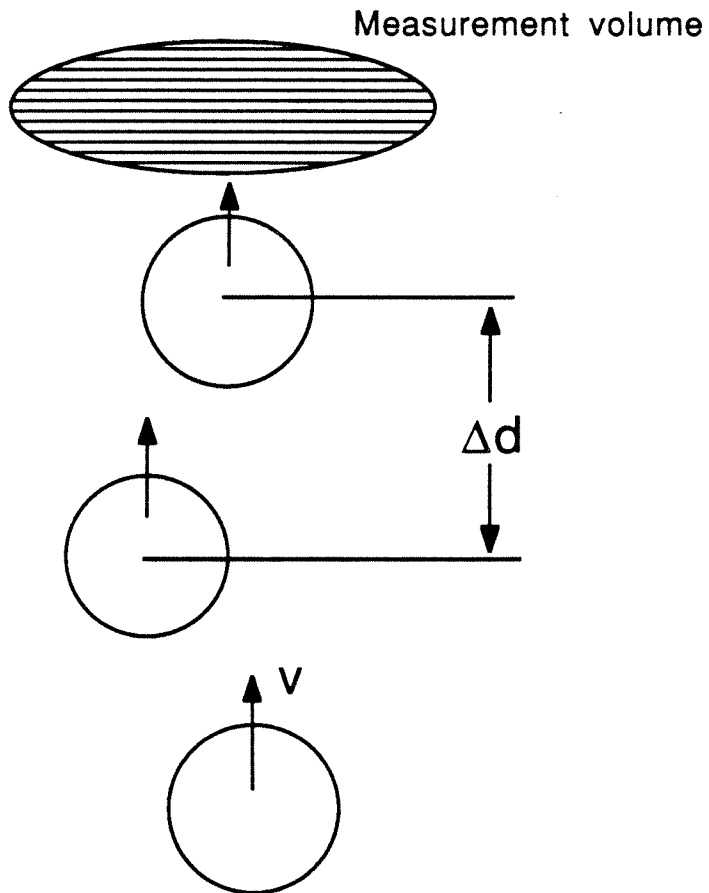


Figure 3.7

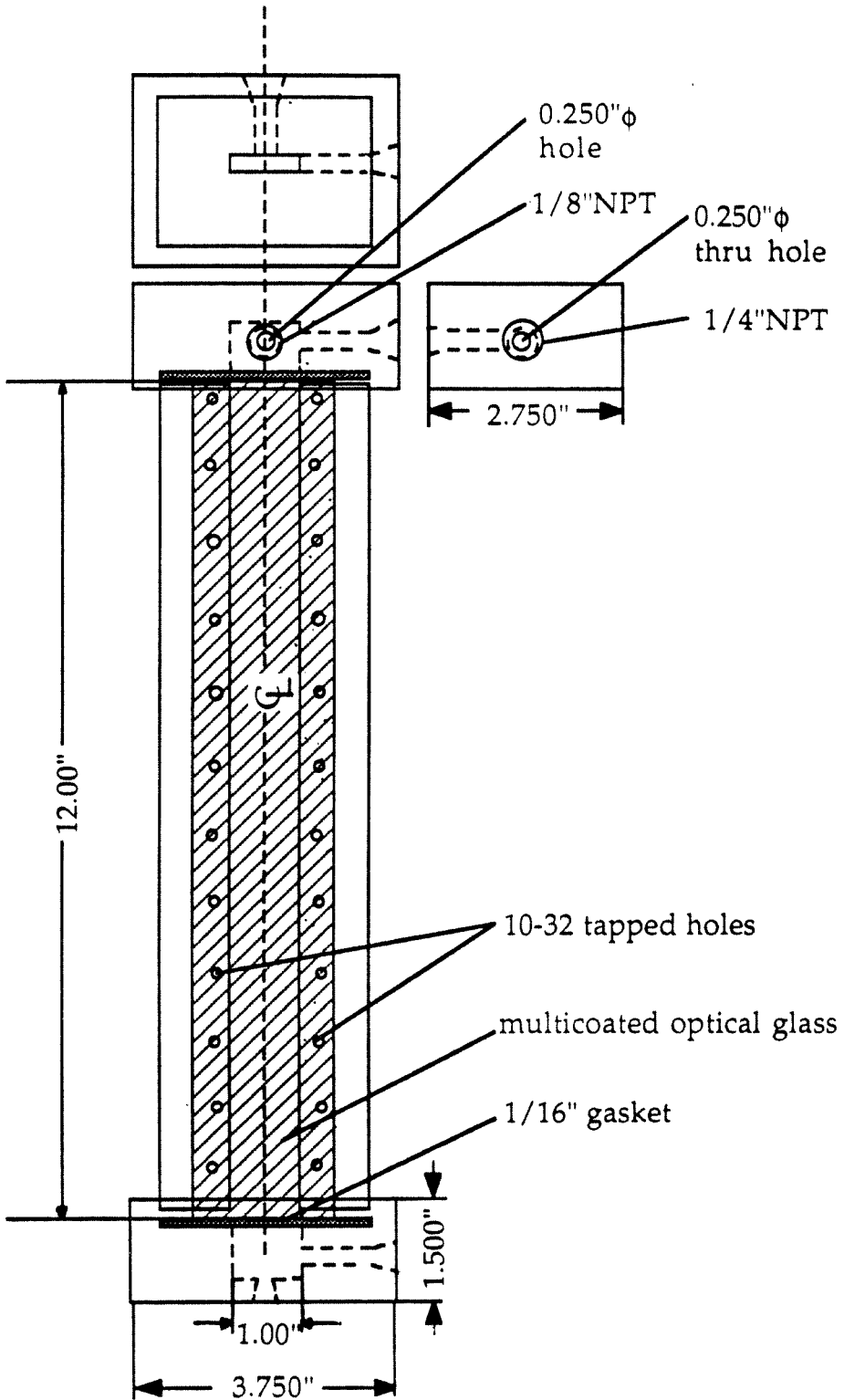


Figure 3.8

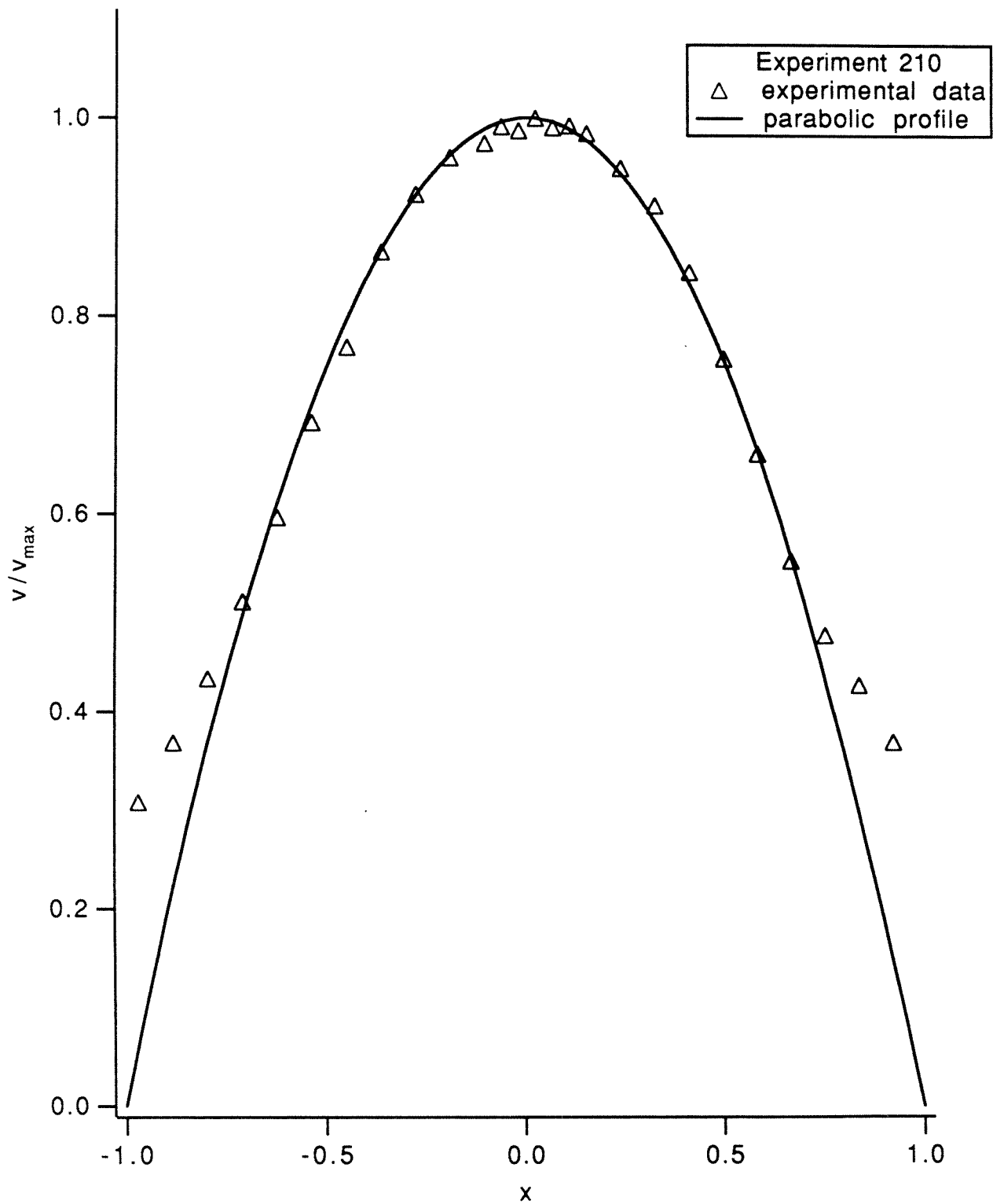


Figure 3.9

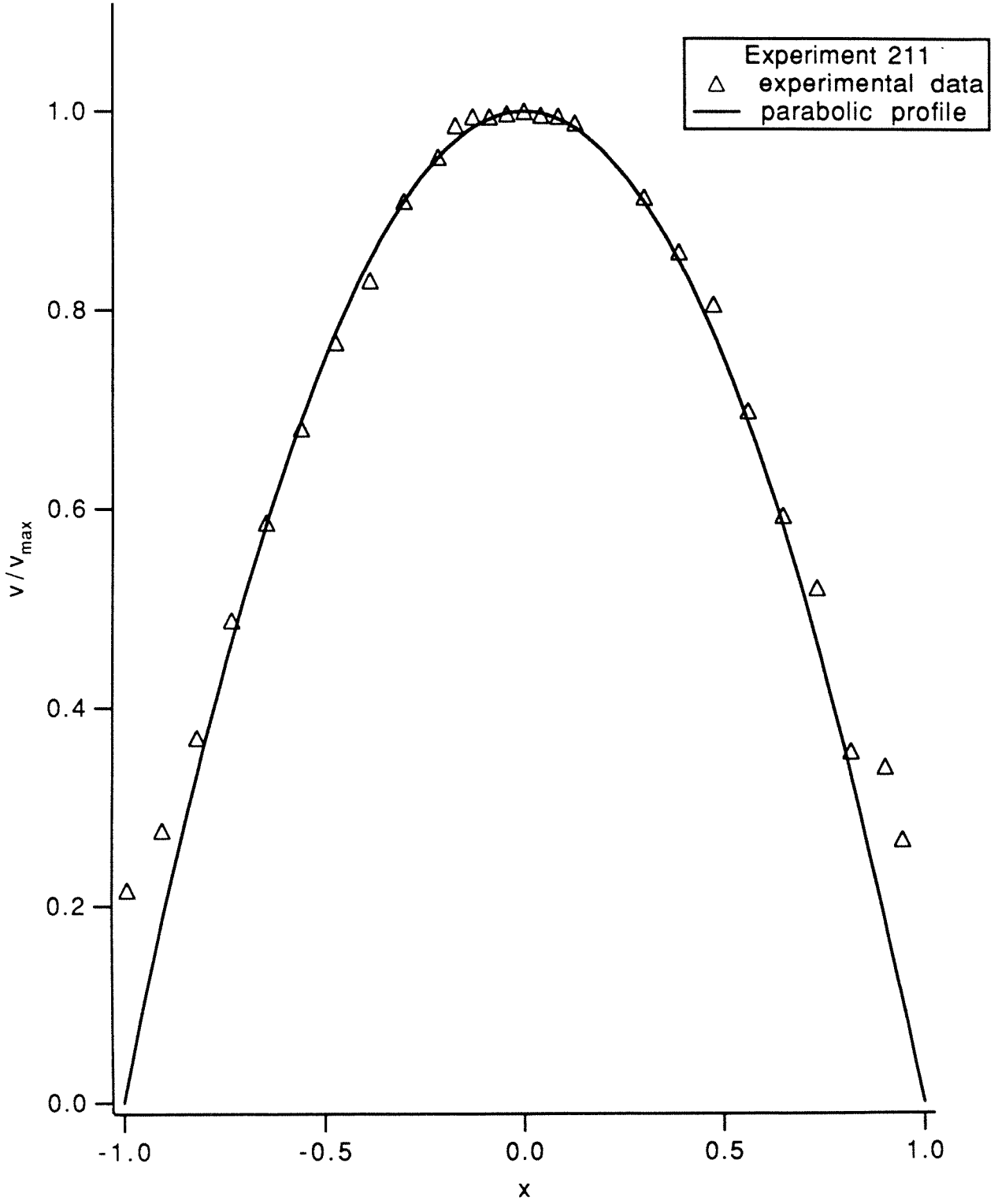


Figure 3.10

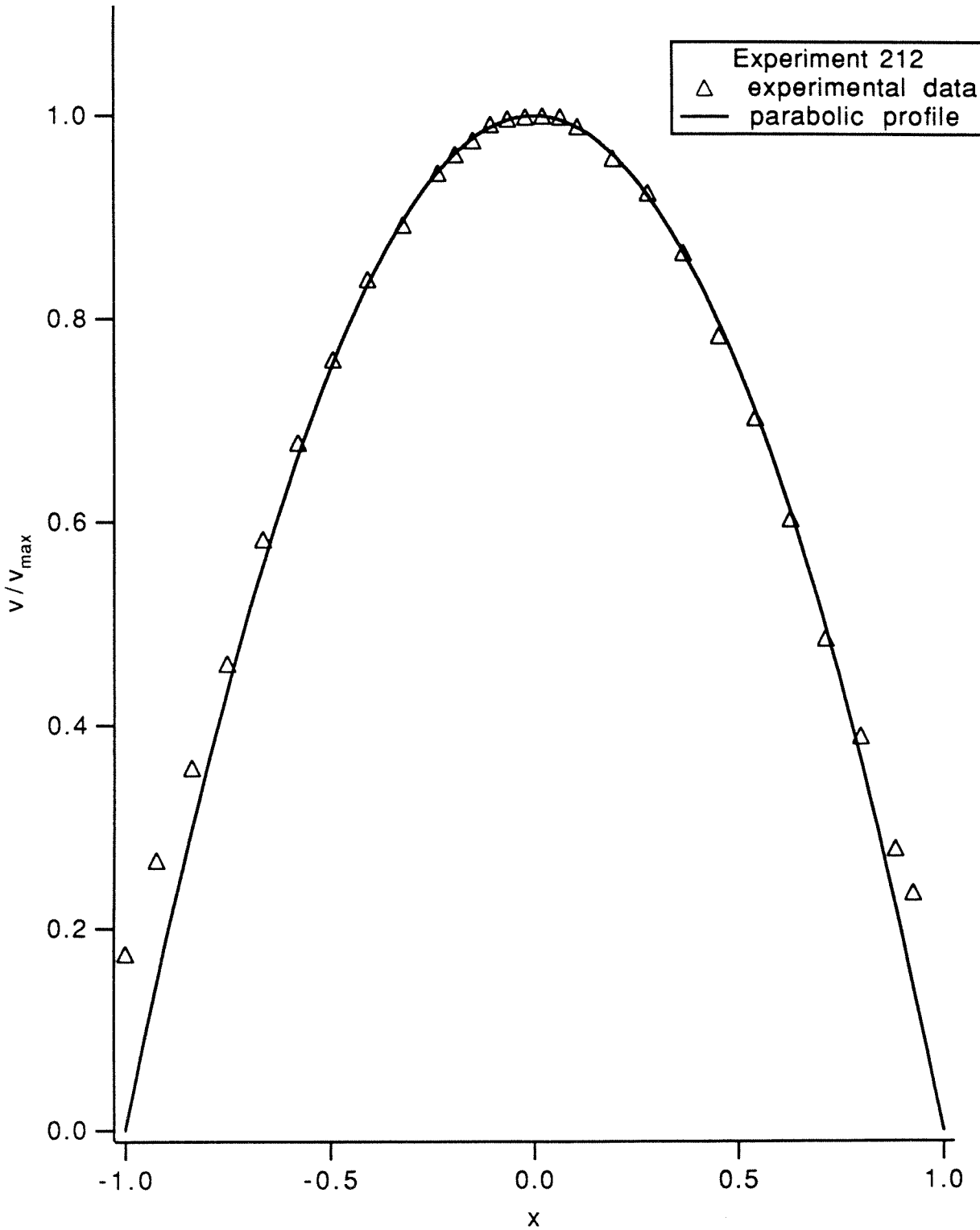
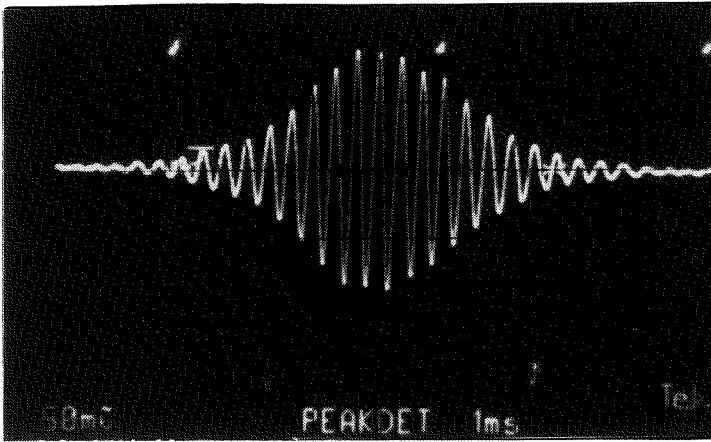
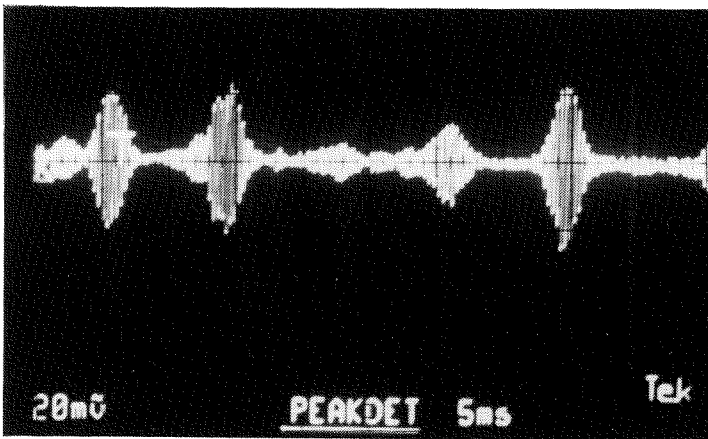


Figure 3.11

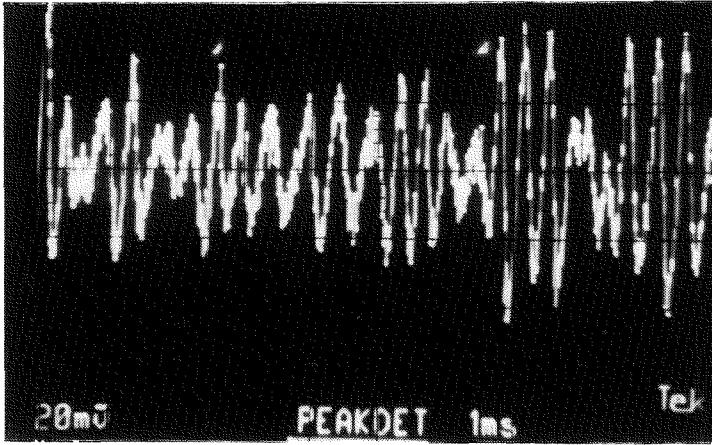


Trace at low sweep rate

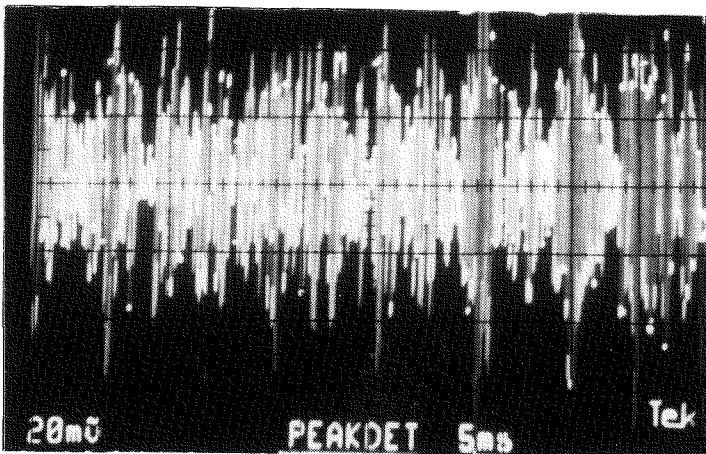


Trace at high sweep rate

Fig 3.12

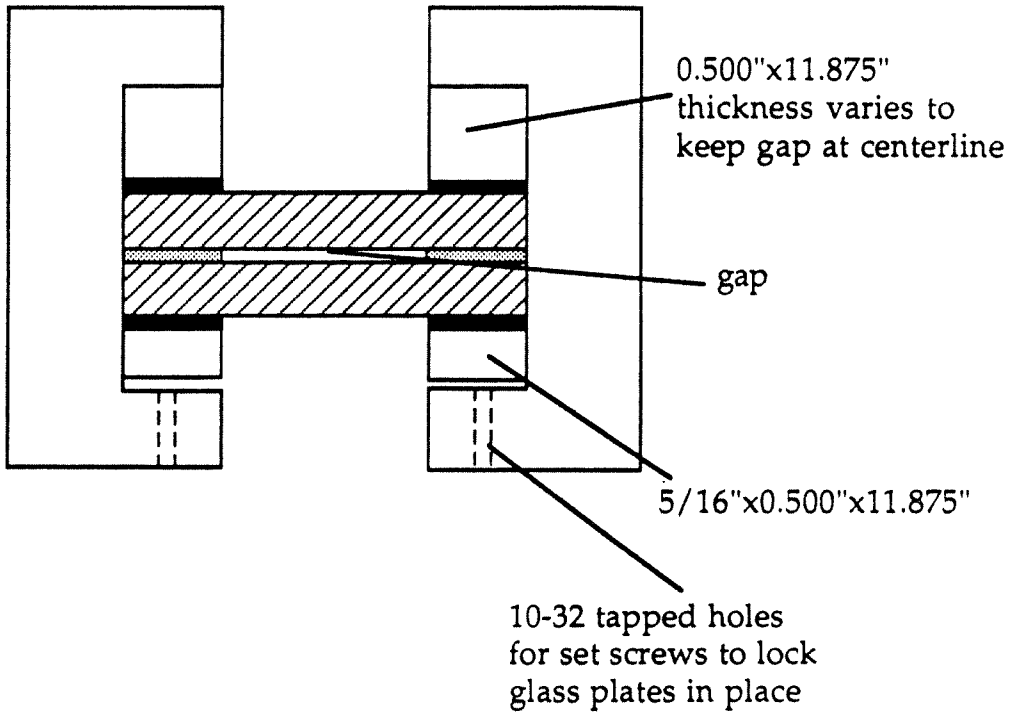


Trace at low sweep rate



Trace at high sweep rate

Fig 3.13



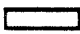



-  Aluminum
-  Teflon(0.010"x0.50"x12")
-  Optical Glass Plates(0.250"x2.00"x12.00")
-  Lucite Spacer (0.50"x12.00", various thickness)

Figure 3.14

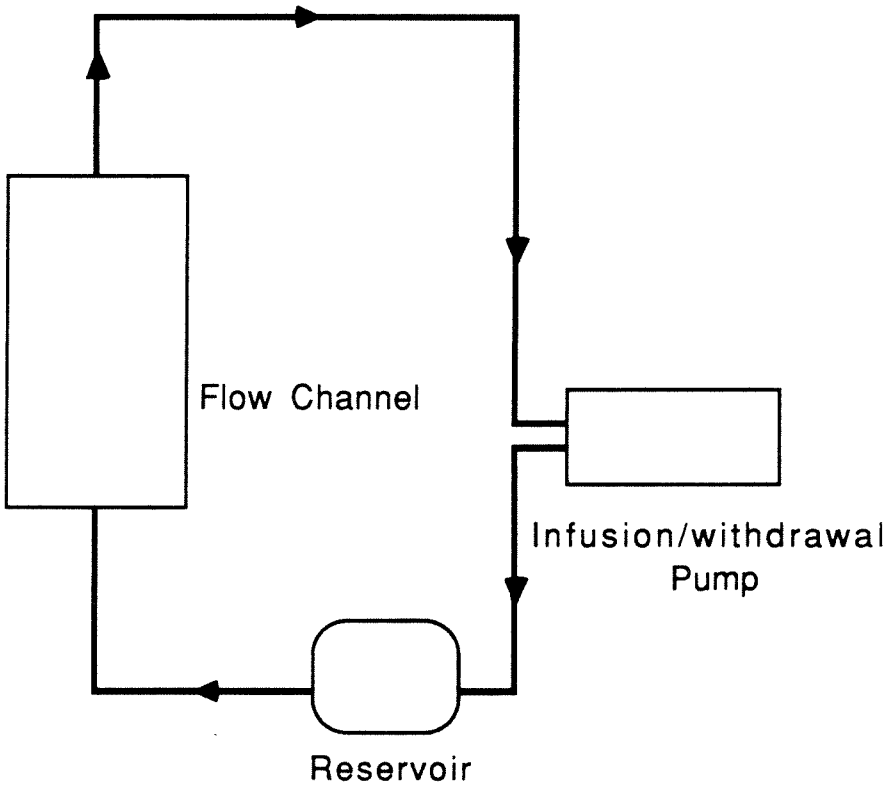


Figure 3.15

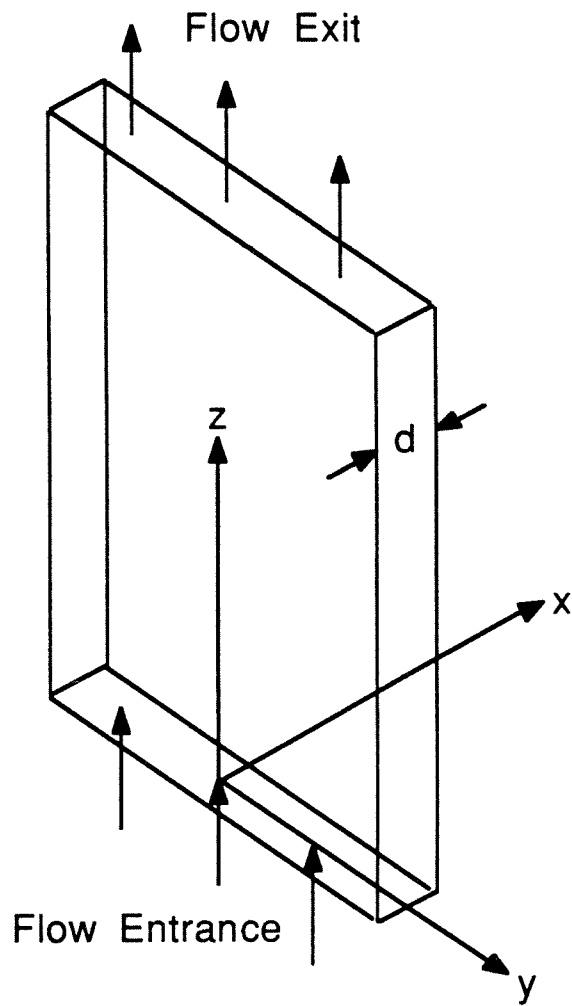


Figure 3.16

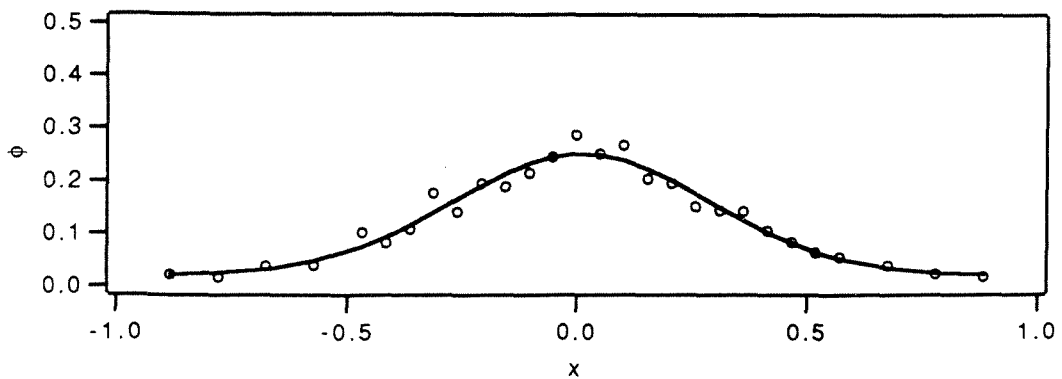
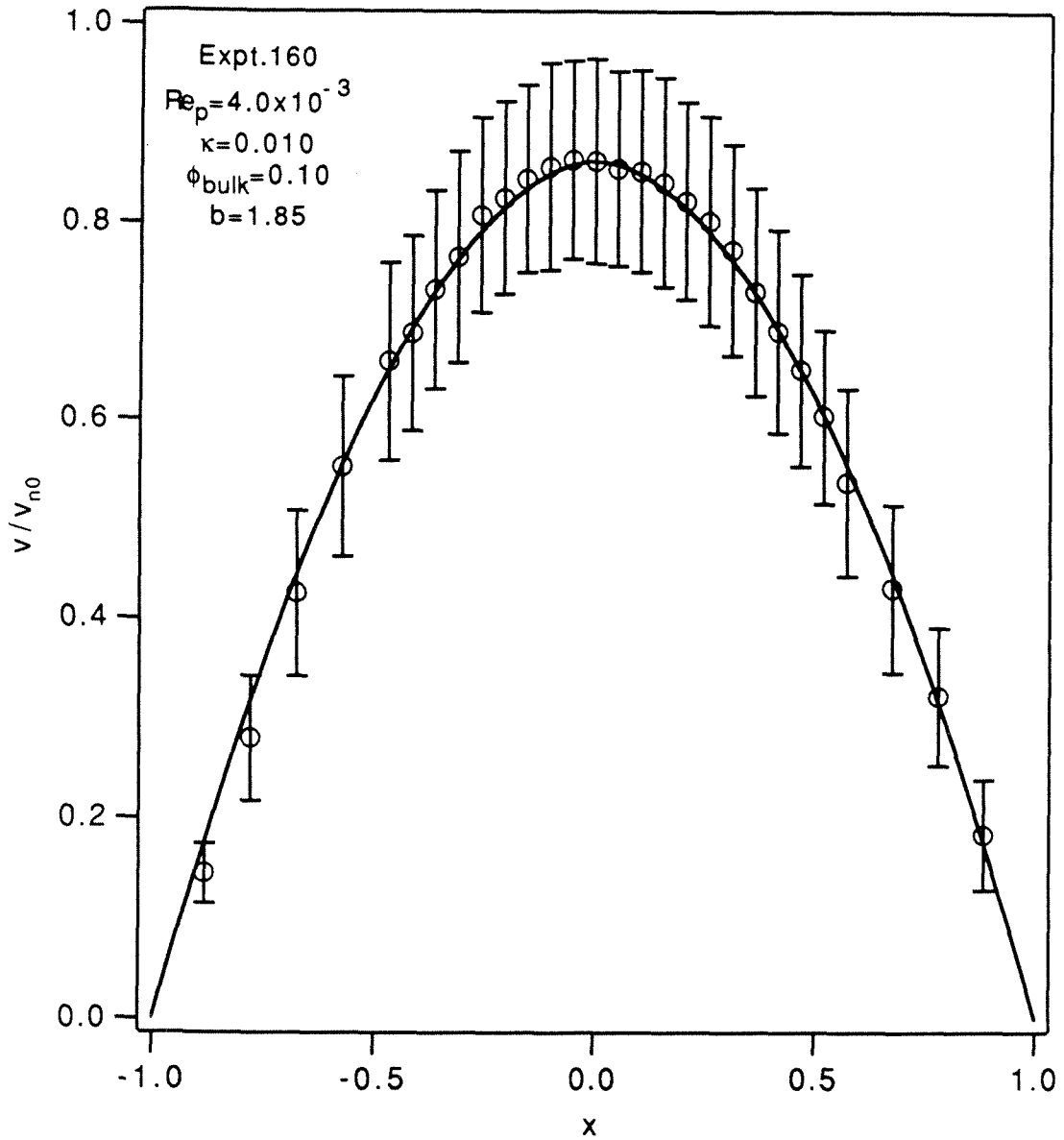


Figure 3.17

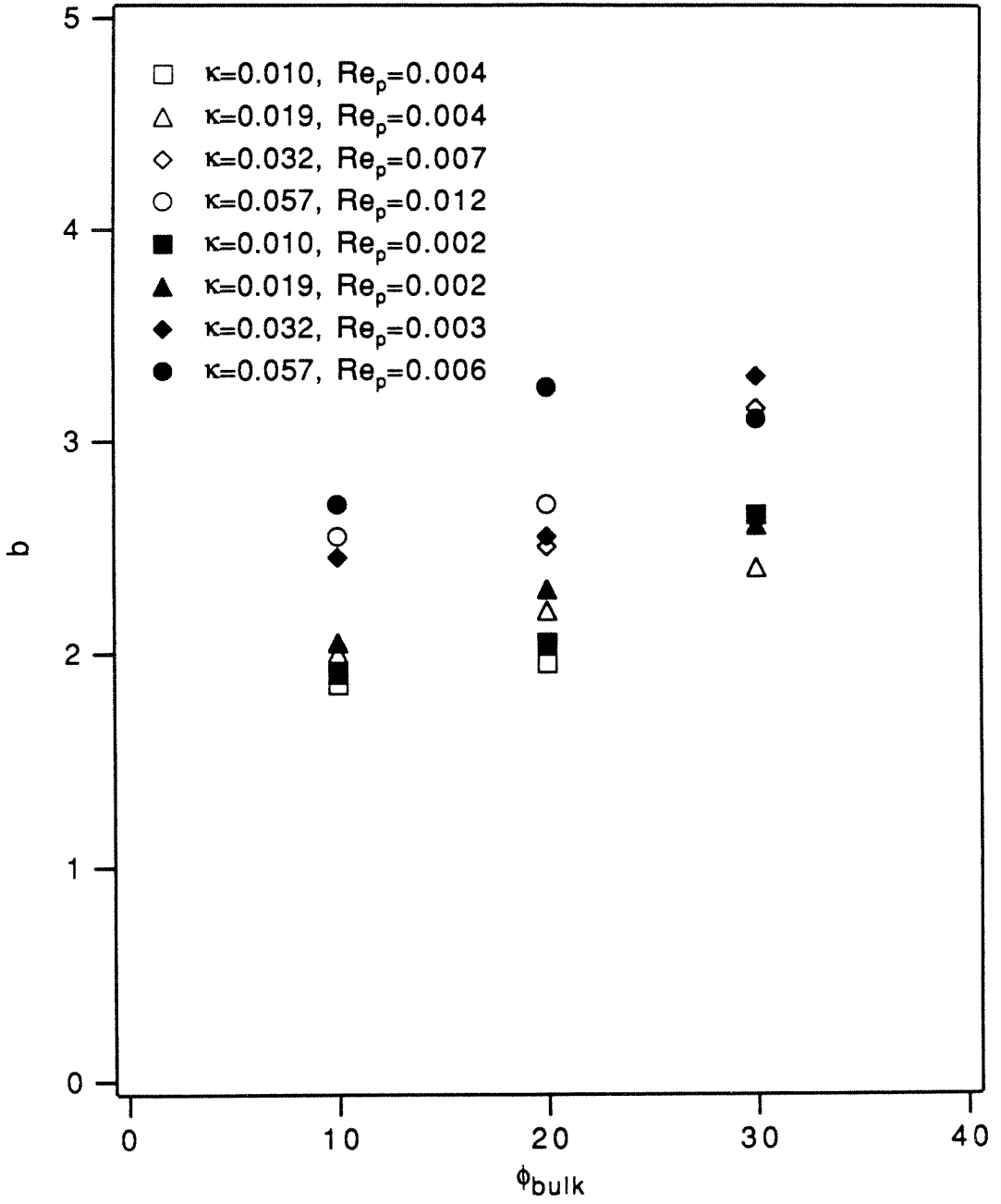


Figure 3.18

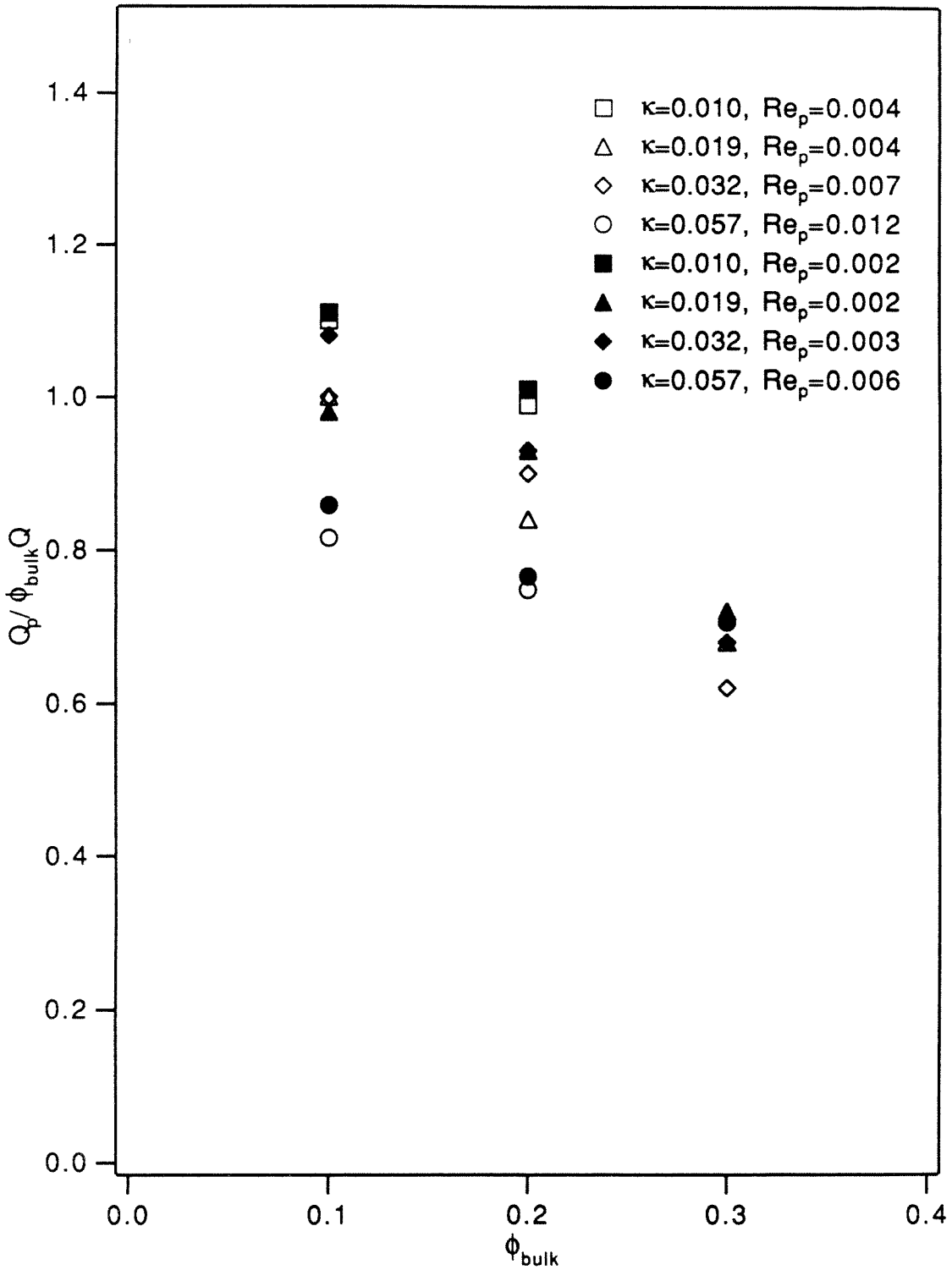


Figure 3.19

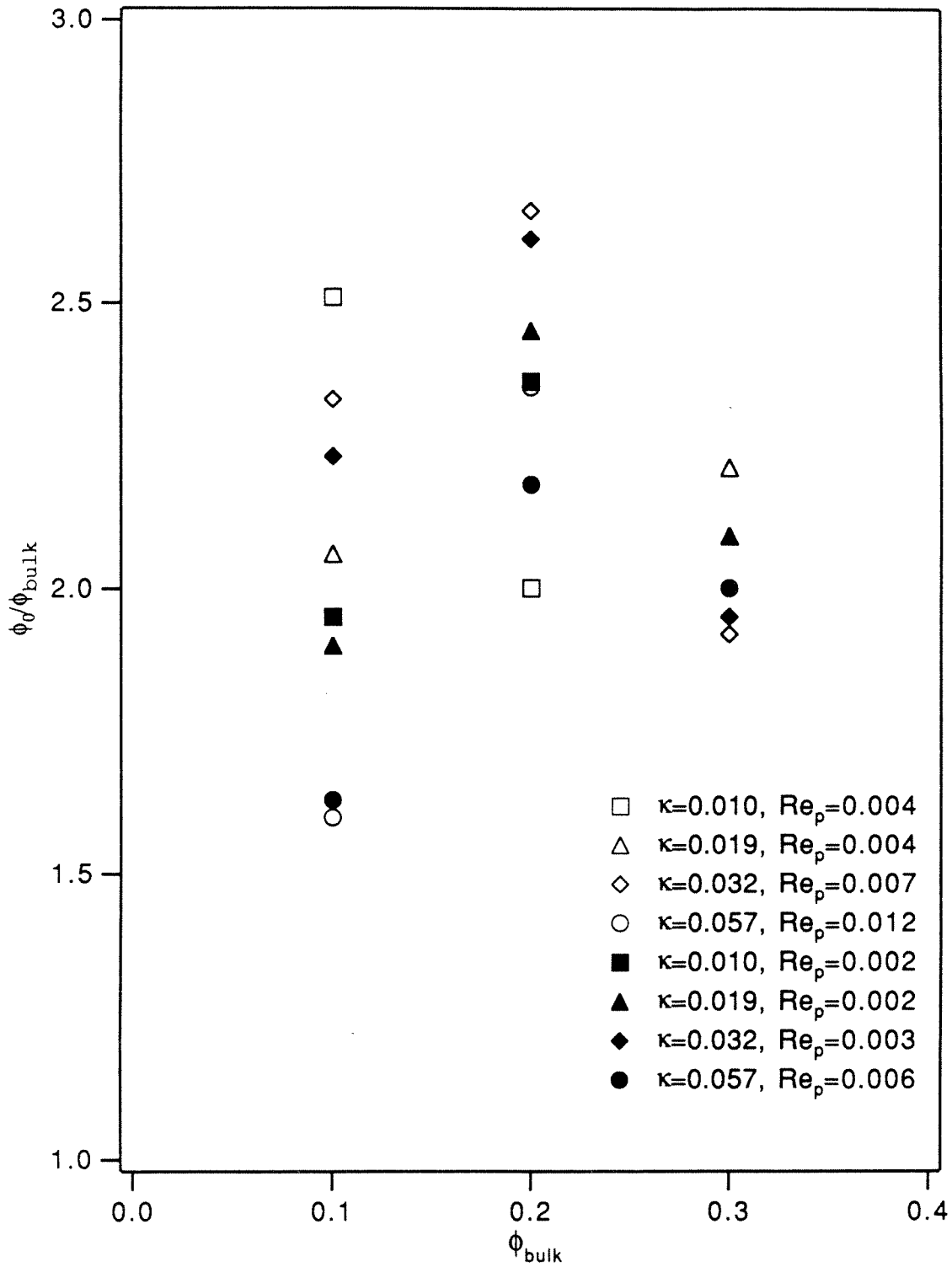


Figure 3.20

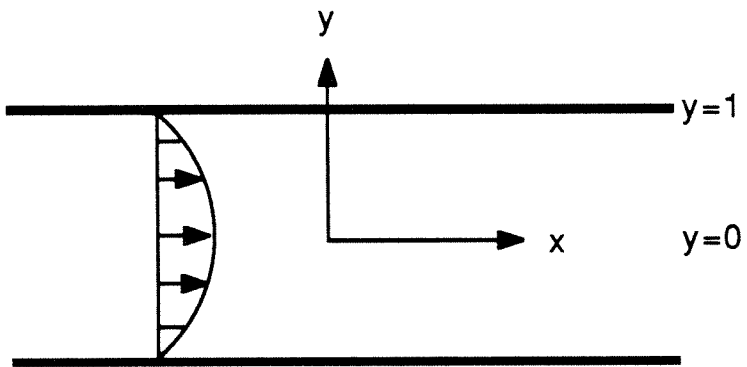


Figure 3.21

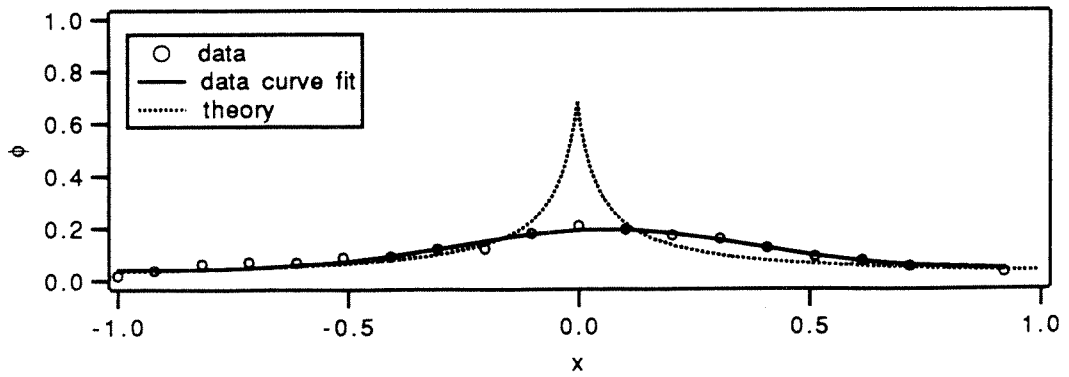
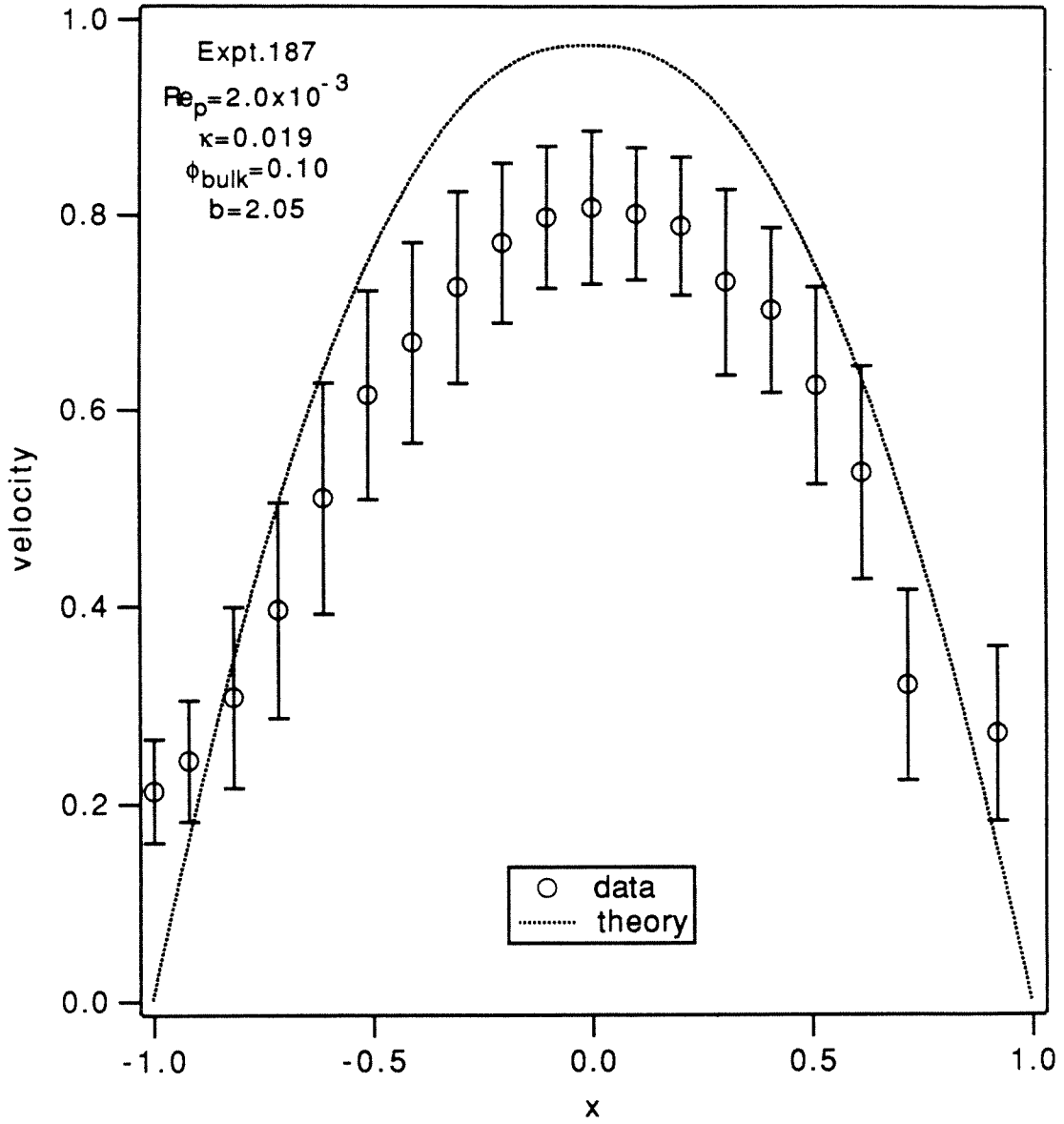


Figure 3.22

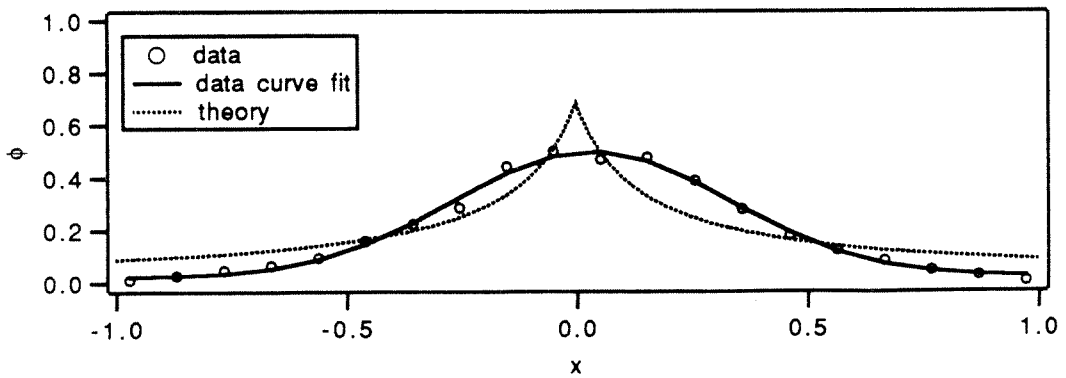
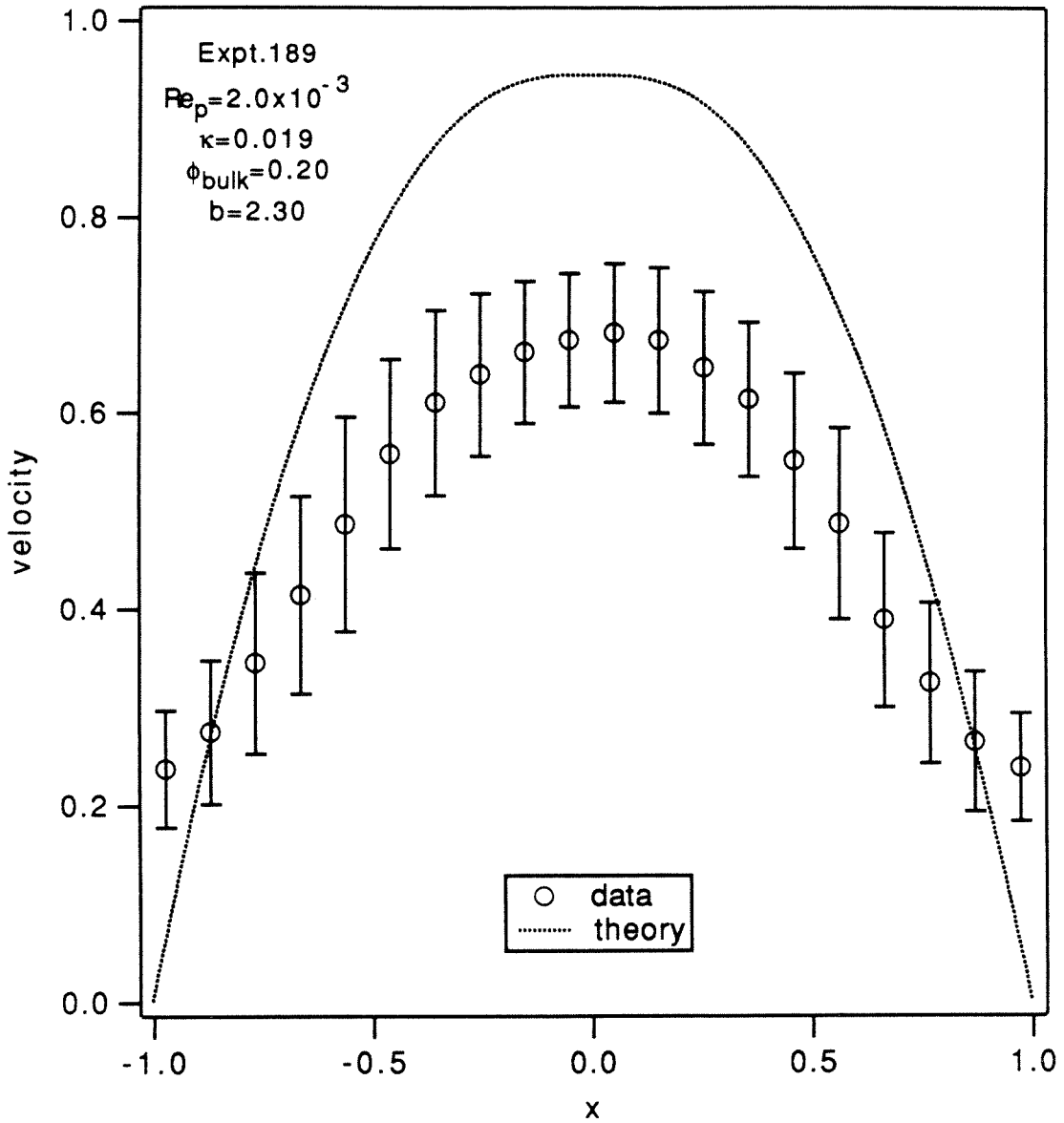


Figure 3.23

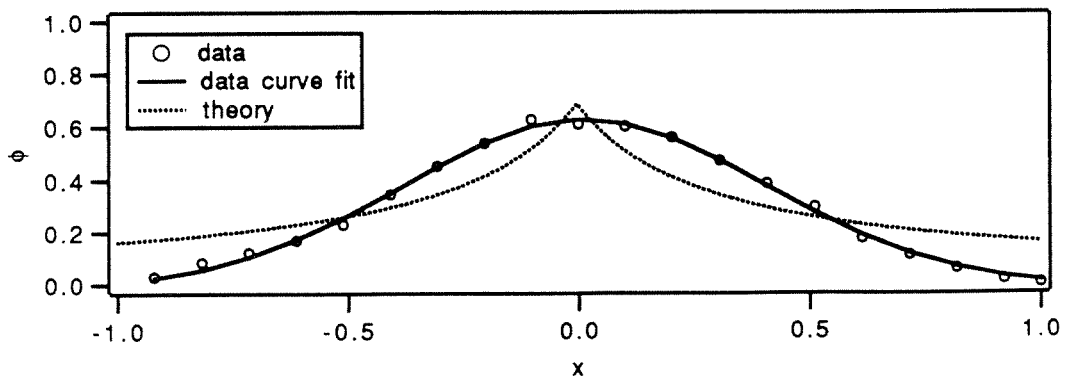
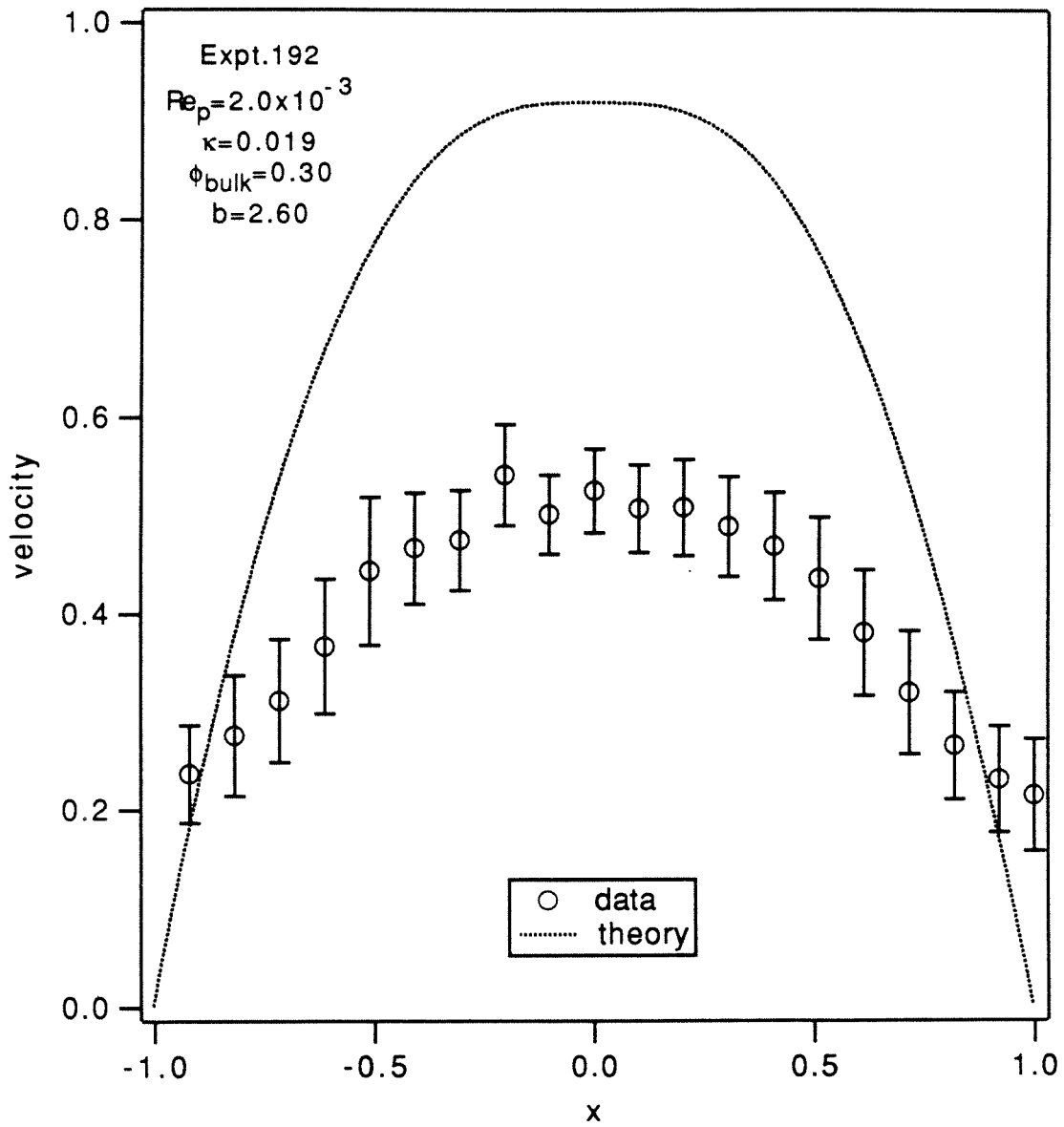


Figure 3.24

	Viscosity(cP)	Density(g/cm ³)
1-Chloronaphthalene		
16.0°C	3.79	—
20.0°C	3.42	1.191
24.0°C	3.13	—
1-Methylnaphthalene		
16.0°C	3.70	—
20.0°C	3.29	1.017
24.0°C	2.97	—
UCON oil 75-H-90,000		
16.0°C	6.89×10^4	—
20.0°C	5.11×10^4	1.094
24.0°C	4.18×10^4	—
Suspending Liquid		
16.0°C	148	—
20.0°C	124	1.052
24.0°C	106	—

Table 1

Experiment No.	κ	Φ	Re_p
160	0.010	0.10	4.0×10^{-3}
158	0.010	0.10	2.0×10^{-3}
215	0.010	0.20	4.0×10^{-3}
217	0.010	0.20	2.0×10^{-3}
172	0.010	0.30	2.0×10^{-3}
186	0.019	0.10	4.0×10^{-3}
187	0.019	0.10	2.0×10^{-3}
191	0.019	0.20	4.0×10^{-3}
189	0.019	0.20	2.0×10^{-3}
194	0.019	0.30	4.0×10^{-3}
192	0.019	0.30	2.0×10^{-3}
199	0.032	0.10	6.6×10^{-3}
198	0.032	0.10	3.3×10^{-3}
204	0.032	0.20	6.6×10^{-3}
202	0.032	0.20	3.3×10^{-3}
207	0.032	0.30	6.6×10^{-3}
205	0.032	0.30	3.3×10^{-3}
246	0.057	0.10	1.2×10^{-2}
245	0.057	0.10	5.9×10^{-3}
224	0.057	0.20	1.2×10^{-2}
223	0.057	0.20	5.9×10^{-3}
226	0.057	0.30	5.9×10^{-3}

Table 2

Appendix A: Laser Doppler Anemometry

The LDA method is based on the principle of Doppler shift—the frequency of light scattered by a *moving* scatterer is shifted by an amount proportional to the velocity of the scatterer. Consider a particle moving at speed v across laser beam 1 at A (see Figure A1). The frequency shift of the *scattered* light is given by

$$\frac{\Delta\nu_1}{\nu} = \frac{v}{c}(\cos\theta_1 + \cos\phi) \quad (\text{A1})$$

where ν is the frequency of the laser beam and c is the speed of light *in vacuo*. It is clear that the maximum shift is of the order of (v/c) ; for most fluid flows, especially those we encounter in chemical engineering processes, this ratio is of the order of 10^{-8} . From a technical point of view, this relatively small frequency shift is extremely difficult to measure directly. However, consider an optical system consisting of two laser beams (beams 1 and 2). Similarly, the frequency shift of the scattered light due to the same particle passing through beam 2 is

$$\frac{\Delta\nu_2}{\nu} = \frac{v}{c}(\cos\theta_2 + \cos\phi) \quad (\text{A2})$$

When the particle passes through the region of intersection of beams 1 and 2, scattered light due to both beams can be mixed and the resulting mixture consists of signals equal to the the harmonics, the sum as well the difference of ν_1 and ν_2 (where $\nu_1 = \nu + \Delta\nu_1$ and $\nu_2 = \nu + \Delta\nu_2$). Ignoring signals with frequencies too high to be detected, we can define the beat frequency as

$$\begin{aligned} f_{\text{Doppler}} &= \nu_1 - \nu_2 \\ &= \frac{2v}{\lambda} \sin\left(\frac{\alpha}{2}\right) \cos\beta \end{aligned} \quad (\text{A3})$$

This beat frequency, denoted by f_{Doppler} , is directly proportional to the component of the velocity in the z -direction of the particle and is usually in a frequency range that can be readily detected by various types of detector (such as a photomultiplier tube used in this experiment).

The optical system discussed above is known as the real-fringe mode LDA. It is customary to explain its operational principle by the following physical interpretation (see Figure A2). The photomultiplier tube is a nonlinear device in the sense that its current output is proportional to the *square* of the electric field. Consequently, the quantity of interest is the light intensity distribution due to the two laser beams. It is given by

$$\begin{aligned} I &= (E_1 + E_2)^2 \\ &= I_o \left\{ \exp \left(-\frac{z^2 \cos^2 \alpha + x^2 \sin^2 \alpha + y^2}{r_o^2} \right) \times \right. \\ &\quad \left. \left[\cosh \left(\frac{xz \sin 2\alpha}{r_o^2} \right) + \cos \left(\frac{4\pi z \sin \alpha}{\lambda} \right) \right] \right\} \end{aligned} \quad (A4)$$

where

$$\begin{aligned} I_o/2 &= \text{intensity of each of the laser beam} \\ \alpha &= \text{half-angle of the beam crossing} \\ \lambda &= \text{wavelength of laser light} \end{aligned}$$

and

$$r_o = \text{beam radius of incident laser beam} \quad (A5)$$

The cosine term in the square brackets is due to constructive and destructive interference of the two laser beams. This interference produces alternate light and dark “fringes” at a fringe spacing equal to

$$d_f = \frac{\lambda}{2 \sin(\frac{\alpha}{2})} \quad (A6)$$

Consequently, as a particle passes through this region of fringes at a velocity v , it scatters light that is modulated at a frequency determined by the component of the velocity normal to the orientation of the fringes

$$\begin{aligned} f_{\text{Doppler}} &= \frac{v}{d_f} \\ &= \frac{2v}{\lambda} \sin\left(\frac{\alpha}{2}\right) \cos\beta \end{aligned} \quad (A7)$$

It is clear that the result derived from this physical interpretation is the same as that given by Equation A3 .

Additional information can be extracted from Equation A4. The *cosh* term, compared to the cosine term, varies slowly in space. In fact, this relatively constant term produces a low frequency signal as a particle passes through the laser beams. Since this signal does not contain any velocity information, it is usually eliminated electronically with a high pass filter, as shown in Figure A3. The exponential term, due to the Gaussian intensity distribution of the laser beams, governs the size of the measurement volume. The light intensity, with its maximum at the origin, decays to $1/e^2$ of maximum intensity (I_0) on the ellipsoid (Figure A2)

$$z^2 \cos^2 \alpha + x^2 \sin^2 \alpha + y^2 = 2r_o^2 \quad (\text{A8})$$

The effective size of the measurement volume can be defined as the boundary of this ellipsoid:

$$\Delta x_{eff} = 2\sqrt{2}r_o/\sin\alpha \quad (\text{A9})$$

$$\Delta y_{eff} = 2\sqrt{2}r_o \quad (\text{A10})$$

$$\Delta z_{eff} = 2\sqrt{2}r_o/\cos\alpha \quad (\text{A11})$$

Figure Captions

1. Frequency shift for laser Doppler anemometry.
2. Fringe pattern at the intersection of the laser beams.
3. LDA signal before and after high pass filter.

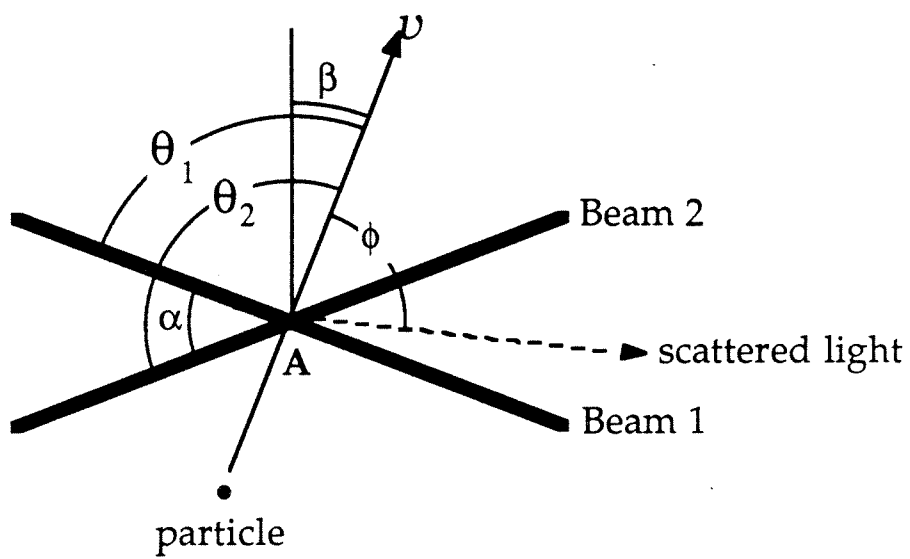


Figure A1

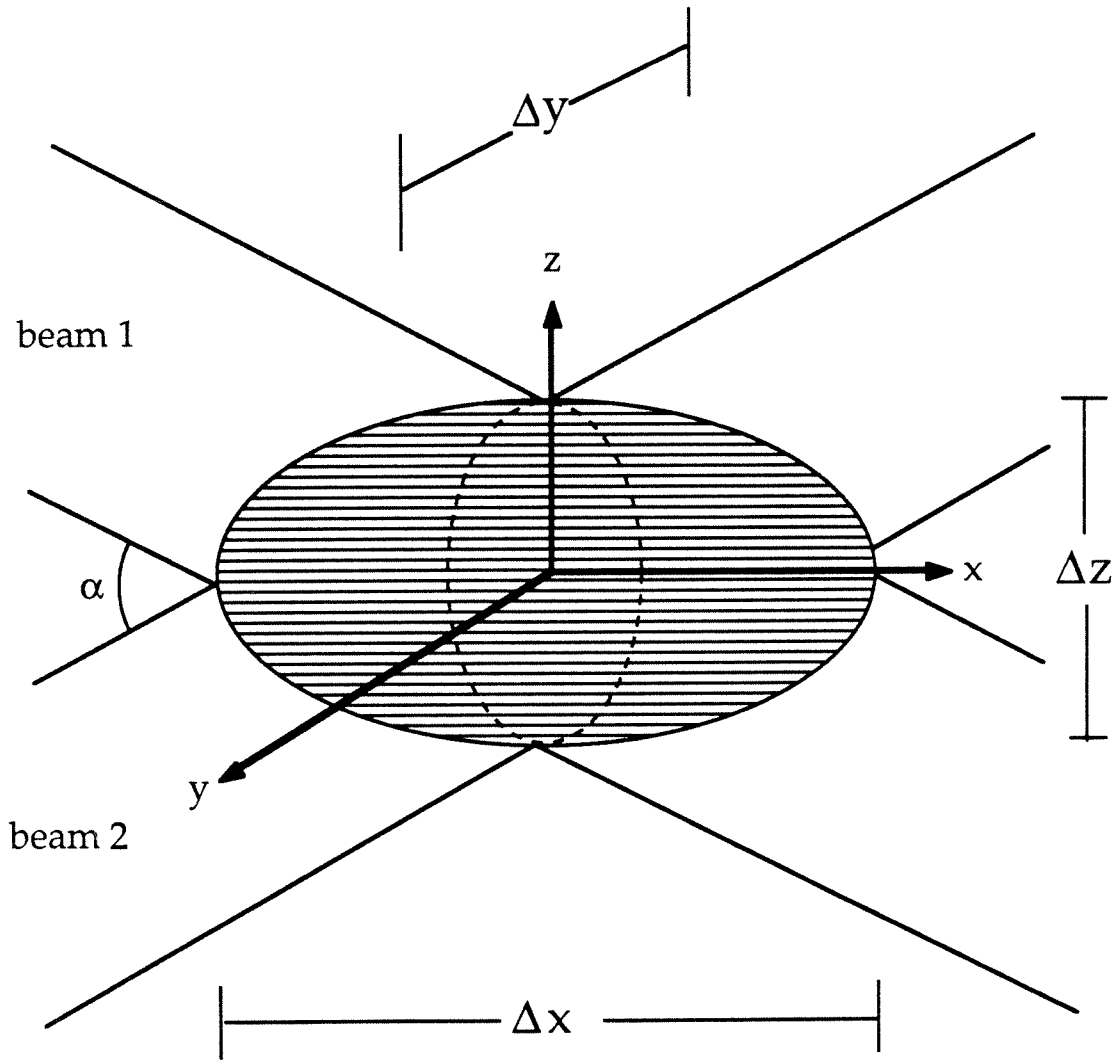


Figure A2

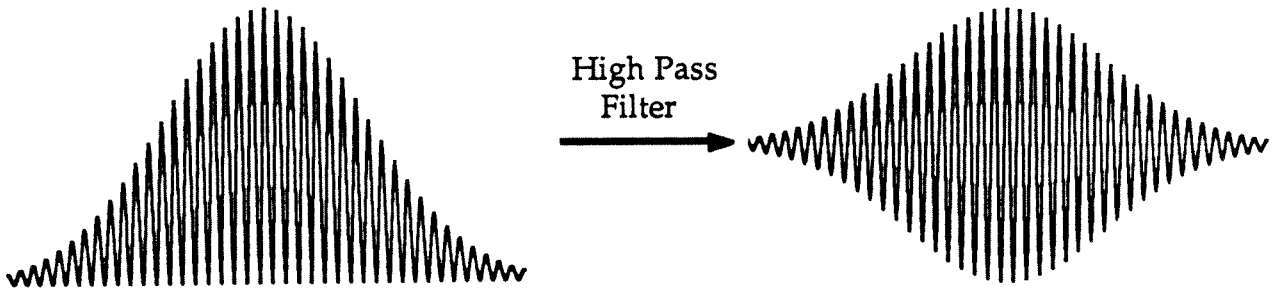
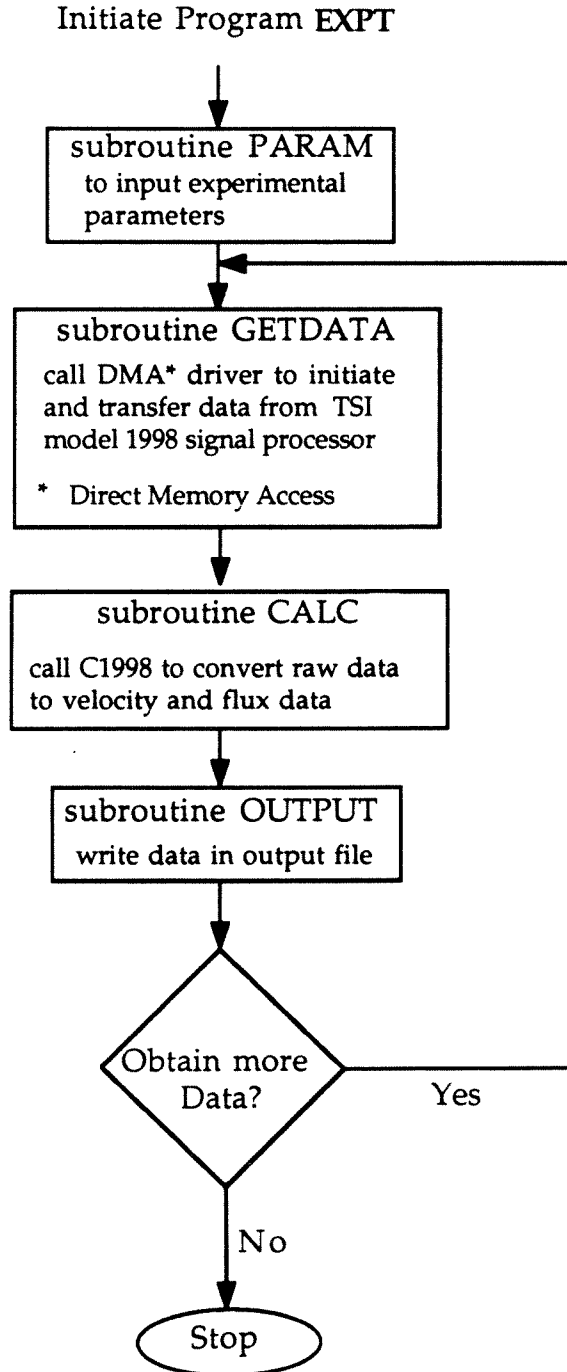


Figure A3

Appendix B

Flowchart of FORTRAN program **EXPT** that collects and interprets data from the LDA experiment:



Appendix C

In this appendix, we discuss some of the details relevant to the operation of the LDA experiment. It will be presented as a set of step-by-step instructions to aid those who wish to perform the experiment.

- Preparation of the suspending fluid. As mentioned in Chapter 3, the refractive indices and the densities of the suspending fluid and the particles are matched.
 1. The 3-component suspending fluid consists of 1-methylnaphthalene, 1-chloronaphthalene, and UCON-oil 75-H-90,000.
 2. An initial “guess” of the composition of the suspending fluid is obtained by assuming linear relationships of the density and refractive index between the components and the resulting fluid. After mixing the fluids, the refractive index and the density are measured. Small adjustments in the composition are then made to ensure the required density and refractive index are obtained.
 3. The suspending fluid is then filterized through $0.22\mu\text{m}$ filter to remove any impurities and dust particles.
- Preparation of the flow channel. As in any other optical experiments, it is important that the optical surfaces be clean and free of defects (such as scratches).
 1. Two pieces of optical quality glass with multiline anti-refractive coatings are used for the flow channel.
 2. After a set of experiments, the flow channel is taken apart and cleaned thoroughly. This is facilitated by the use of a sonic bath filled with cleaning solution (Micro Cleaning Solution).
 3. The flow channel is then rinsed with filtered and deionized water and allowed to air-dry.

4. The two pieces of glass are cleaned once more by wiping with spectroscopic grade methanol and acetone.

- Preparation of the flow pump.

1. Teflon-coated tubings are utilized to connect the syringe pump to the flow channel. These tubings are cleaned by the use of the sonic bath.

2. Small amount of the suspending fluid is used to lubricate the glass syringes of the pump.

- Preparation of the suspension.

1. Approximately 125 ml of suspension is required for the capacity of the flow system.

2. The necessary amount of particles and suspending fluid are mixed together and stirred carefully to minimize the formation of bubbles in the suspension. The suspension is then allowed to stand for about 15-45 minutes for the bubbles to rise to the top.

3. The suspension is carefully poured into the reservoir of the flow cell.

4. The pump is turned on and the suspension is circulated through the flow system.

- Operation of the laser and electronics.

1. The laser is a Spectra-Physics model 165 argon ion laser. It operates at a wavelength of 488 nm; the power is 0.05 W. Before each experiment, the laser is turned on and allowed to warm up for approximately 30 minutes.

2. The photodetector is a Hamamatsu model 1617 photomultiplier tube. The power supply is a DISA model L55 PM exciter which operates at 0.85 kV.

3. The signal processor is a TSI Model 1980B Counter-Type Signal Processor operating under the TBM mode. The built-in amplifier is set at maximum gain (+34 dB) and the minimum cycle per burst is 4. The low and high cut filters are set at 1 kHz and 100 kHz respectively. It is connected to a Tektronix Type 503 oscilloscope for viewing of the Doppler signals.
4. Digital data is sent to a IBM AT computer. This data is processed and analyzed using the FORTRAN program **EXPT**. A flowchart of this program can be found in Appendix B.

Appendix D

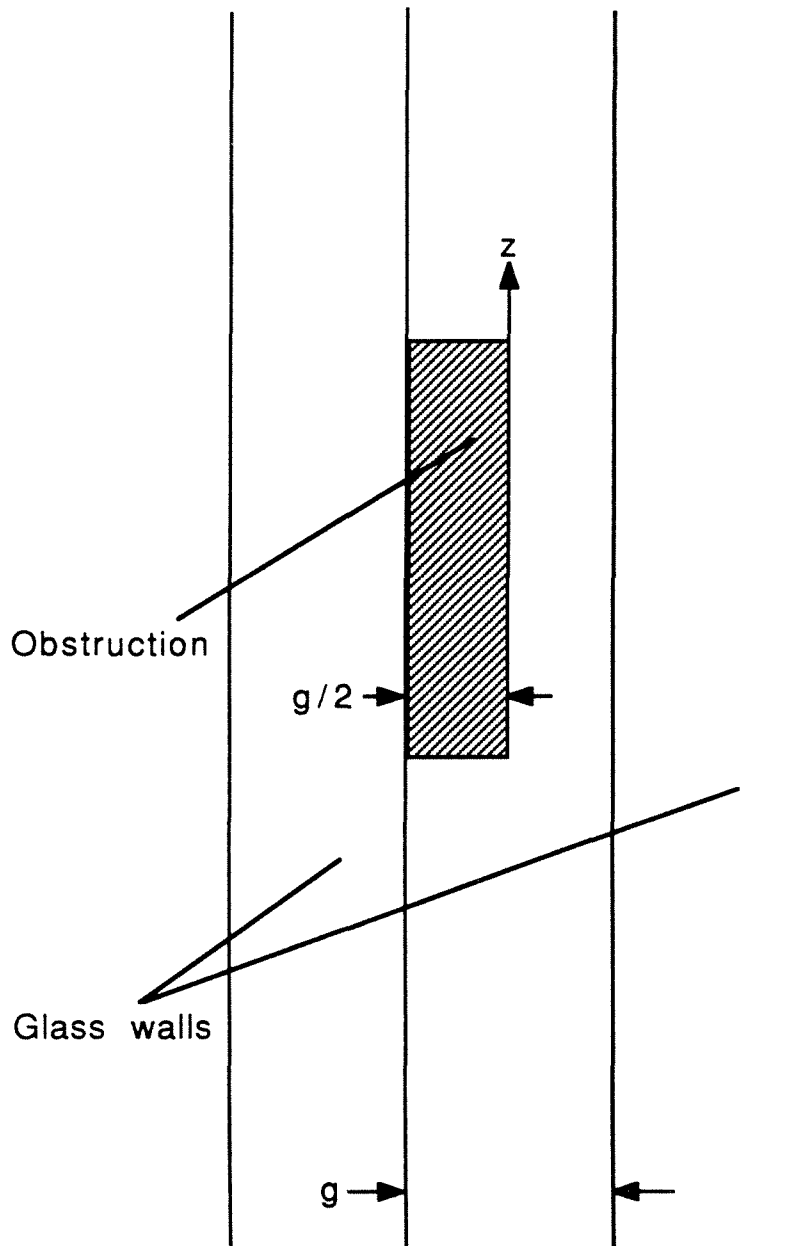
The experimental data given in Chapter 3 are steady state profiles. It is interesting to investigate the behavior of the suspension before it reaches its steady configuration. In this appendix, we show some preliminary data of the evolution of velocity and concentration profiles downstream of an obstruction. The flow channel geometry is shown in Figure D1. The obstruction is a piece of Lucite machined to half the gap width and 2.54 cm long. The z -coordinate is non-dimensionalized with the gap width of the flow channel.

From Figure D2, we can see that the velocity profile quickly returns to a symmetric shape downstream from the flow obstruction. Similarly, the concentration profile becomes symmetric in a distance less than one gap width. The particles can redistribute from an unsymmetric shape to the symmetric shape in such a short distance not because of the shear-induced particle migration effect mentioned in Chapter 3, but most likely because the particles convect along in the same direction of the fluid. Due to the presence of the obstruction, there is a component of the velocity in the gap-wise direction that causes the particle to move from the opening of the obstruction towards the center of the channel.

It should be pointed out that with an obstruction made of Lucite, it is not possible to obtain data closer to the obstruction because the opaque Lucite material blocks the laser beams when the measurement volume is moved too close to the obstruction. This shortcoming can conceivably be minimized by using an obstruction made of optical quality glass (and glued to the glass wall of the flow channel with optical cement).

Figure Captions

1. Flow channel geometry.
2. Velocity and concentration data downstream from obstruction.



Not to scale

Figure D1

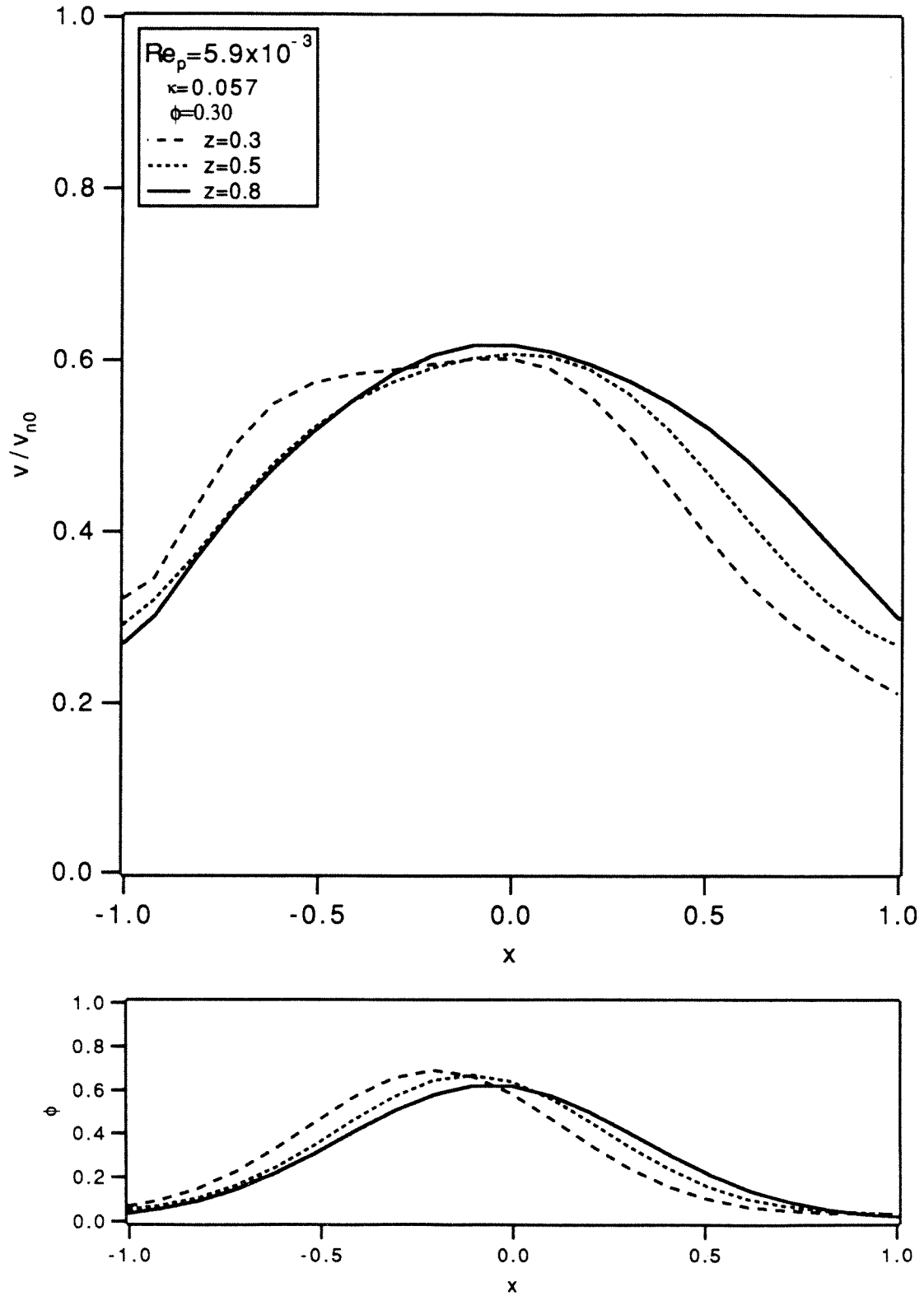
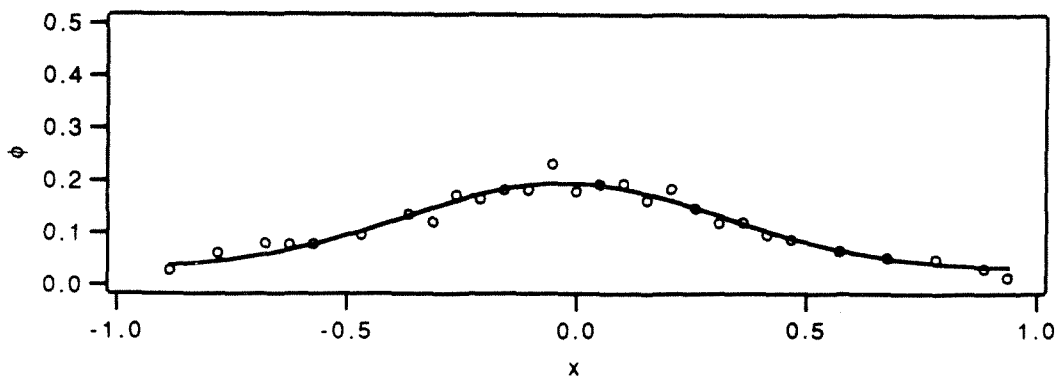
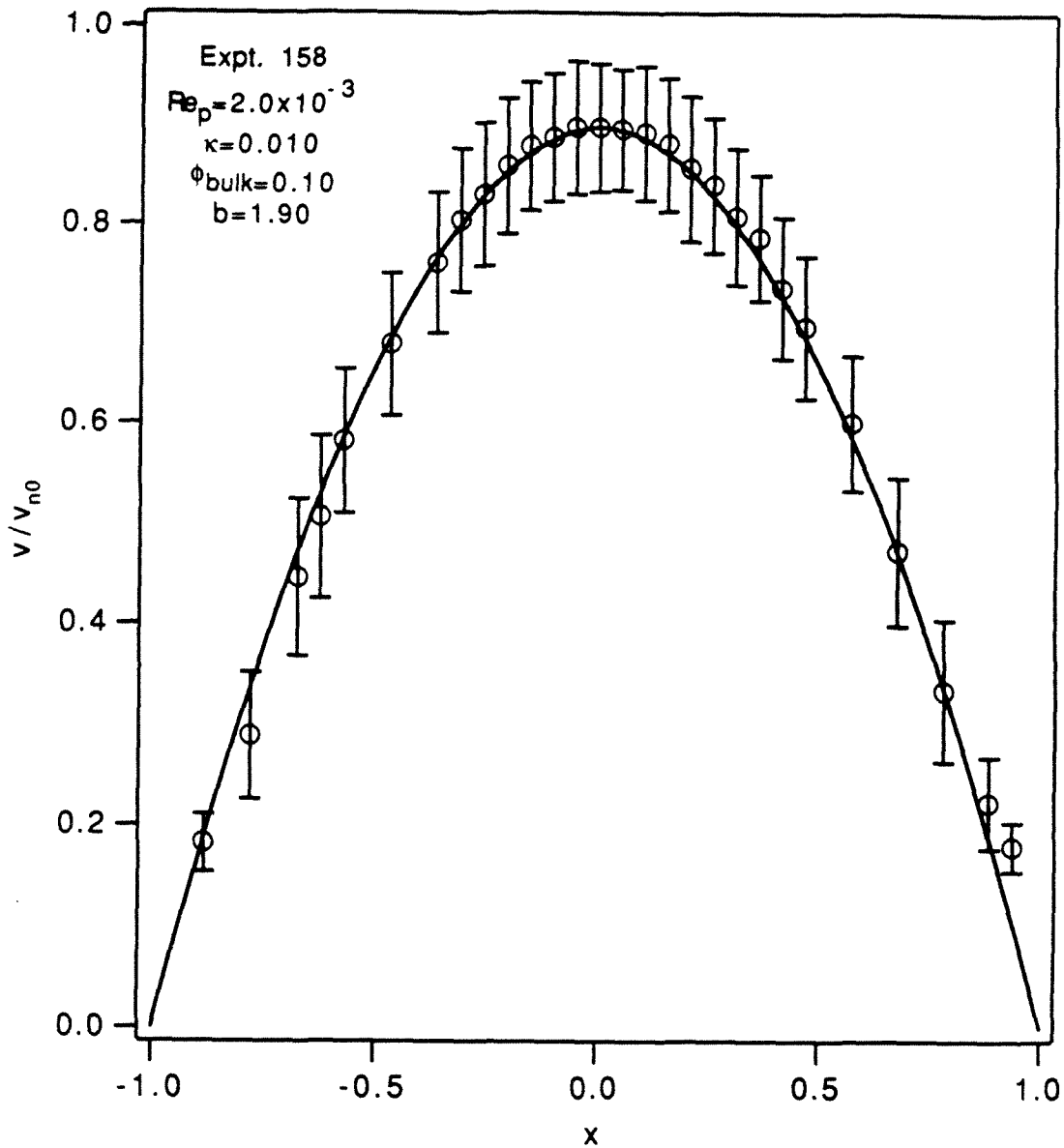
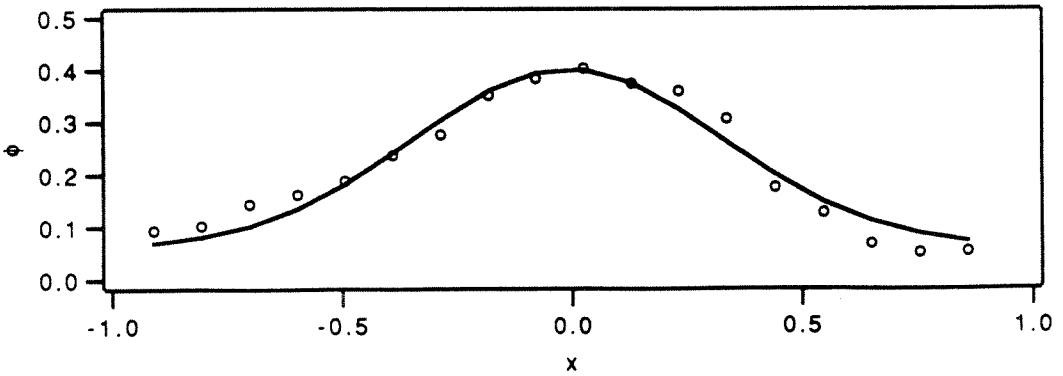
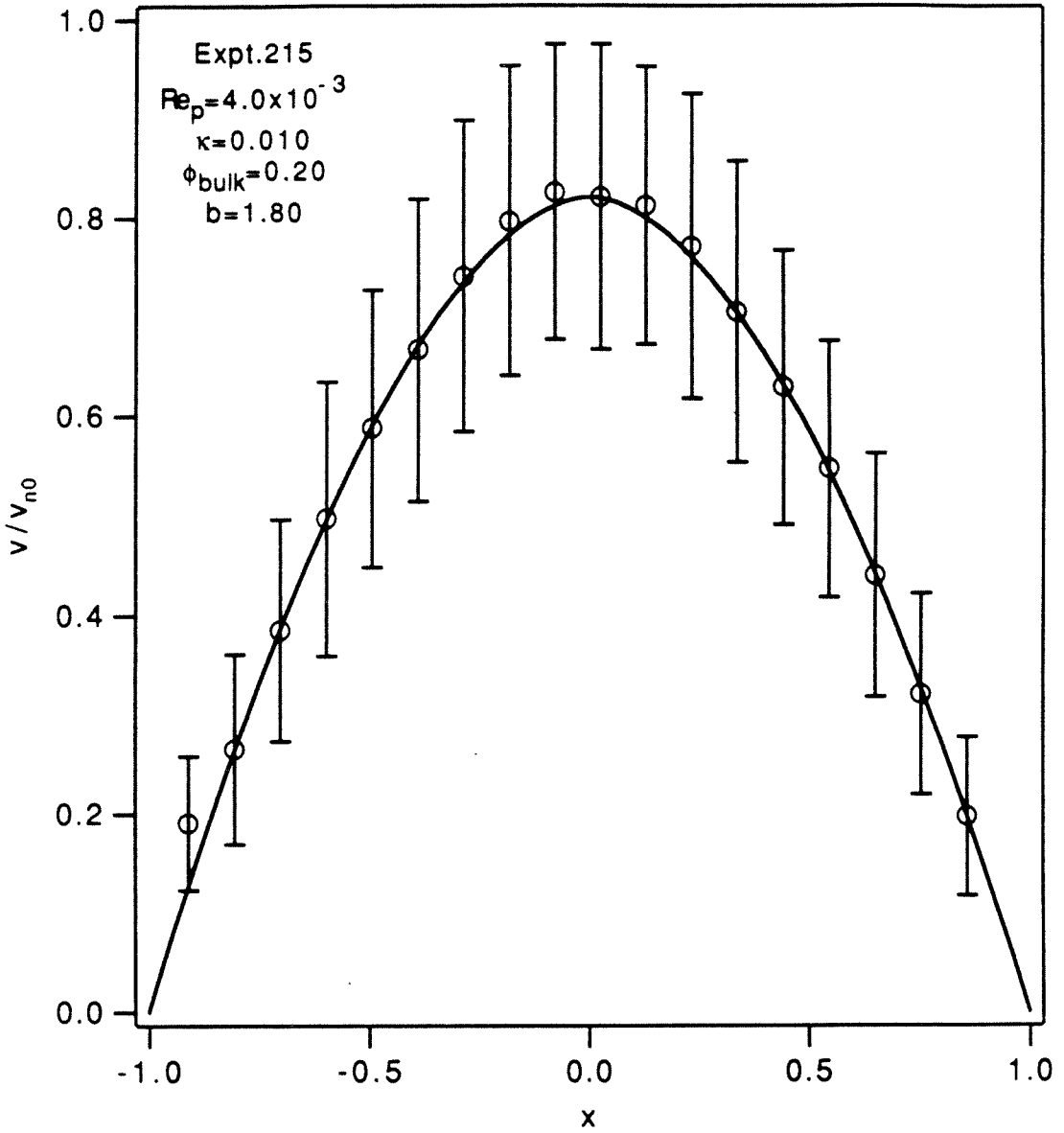


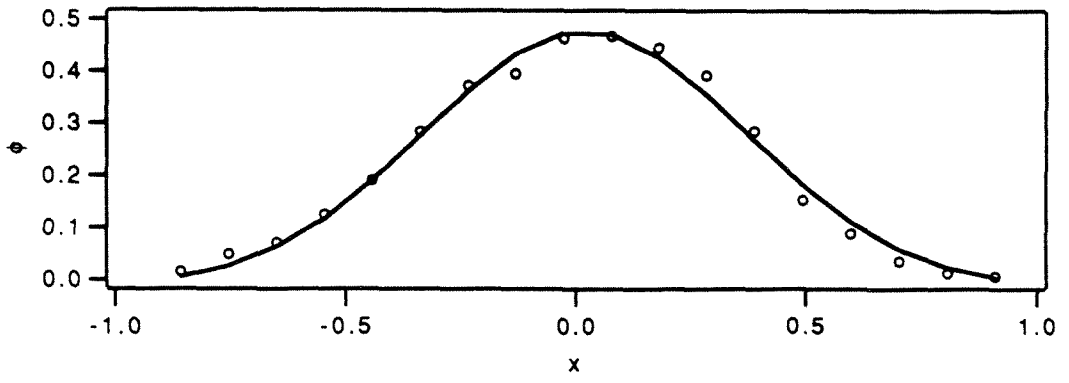
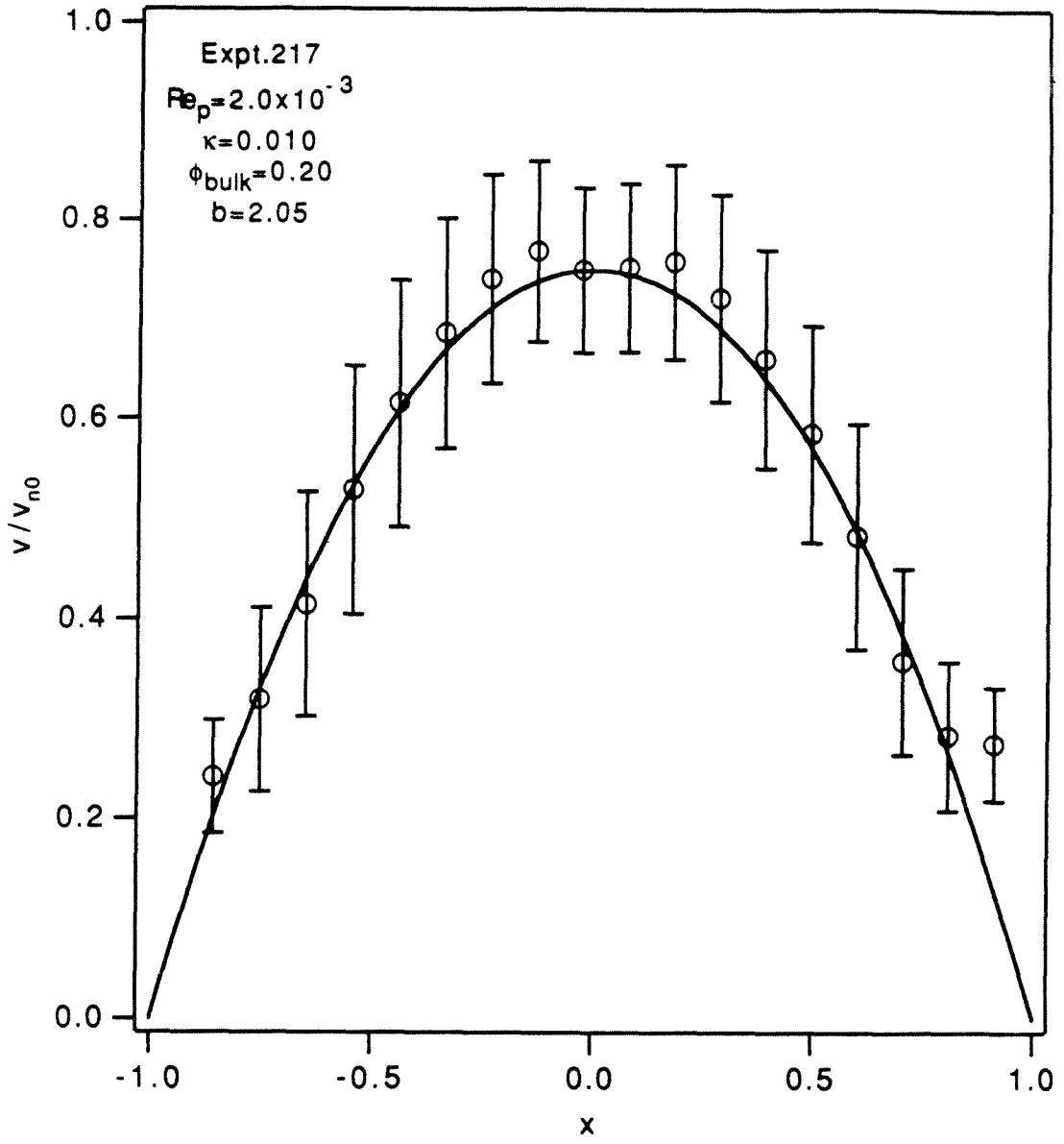
Figure D2

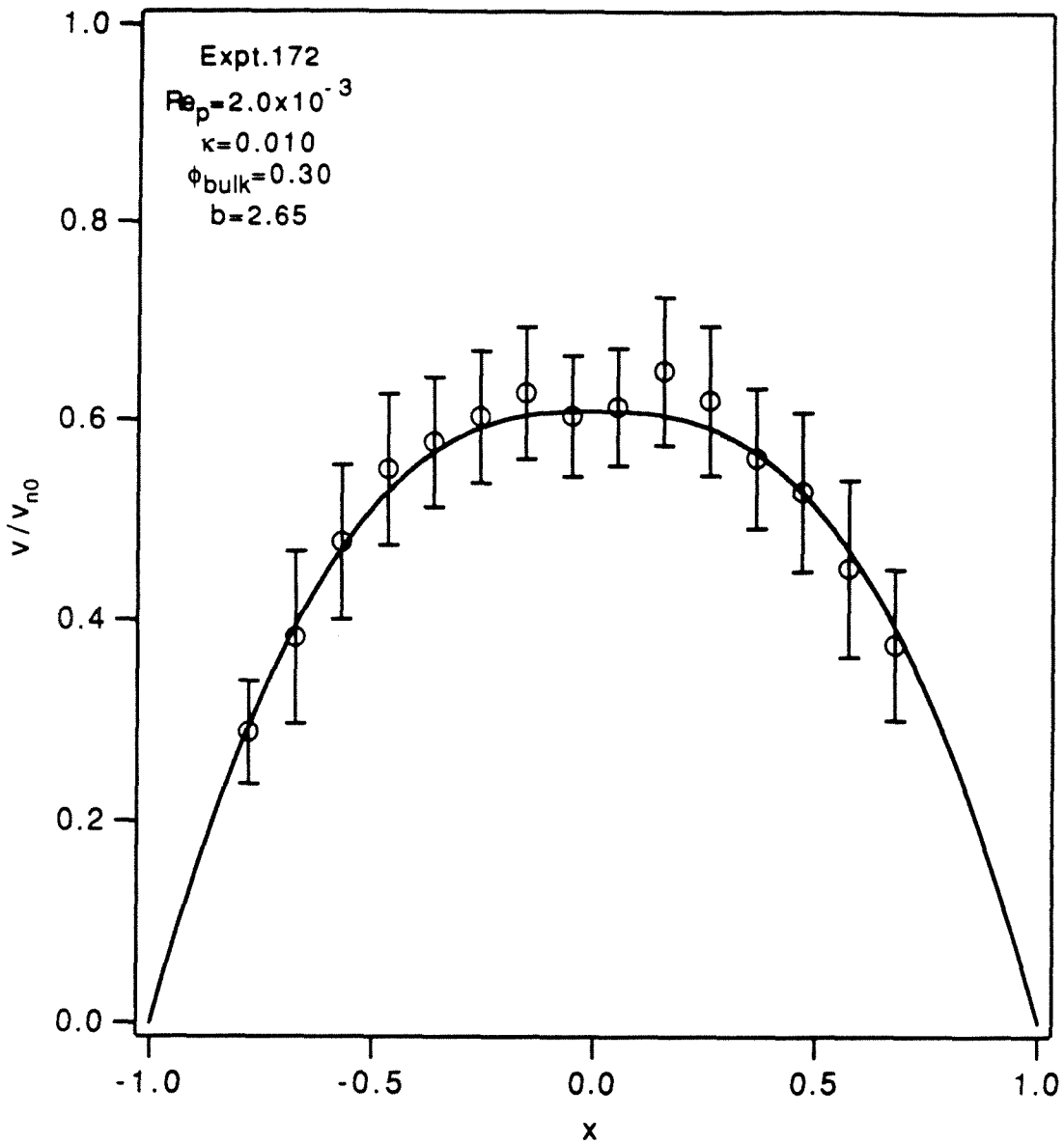
Appendix E

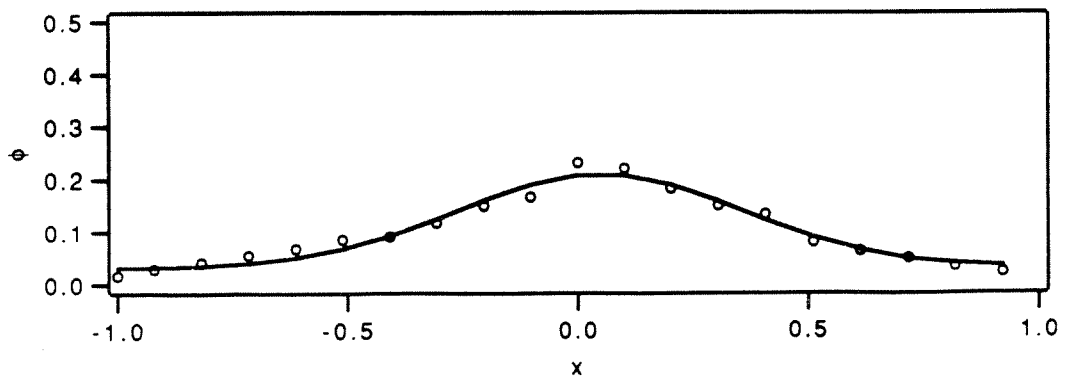
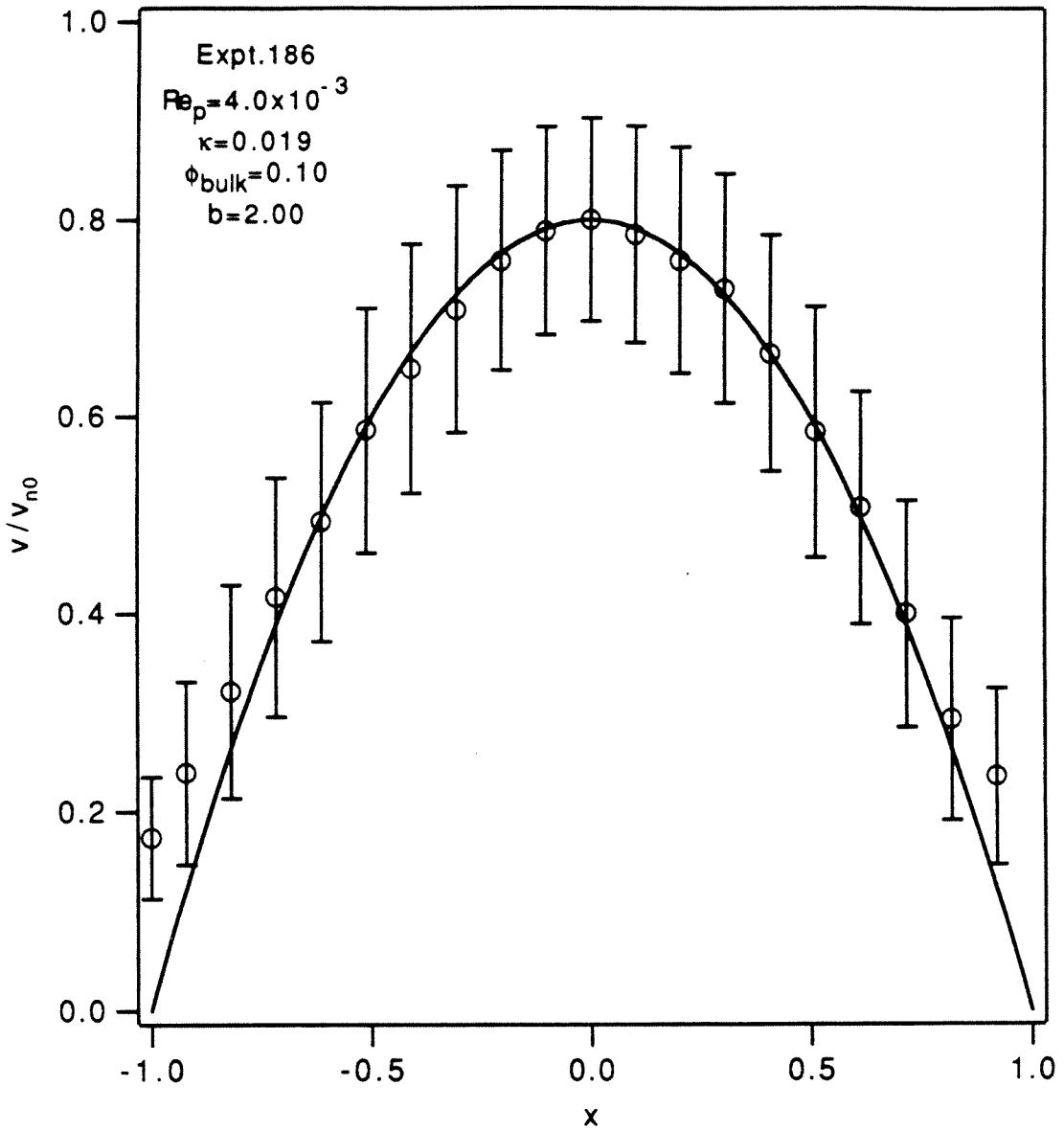
Experimental particle velocity and volume fraction data.

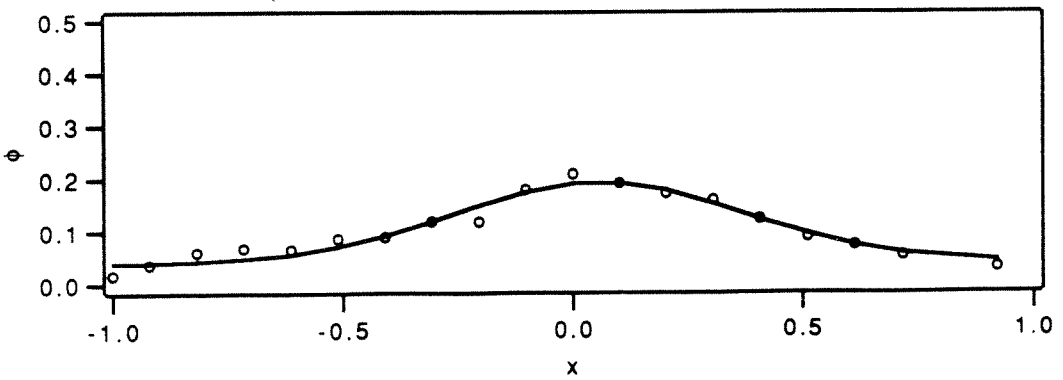
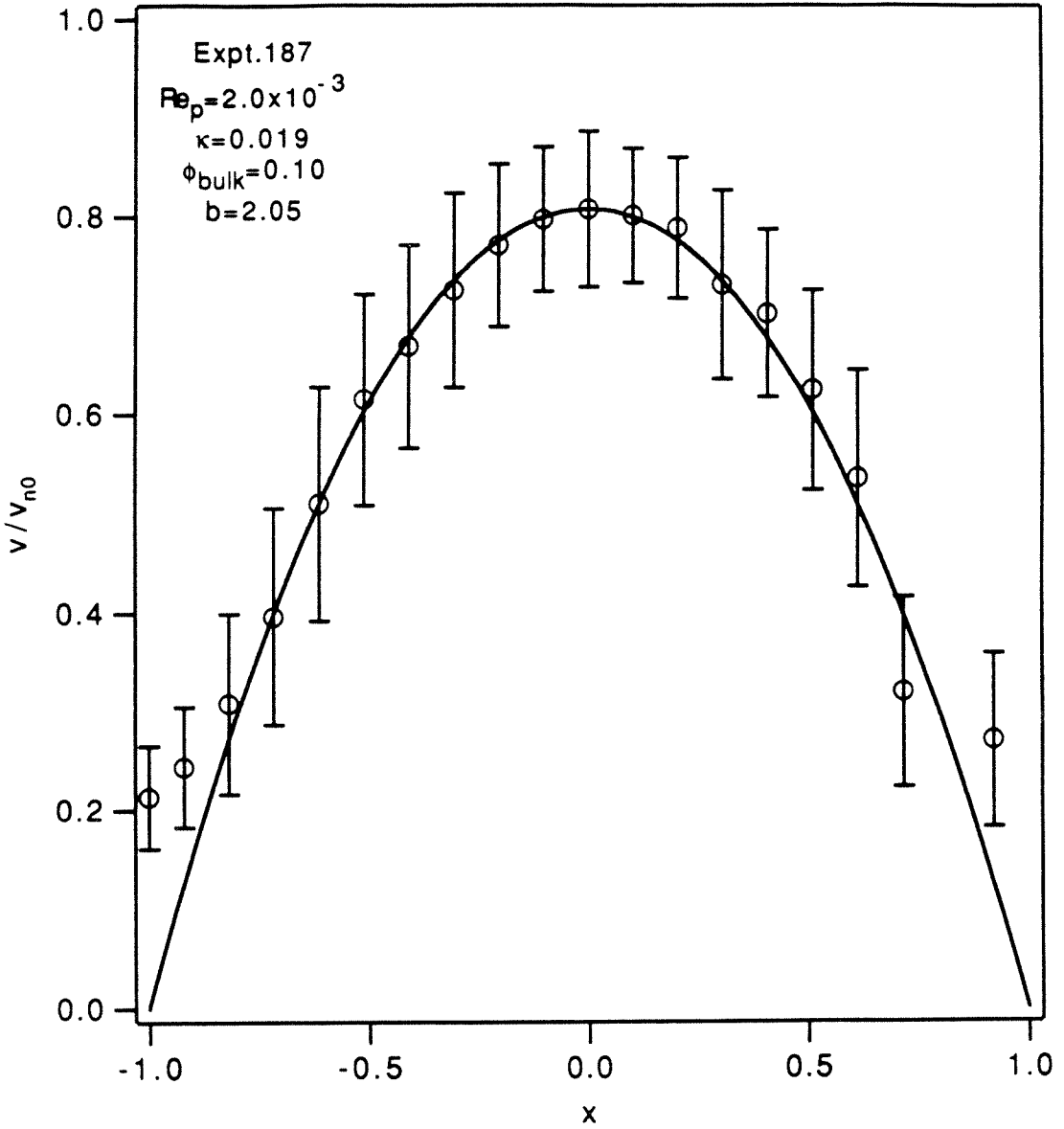


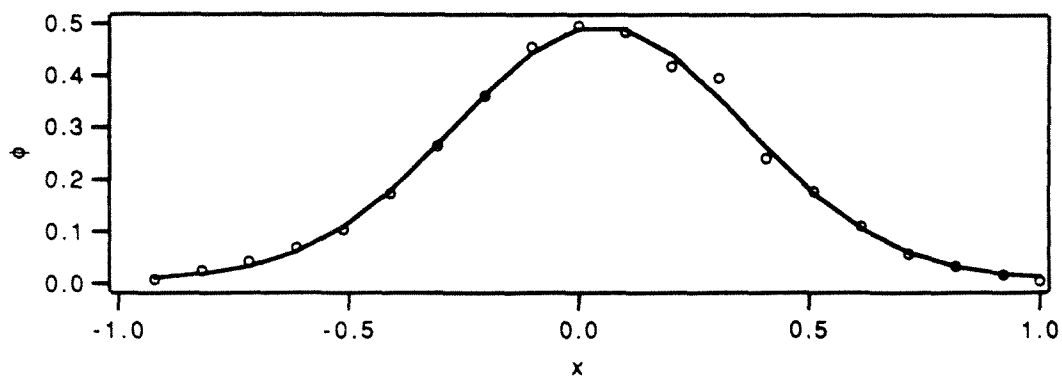
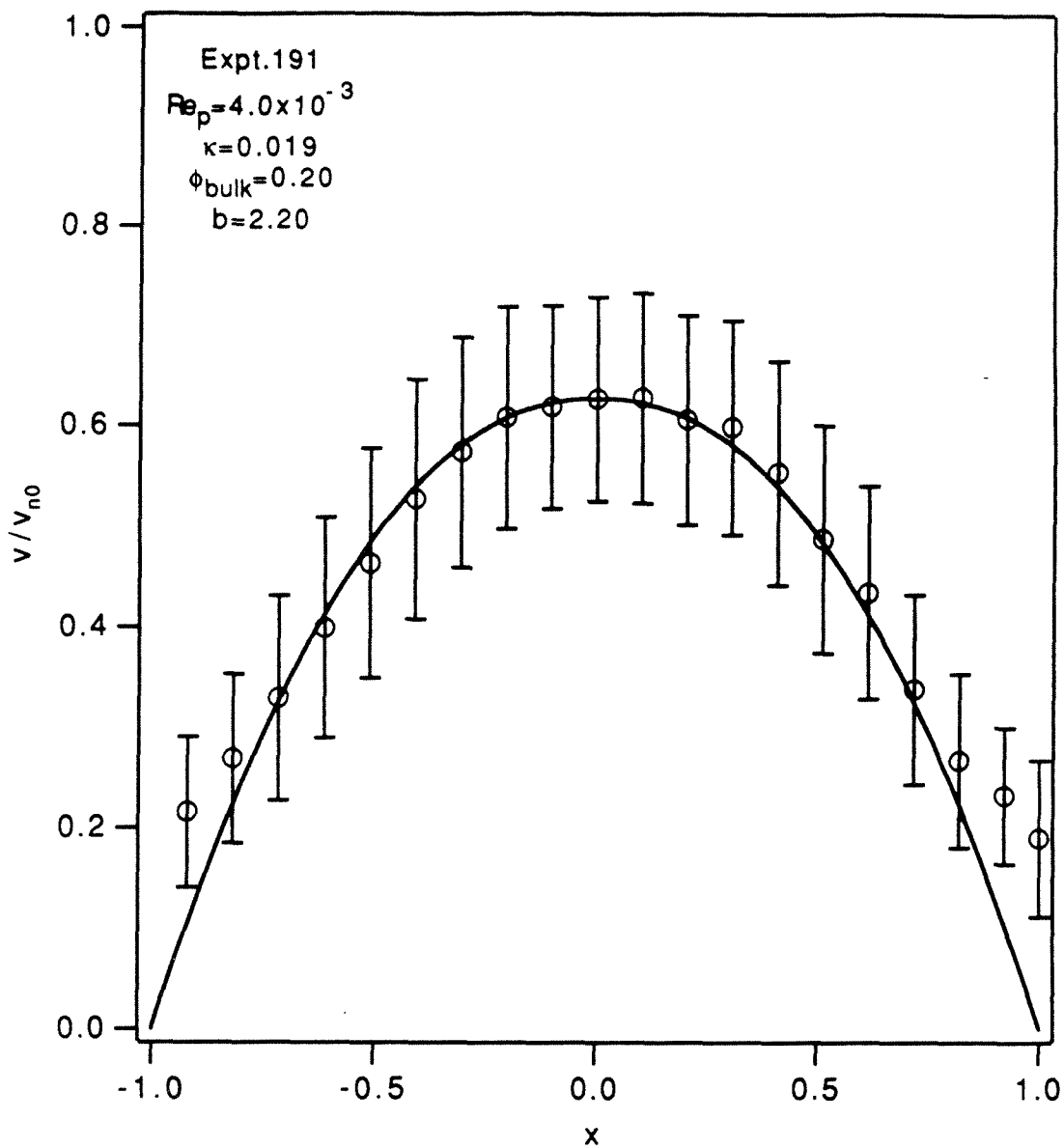


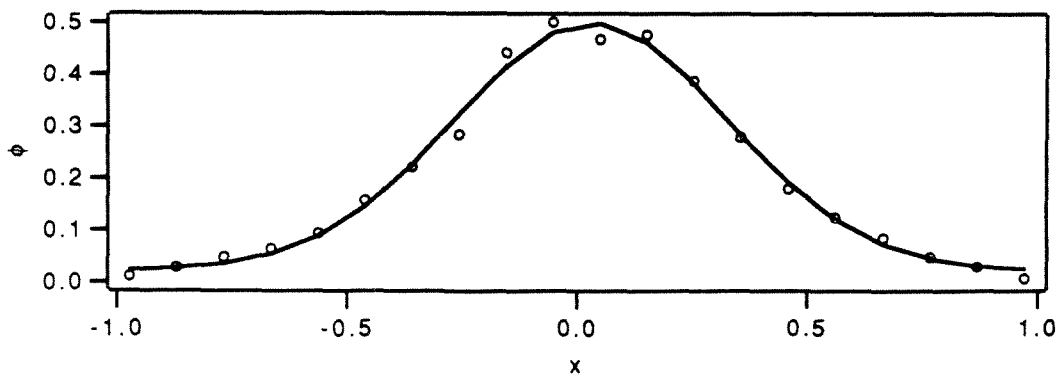
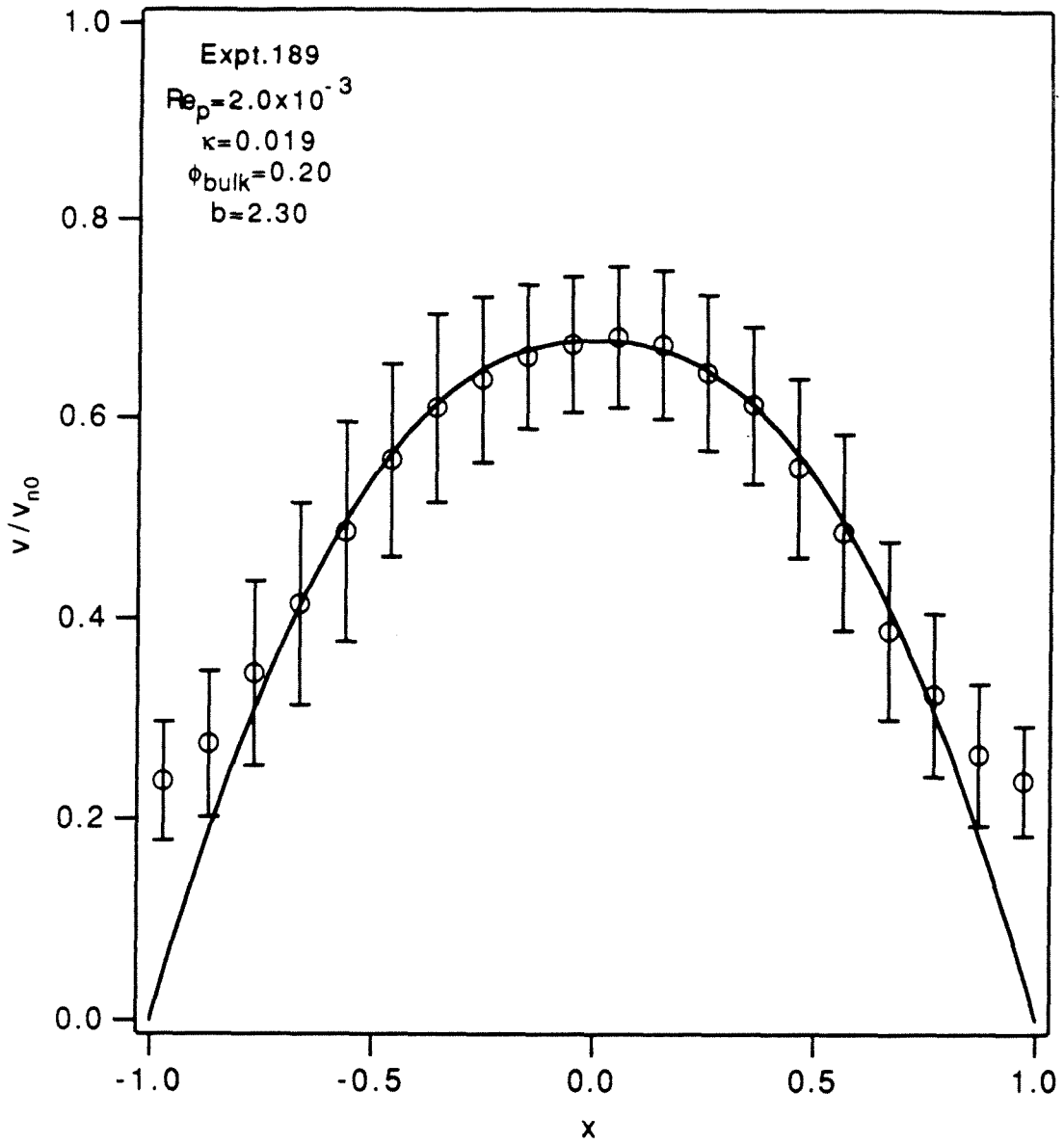


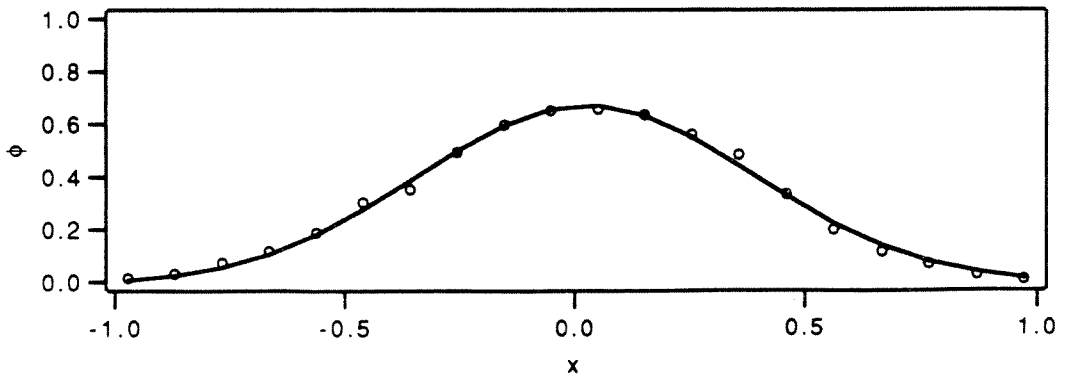
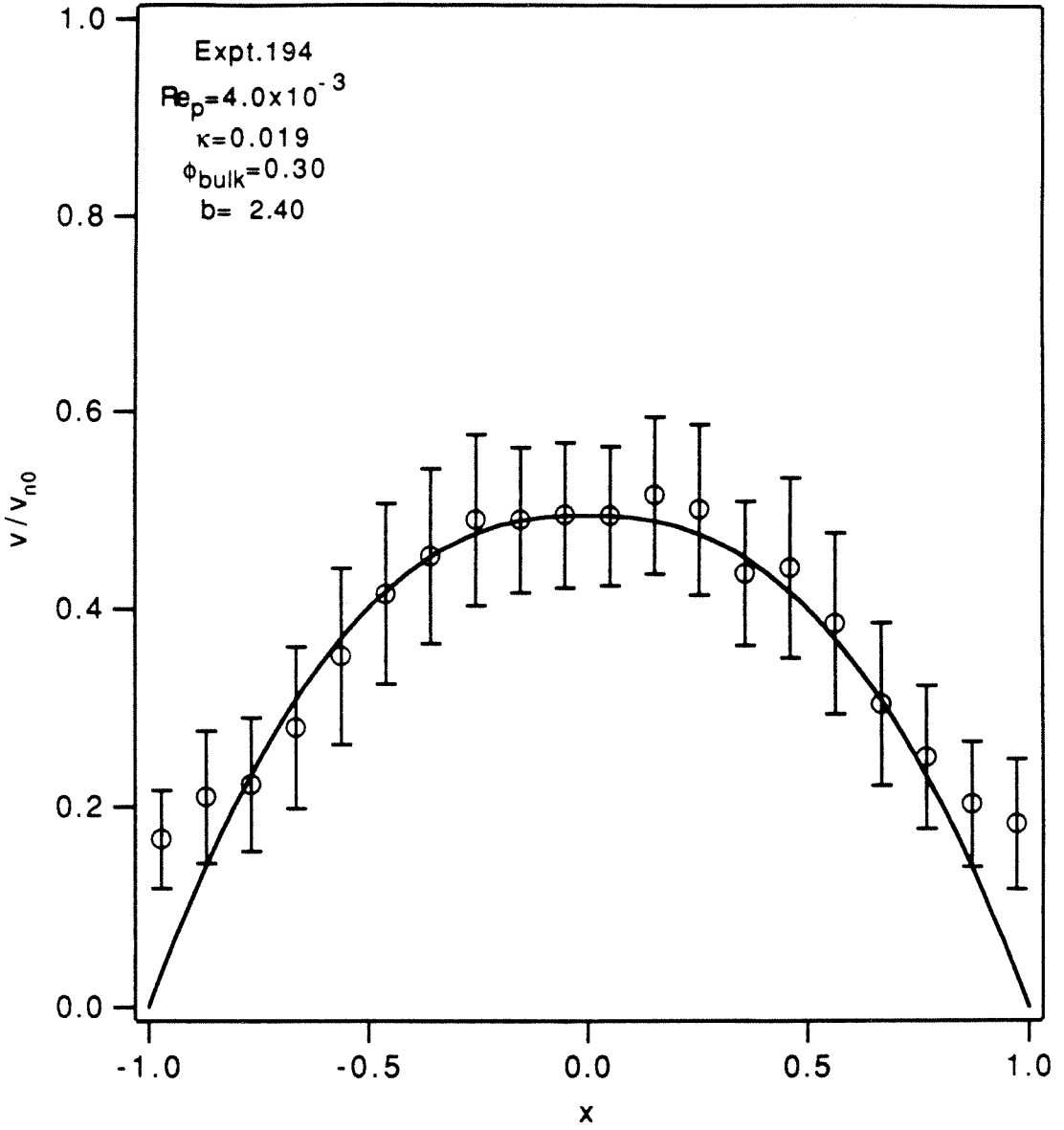


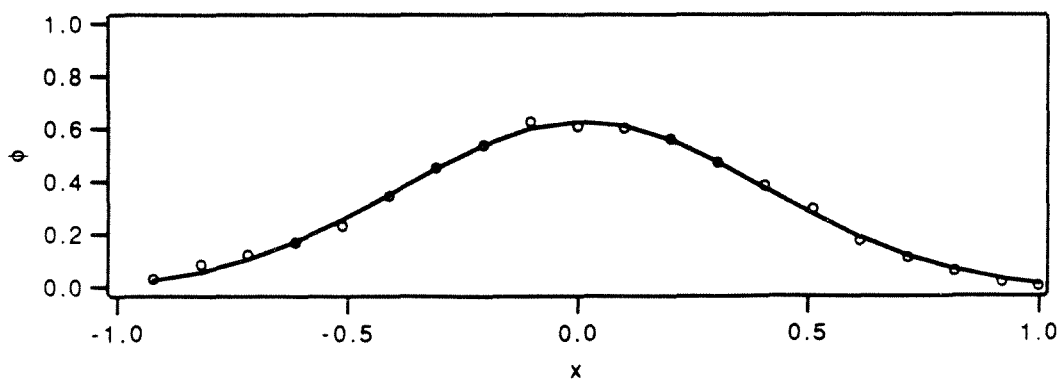
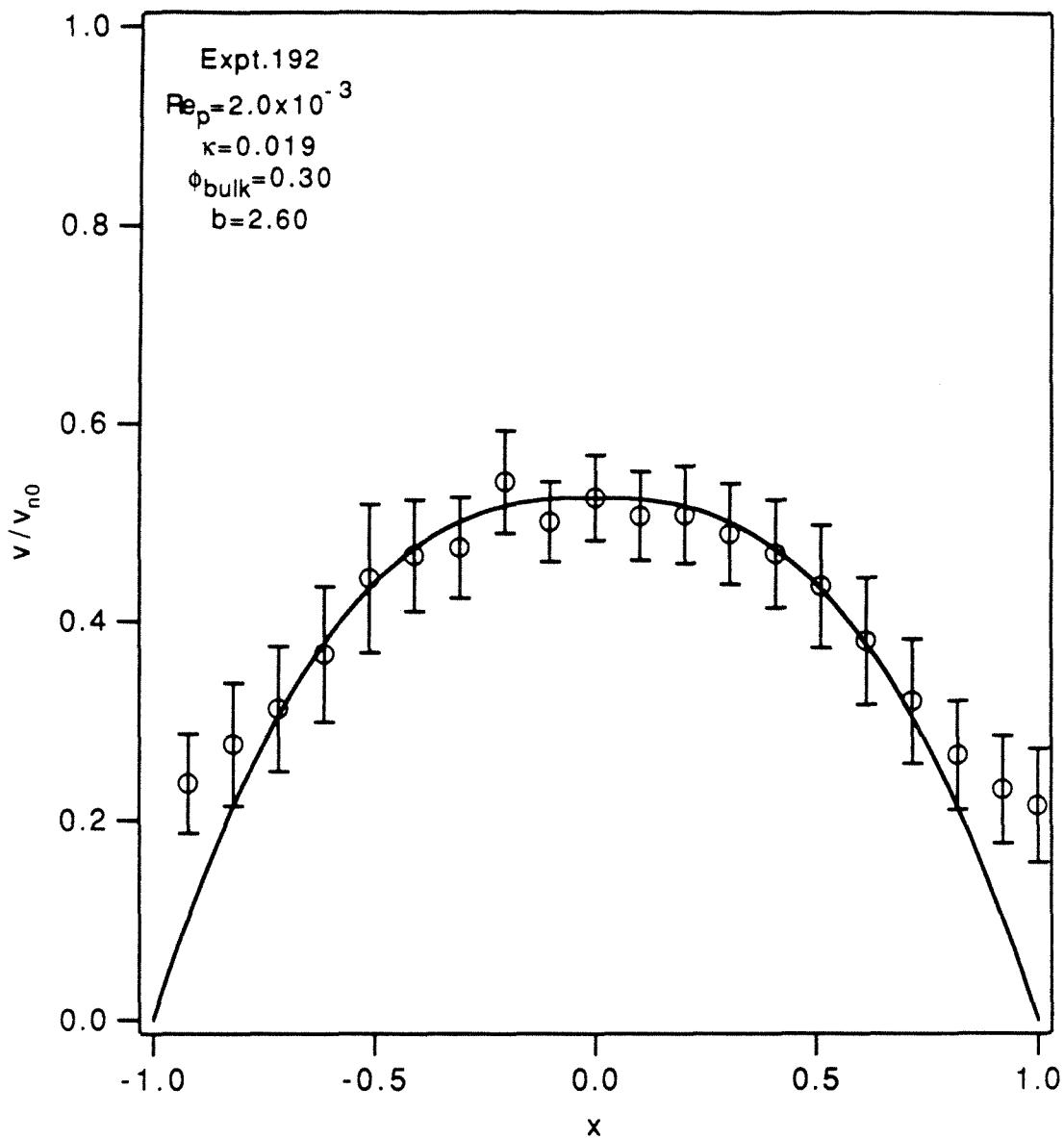


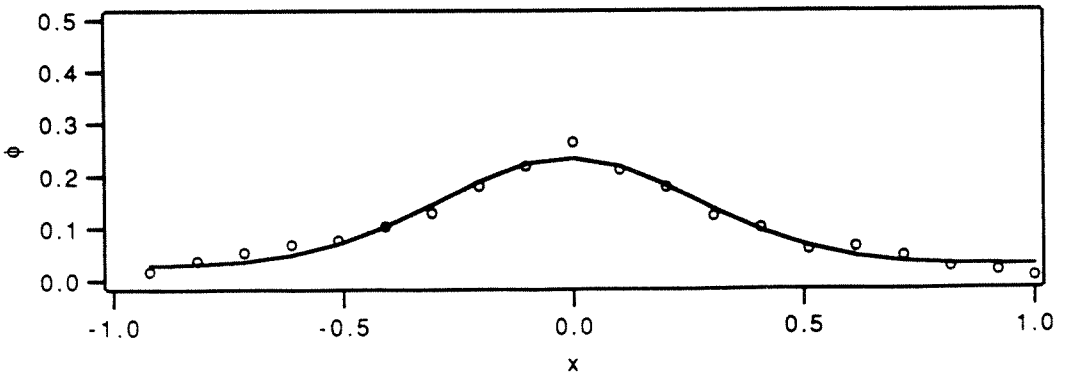
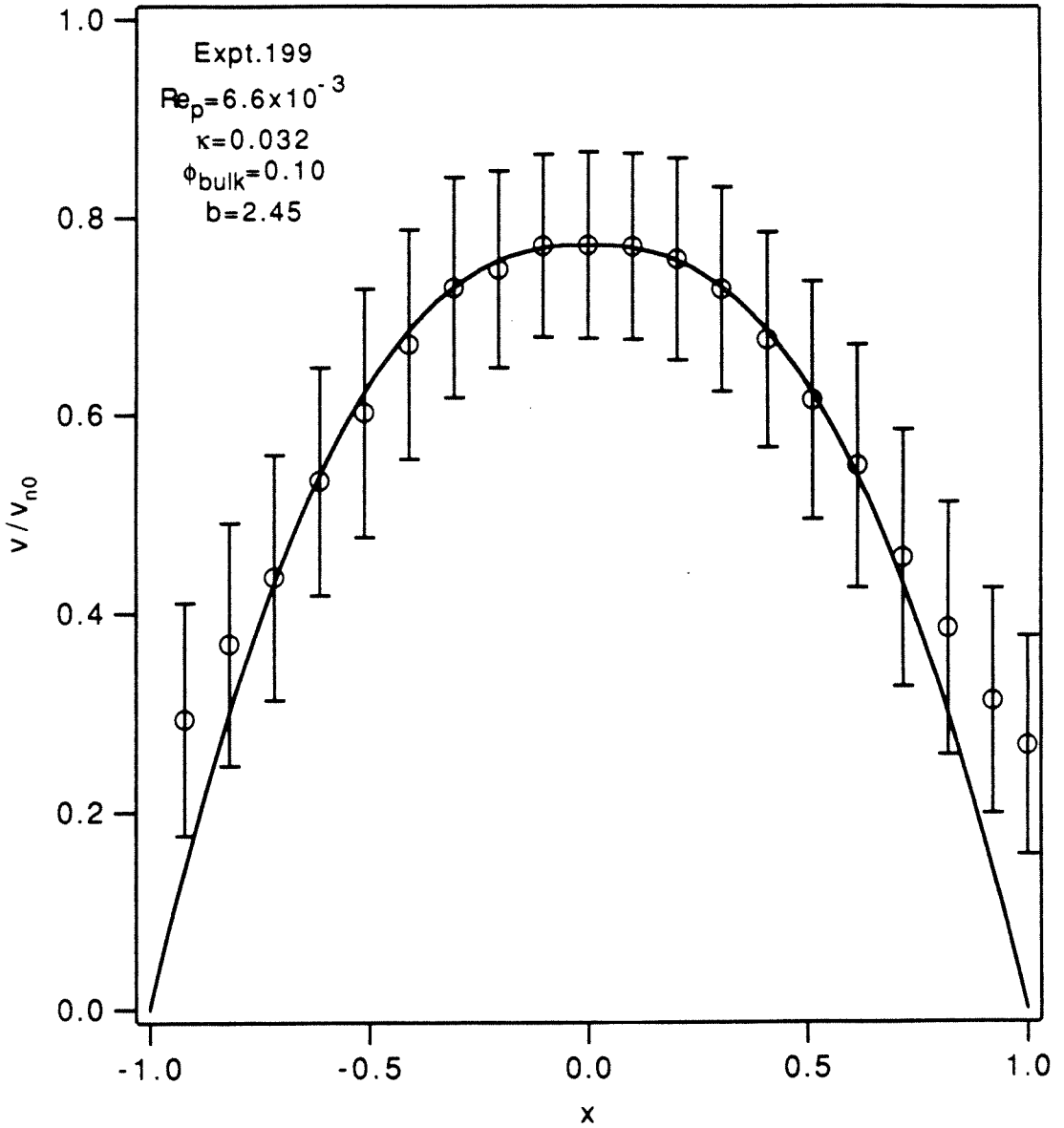


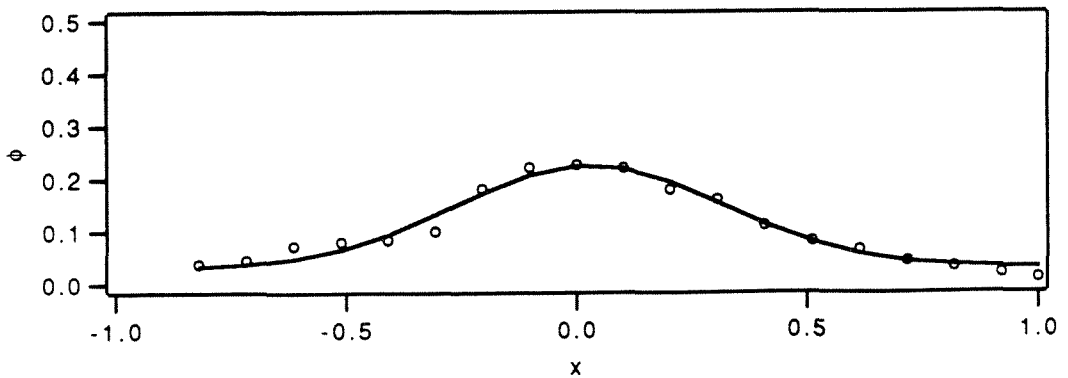
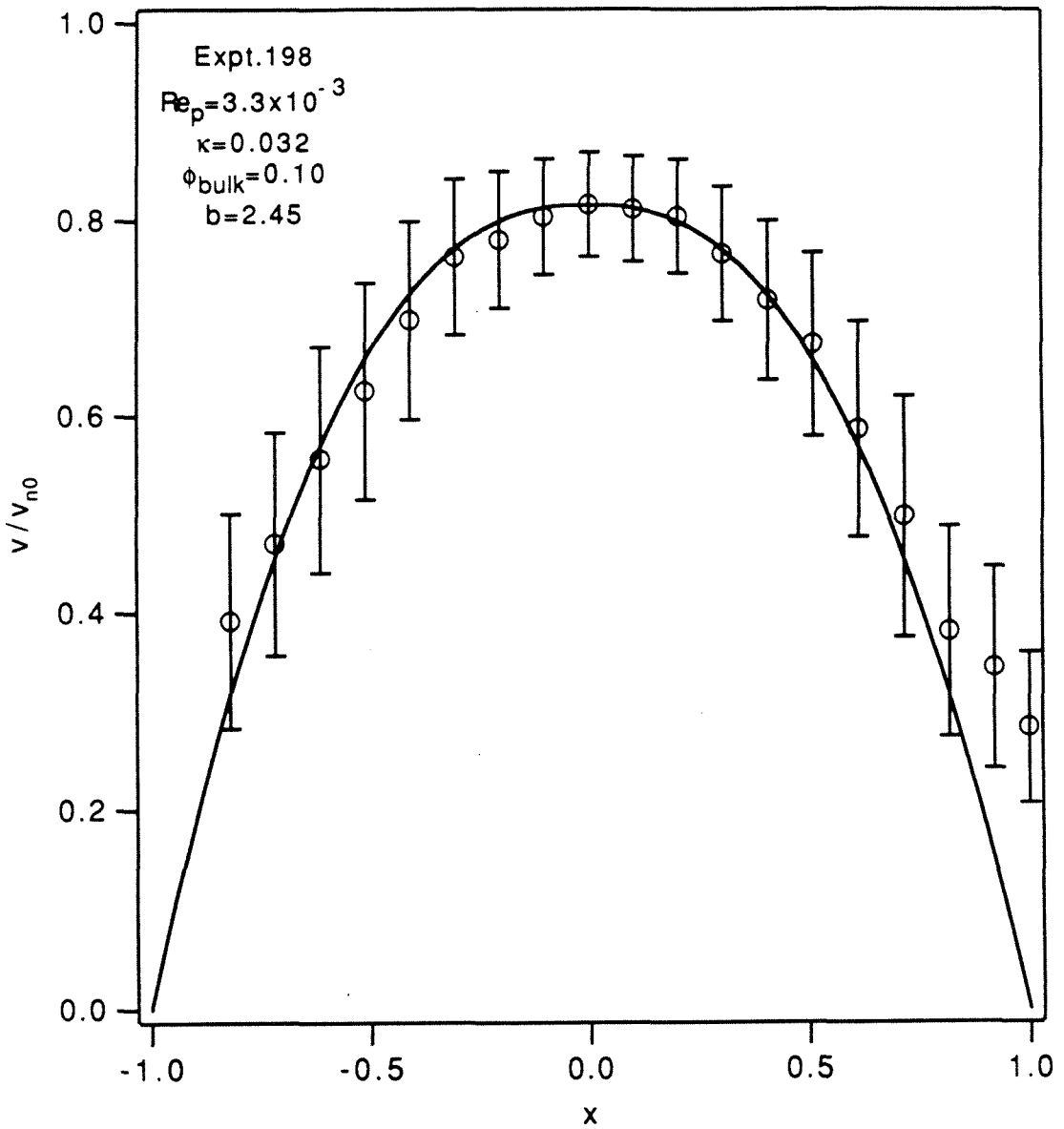


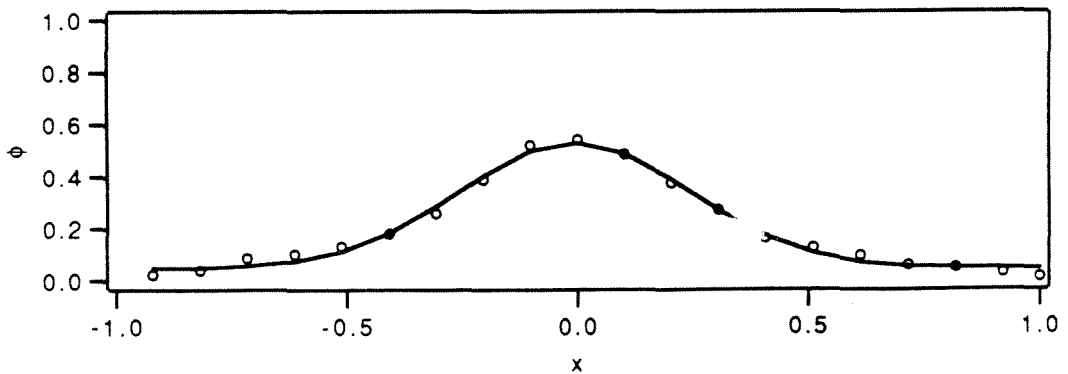
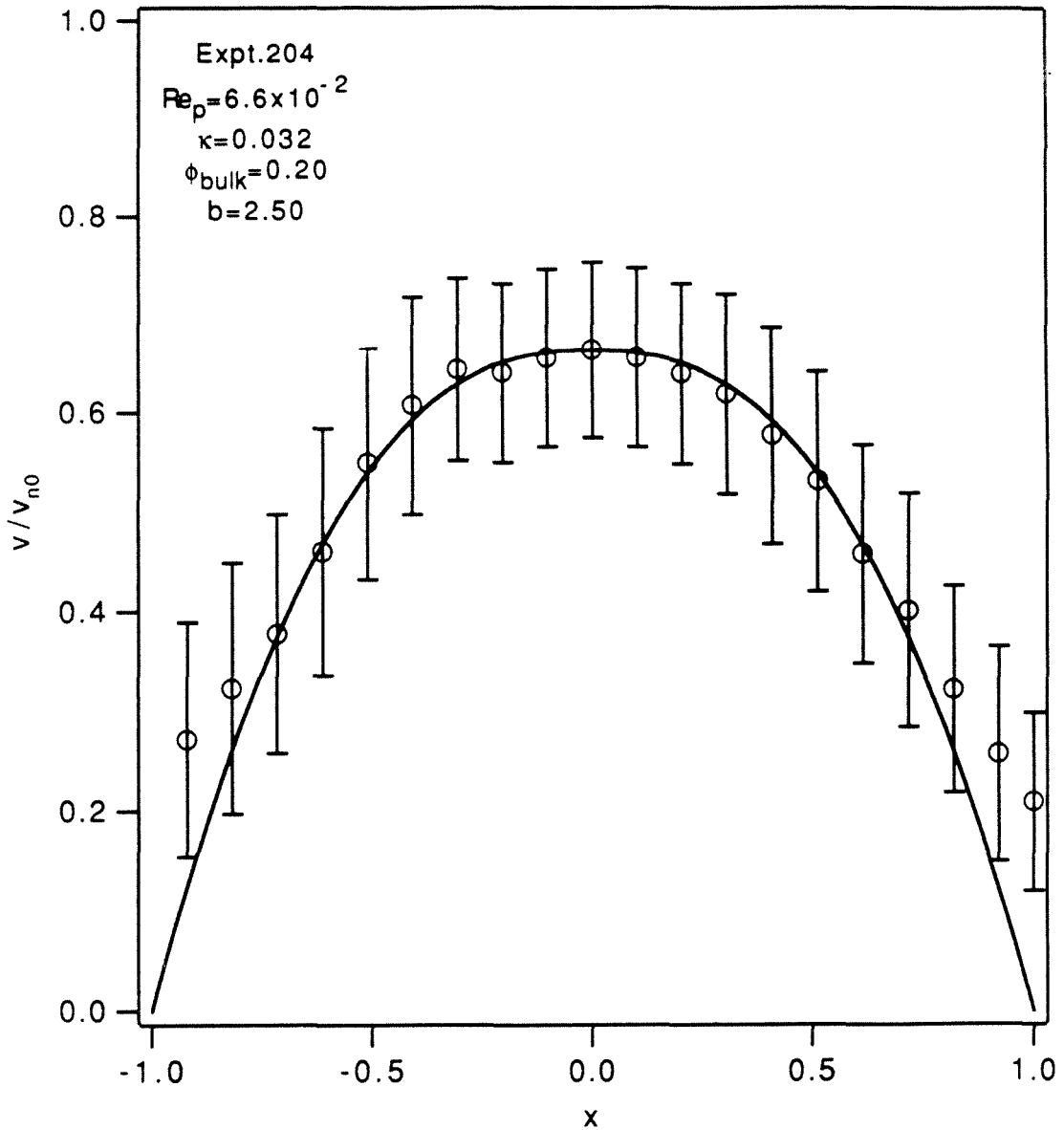


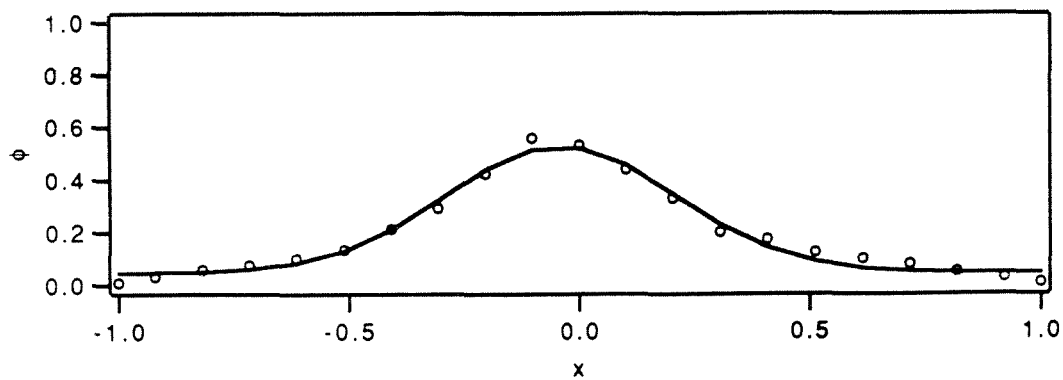
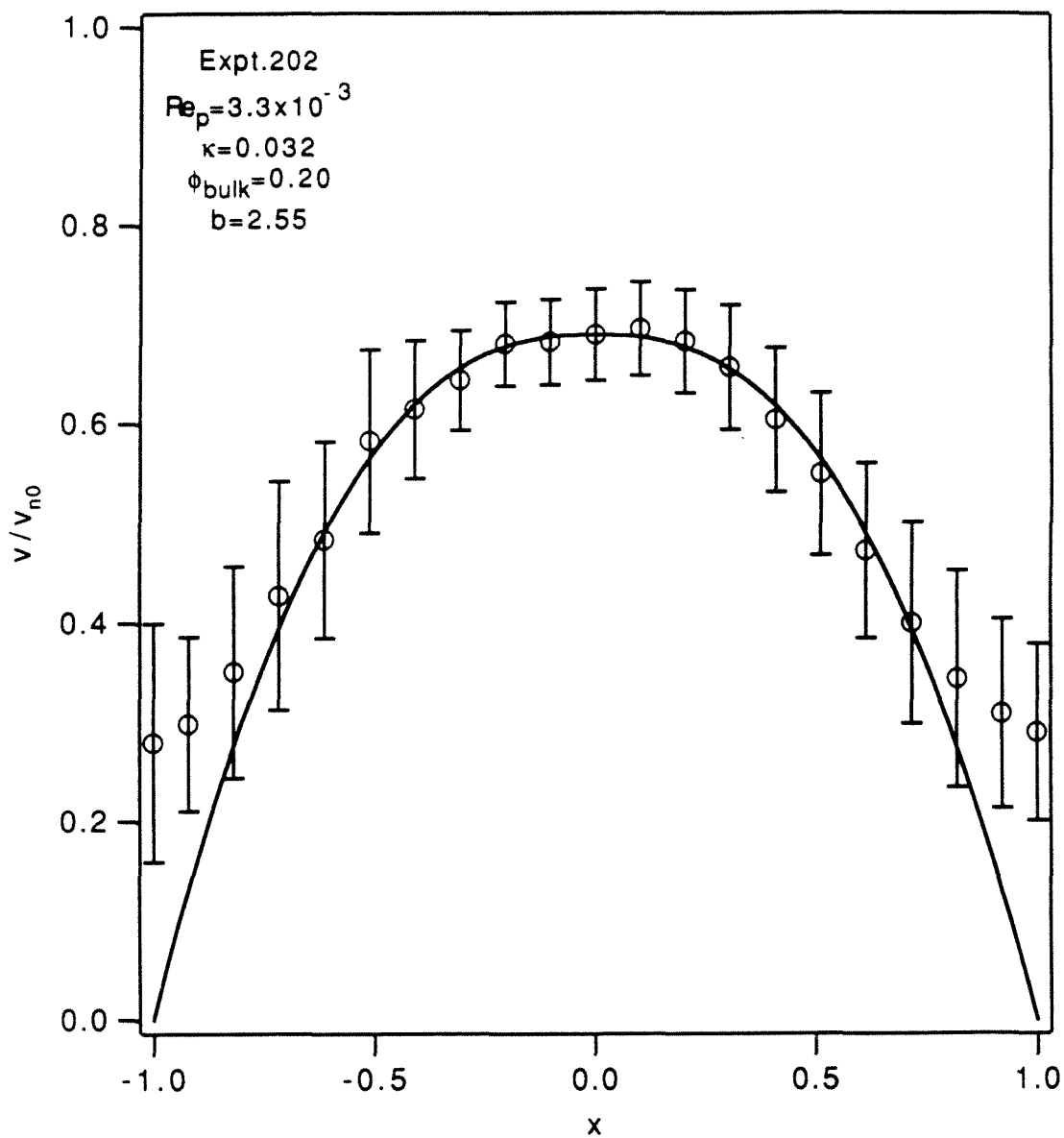


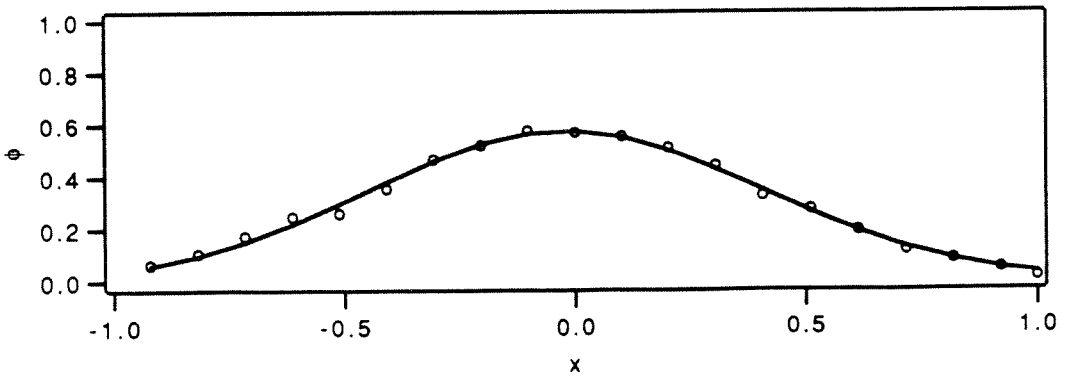
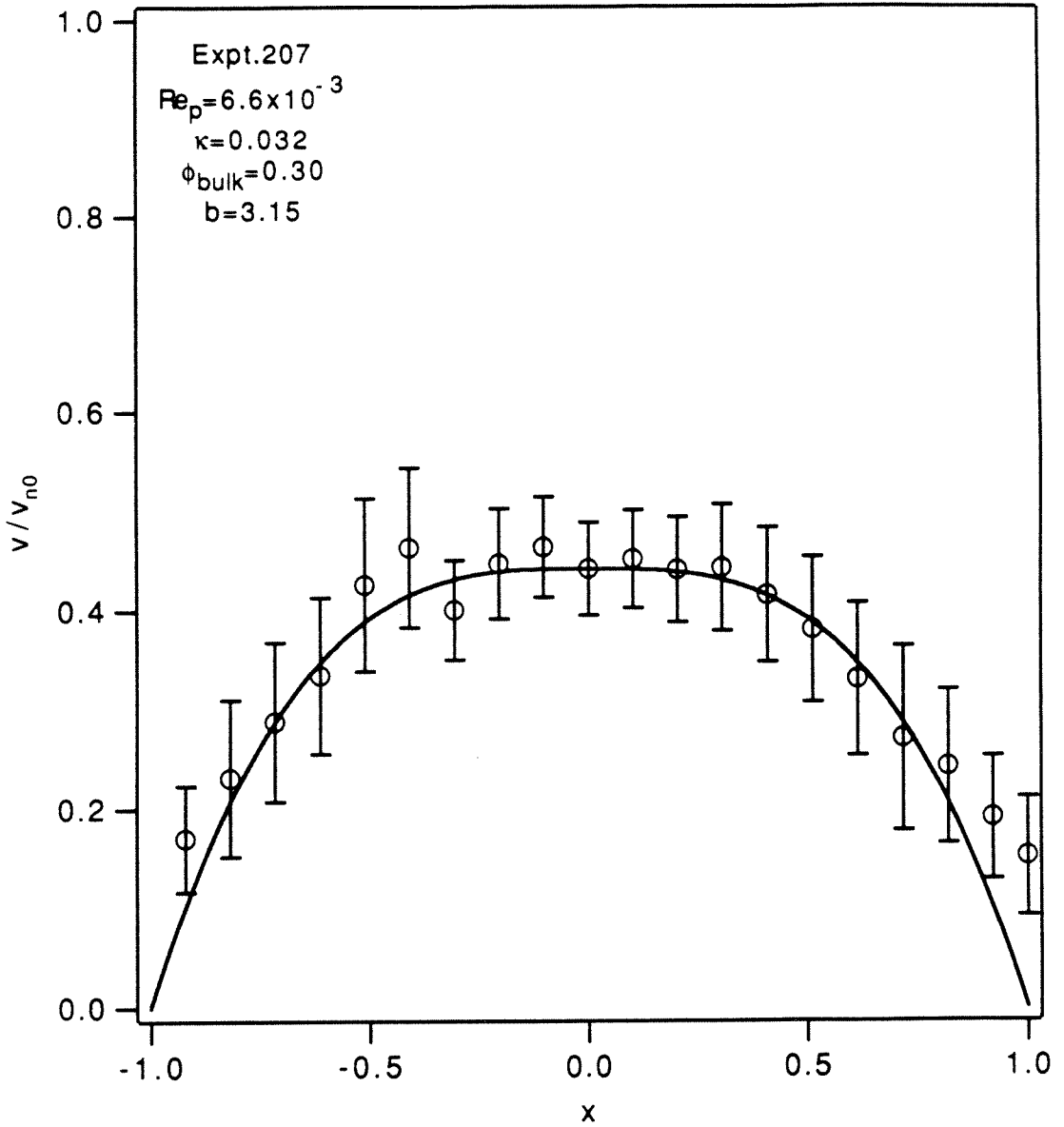


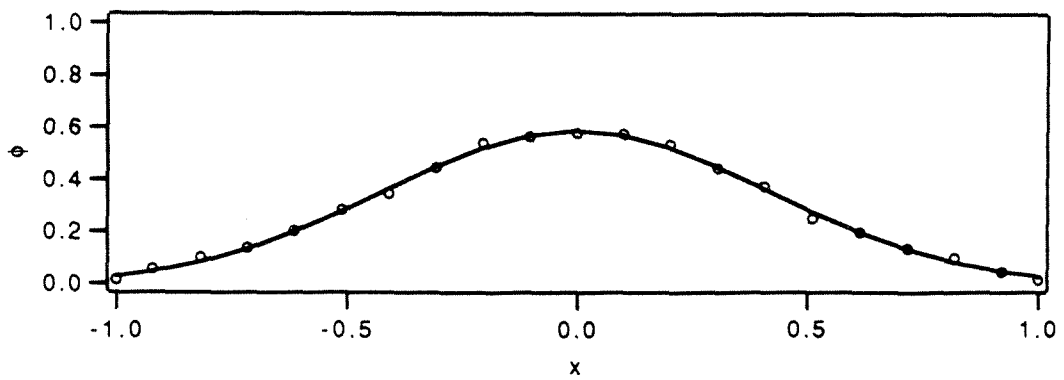
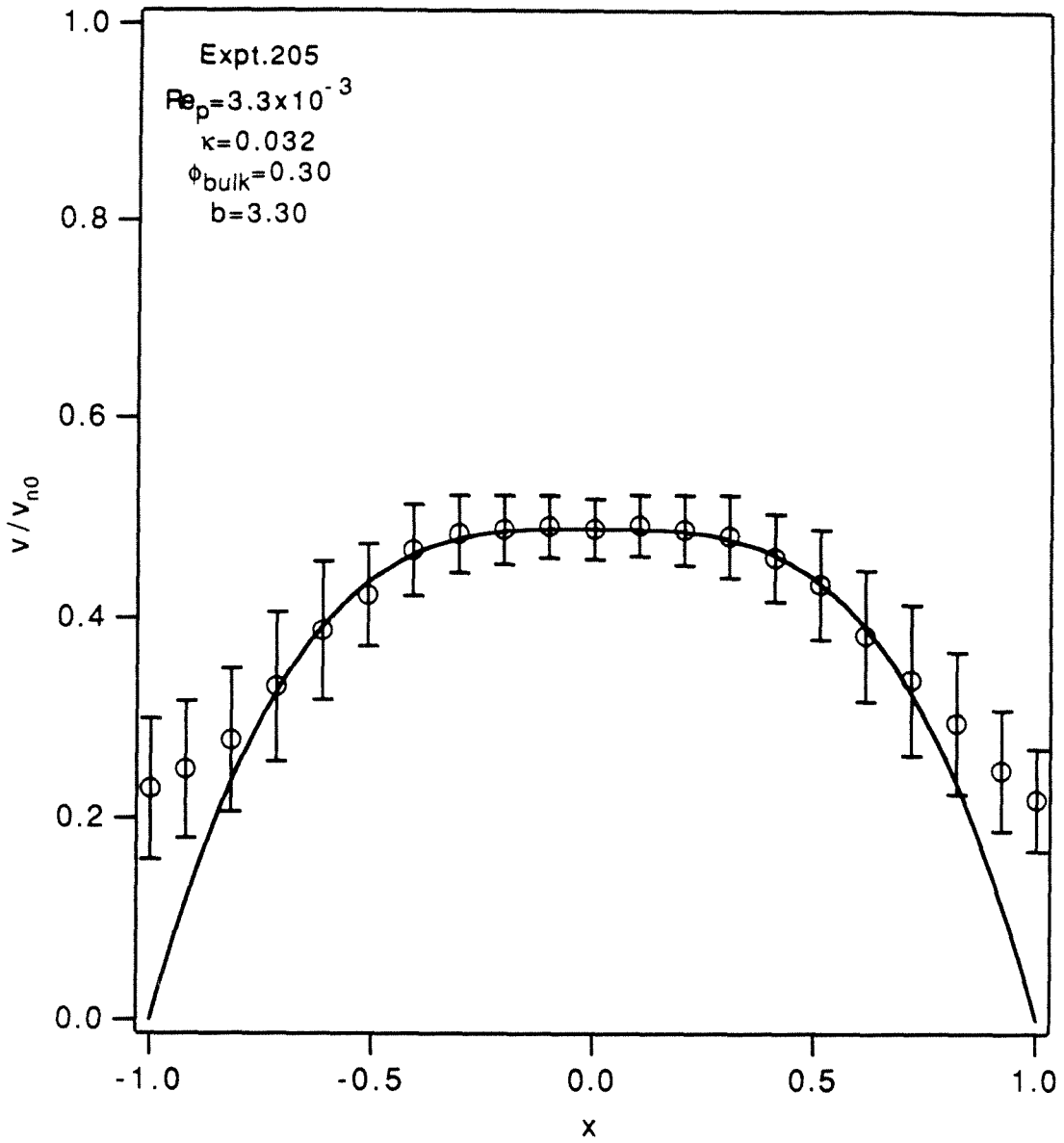


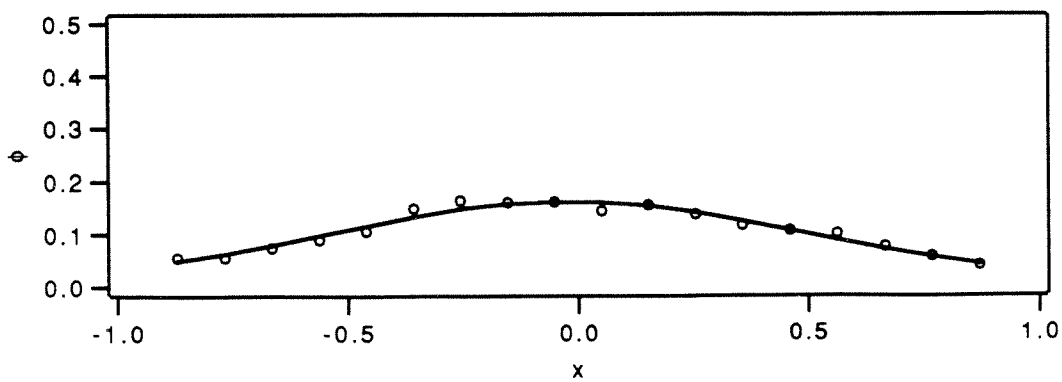
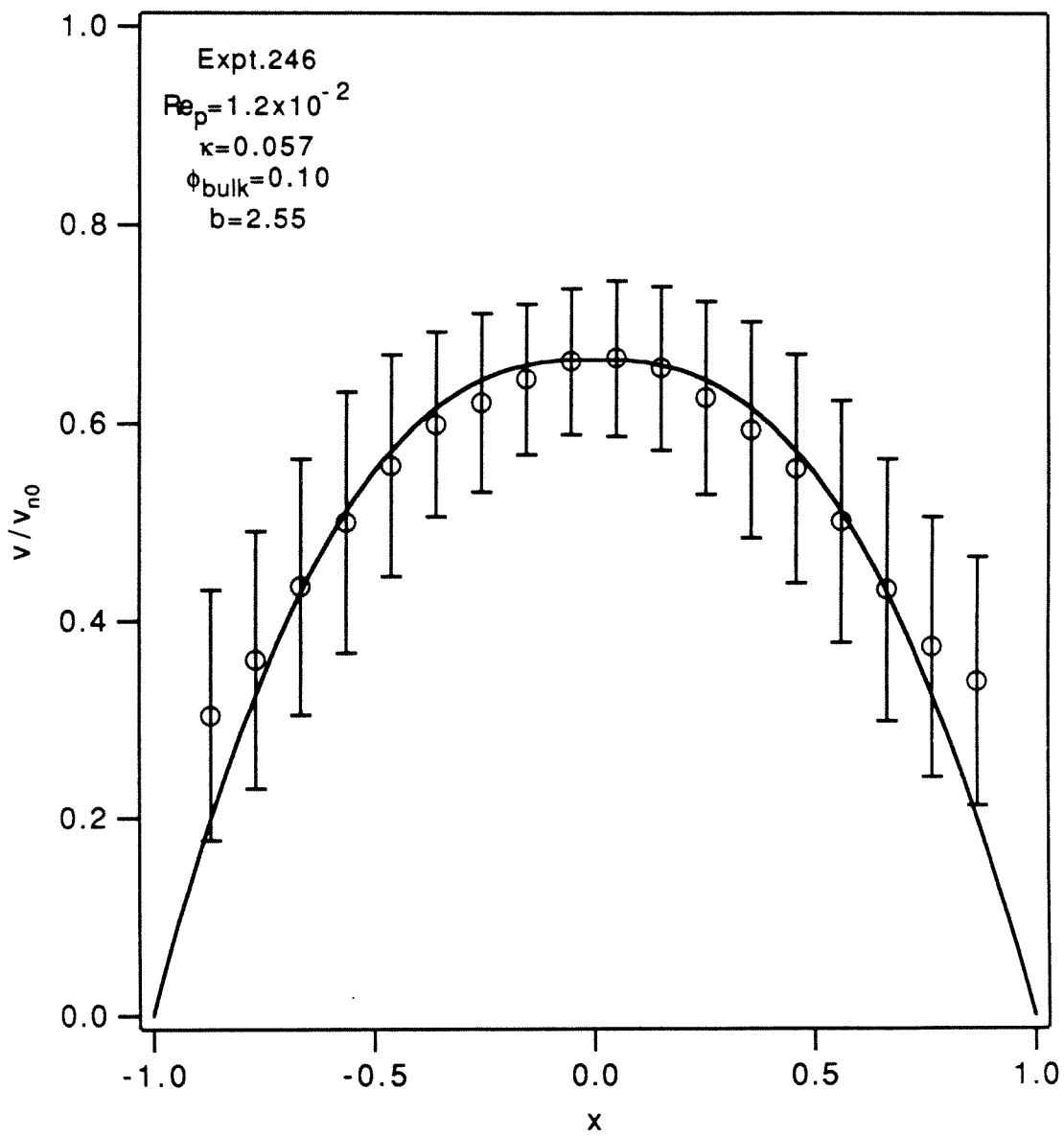


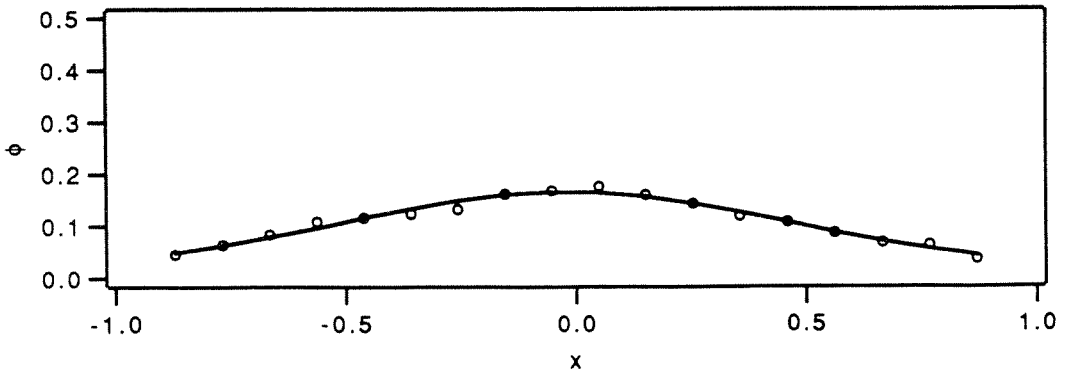
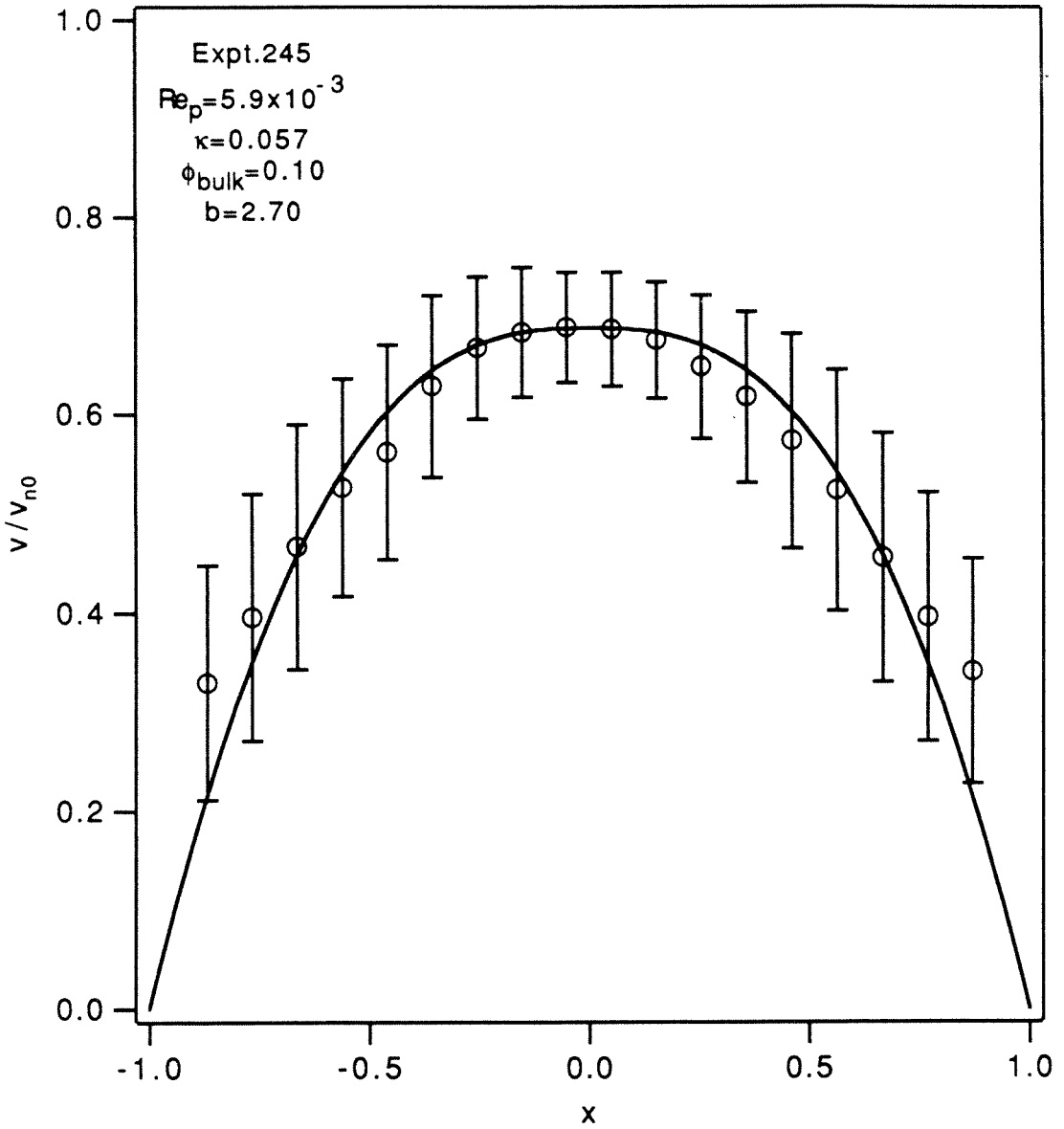


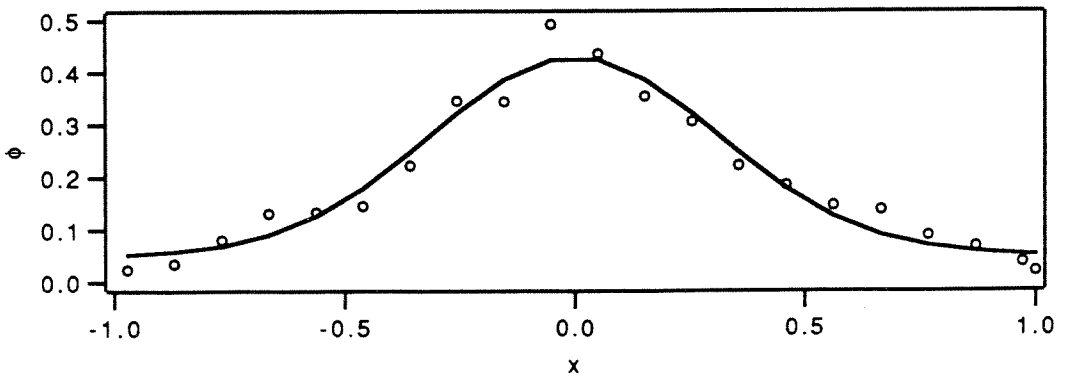
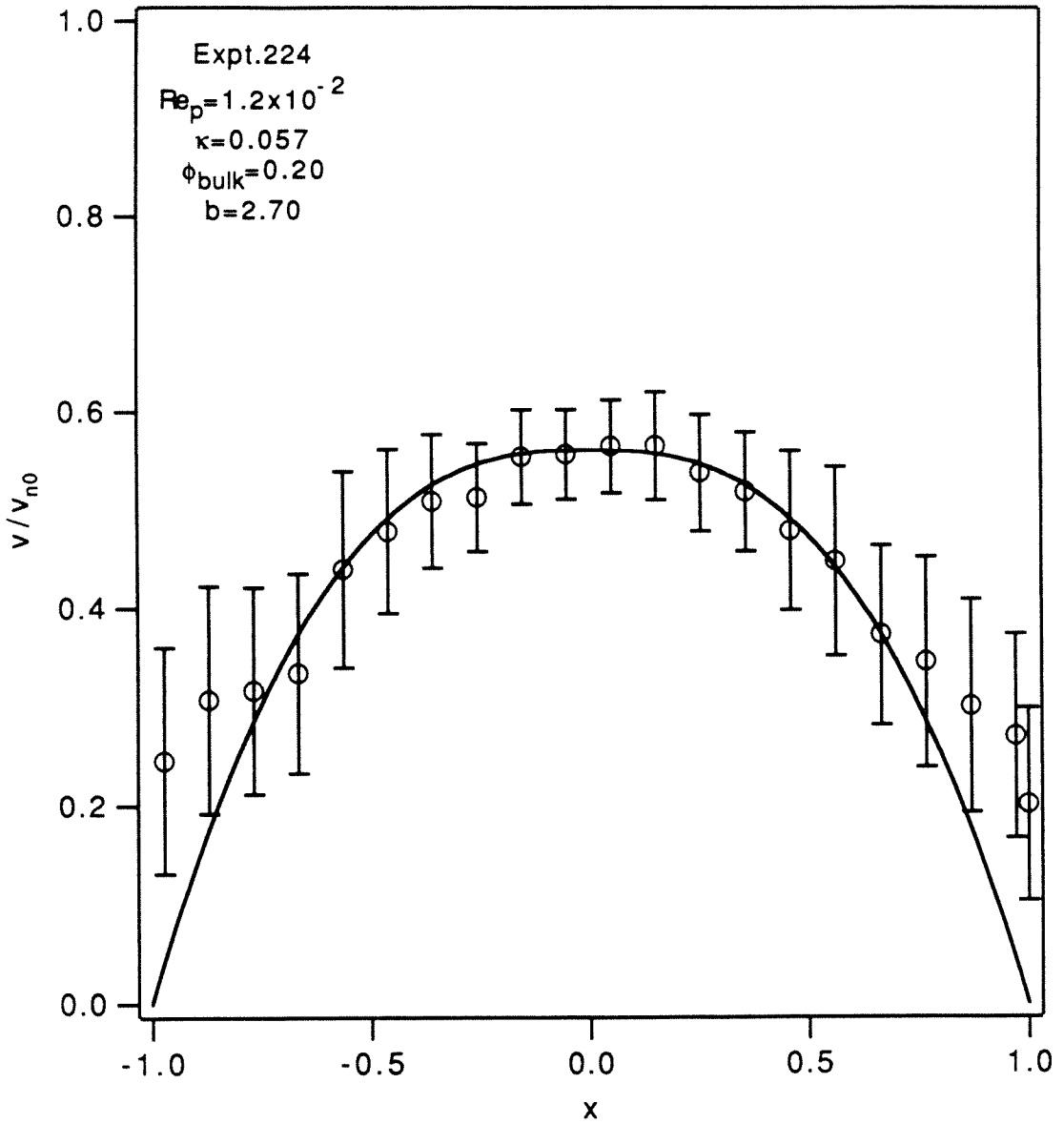


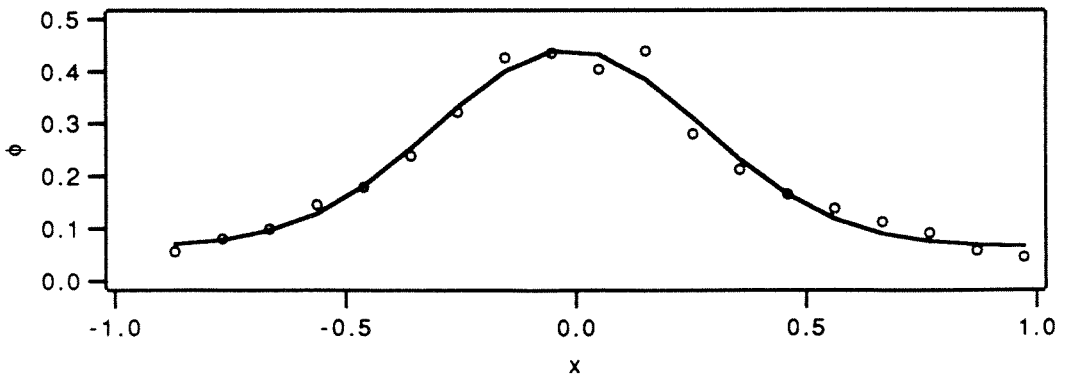
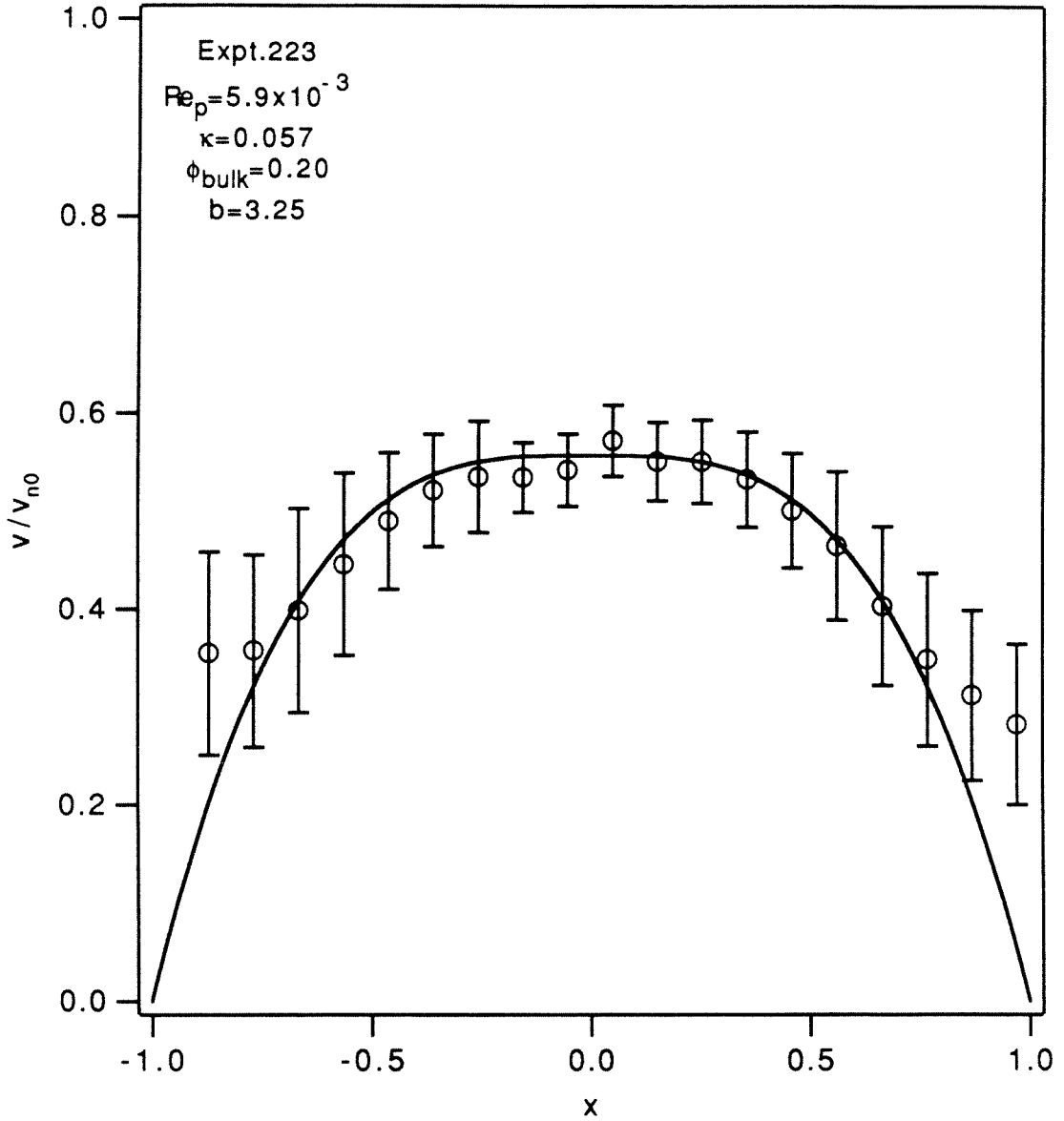


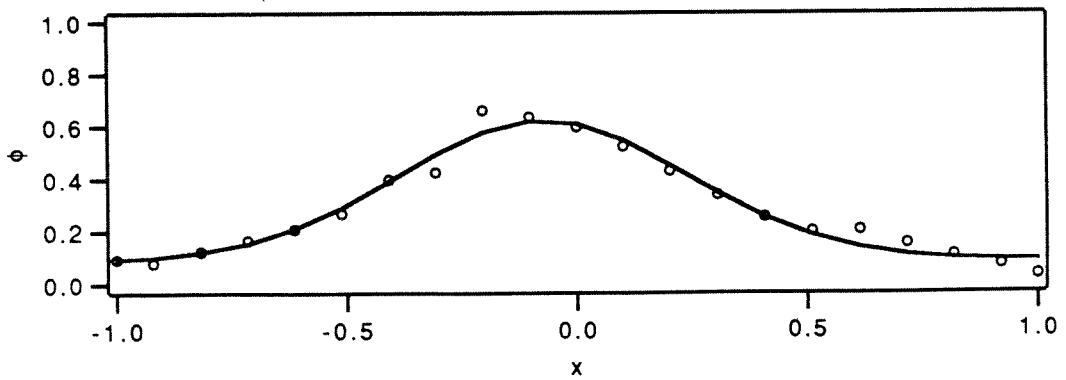
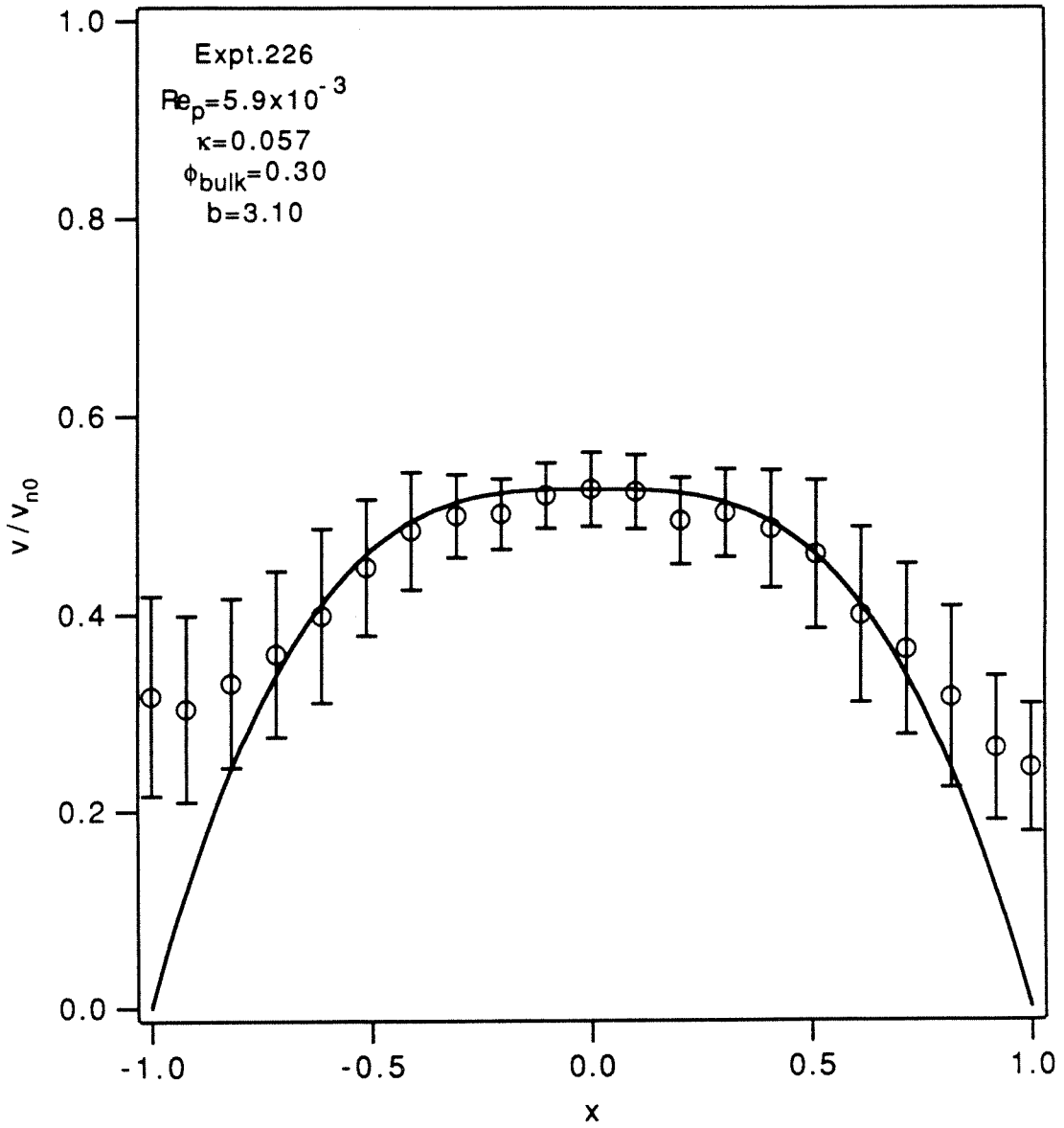






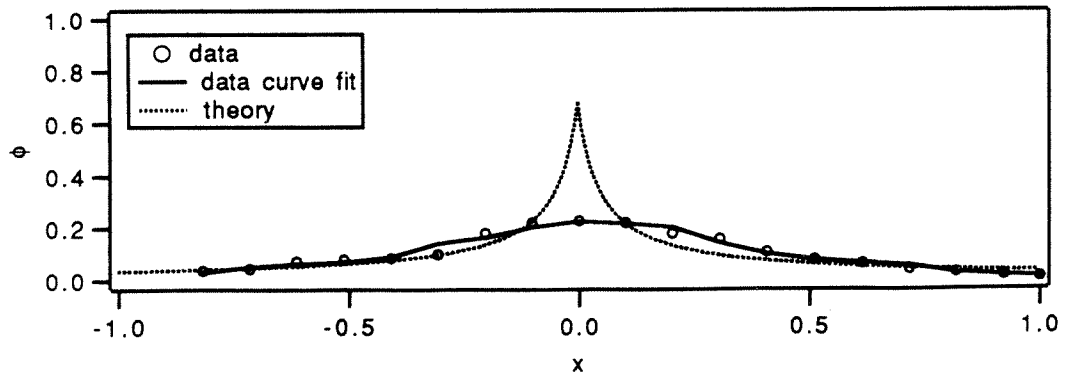
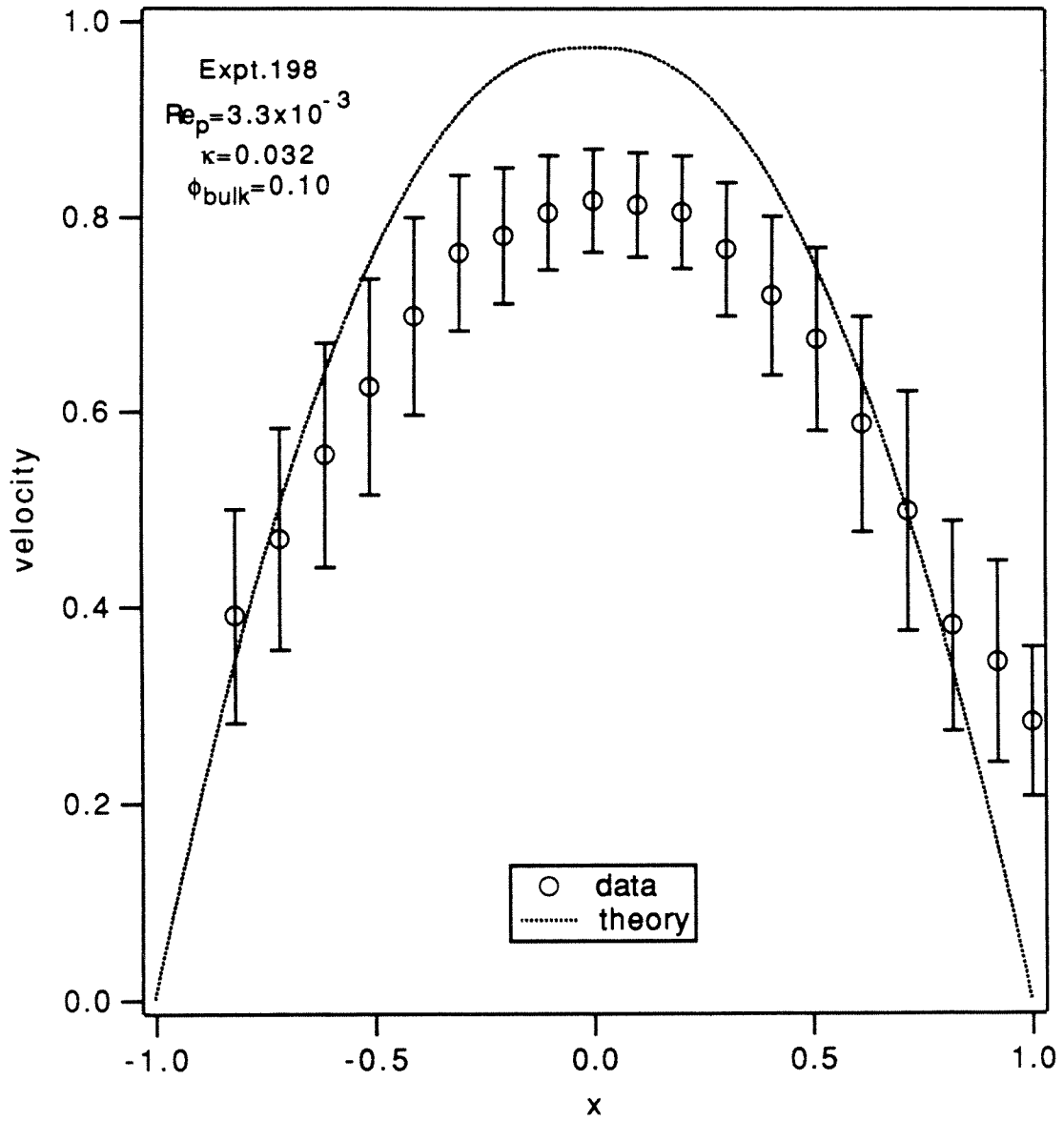


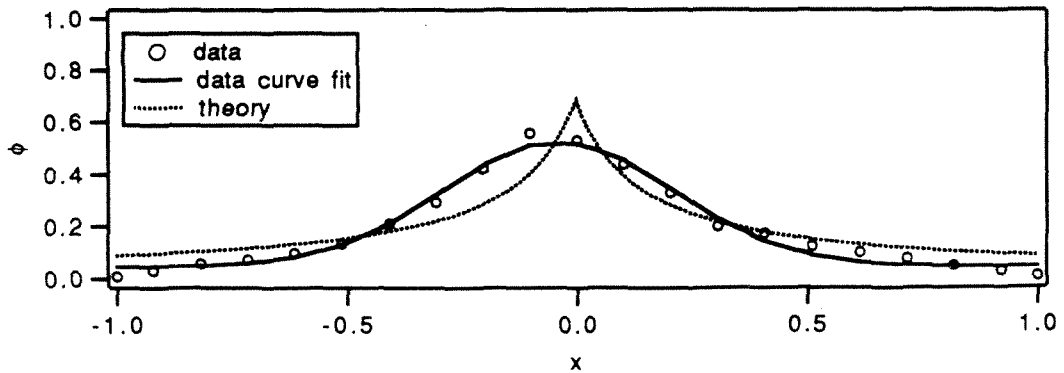
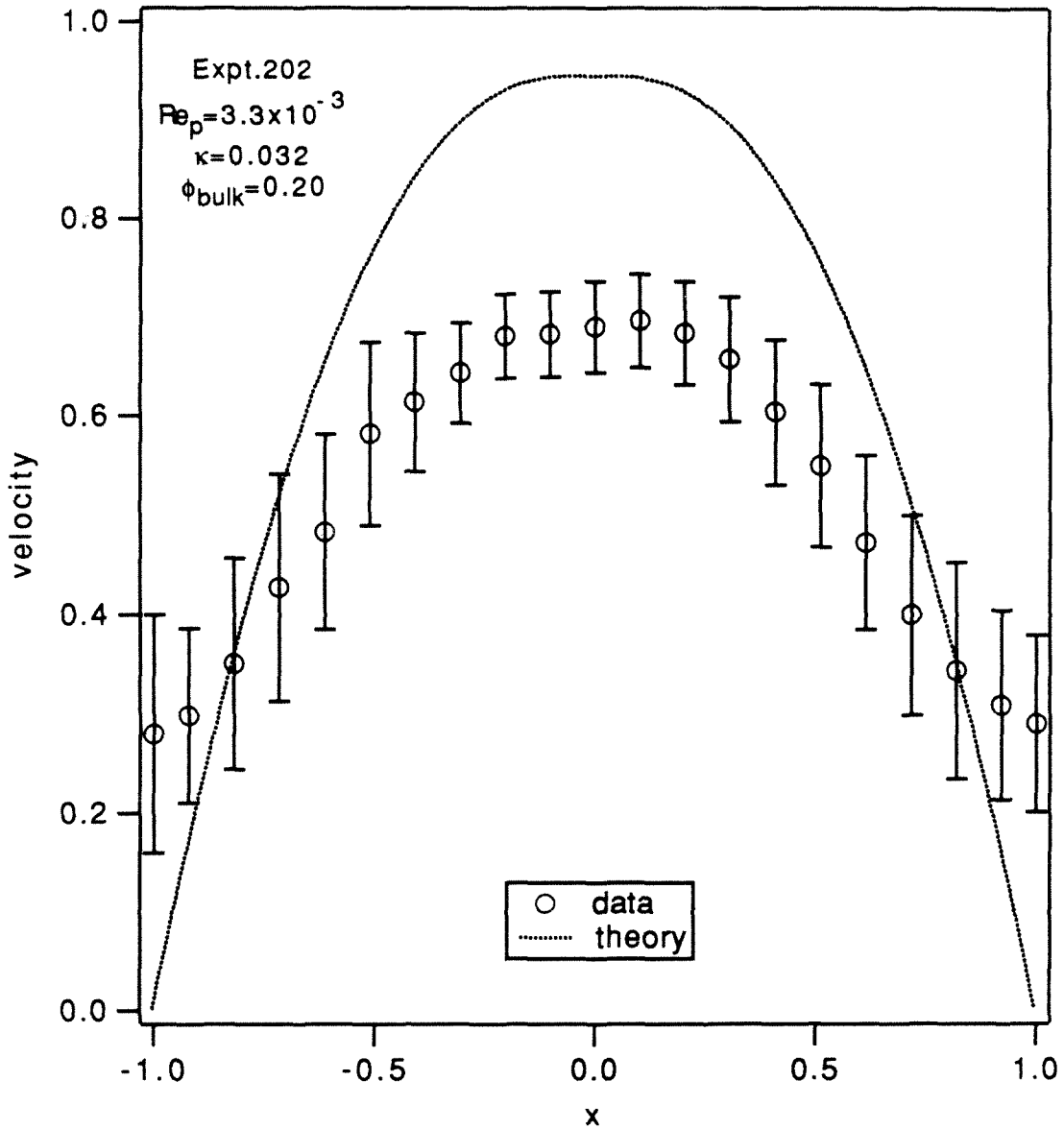


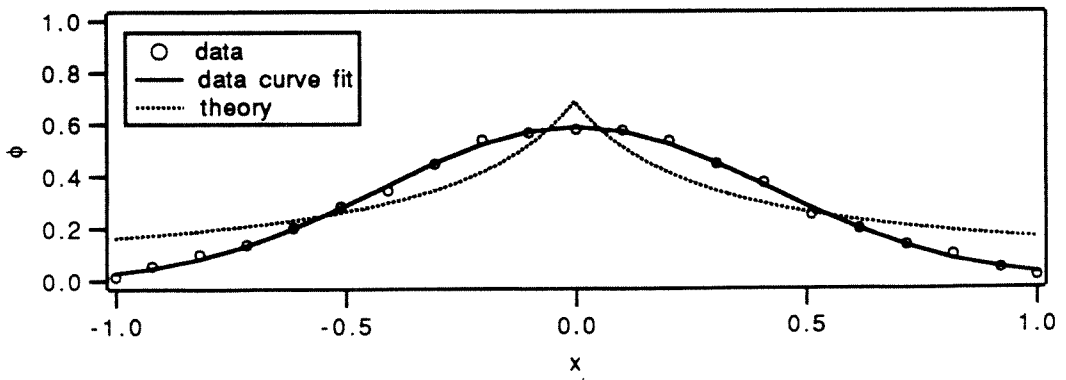
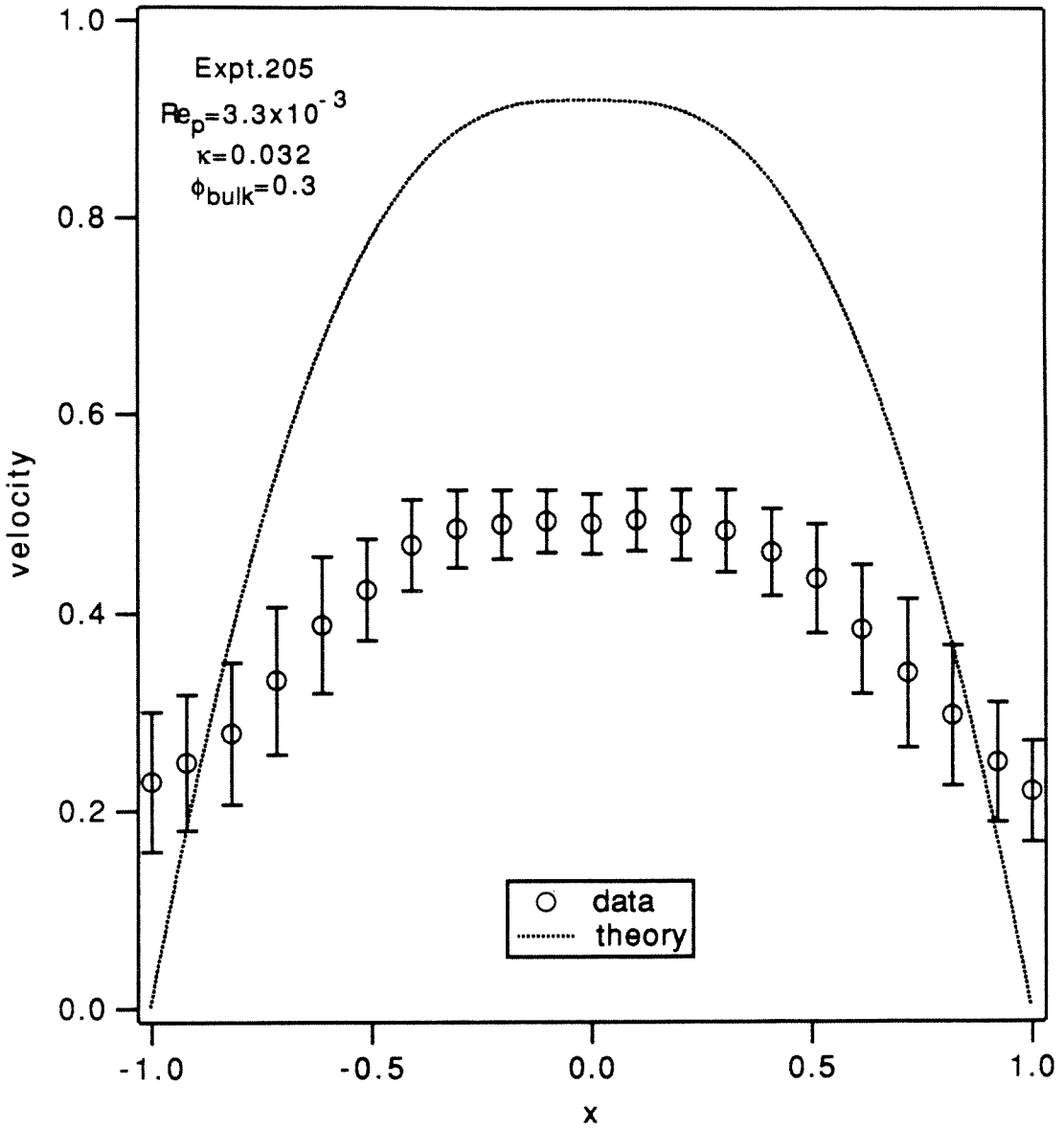


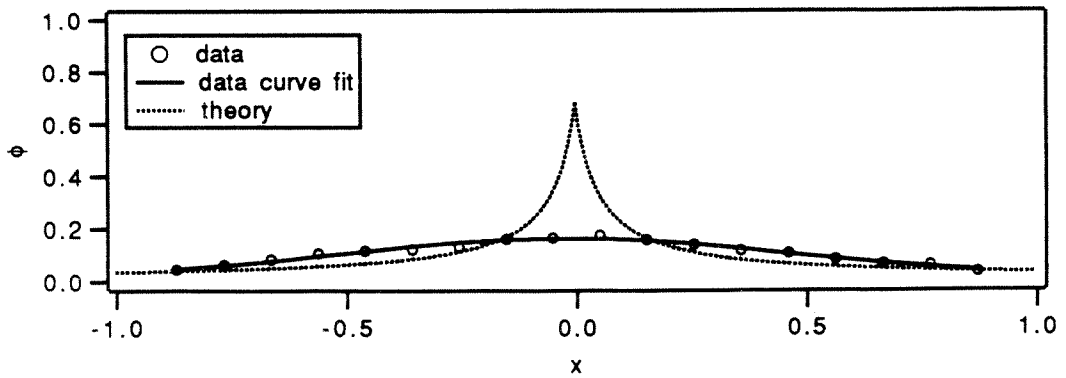
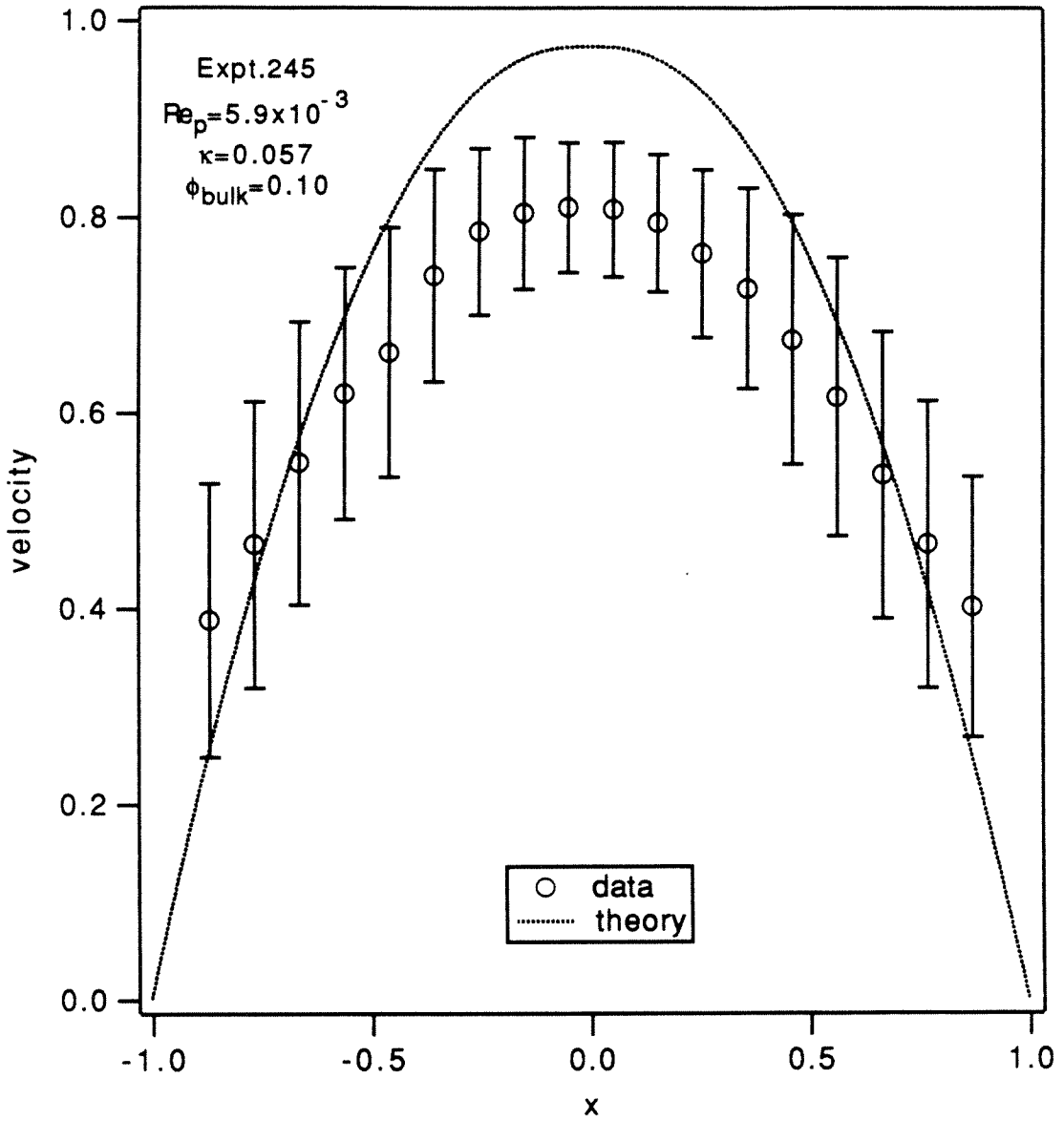
Appendix F

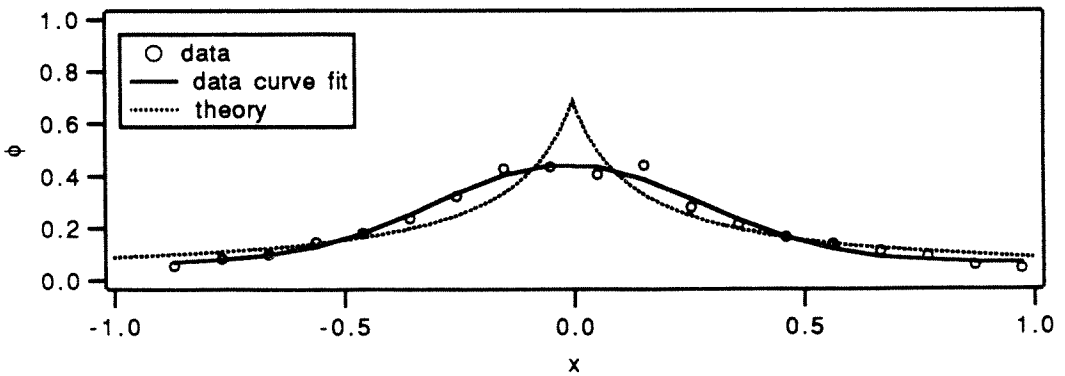
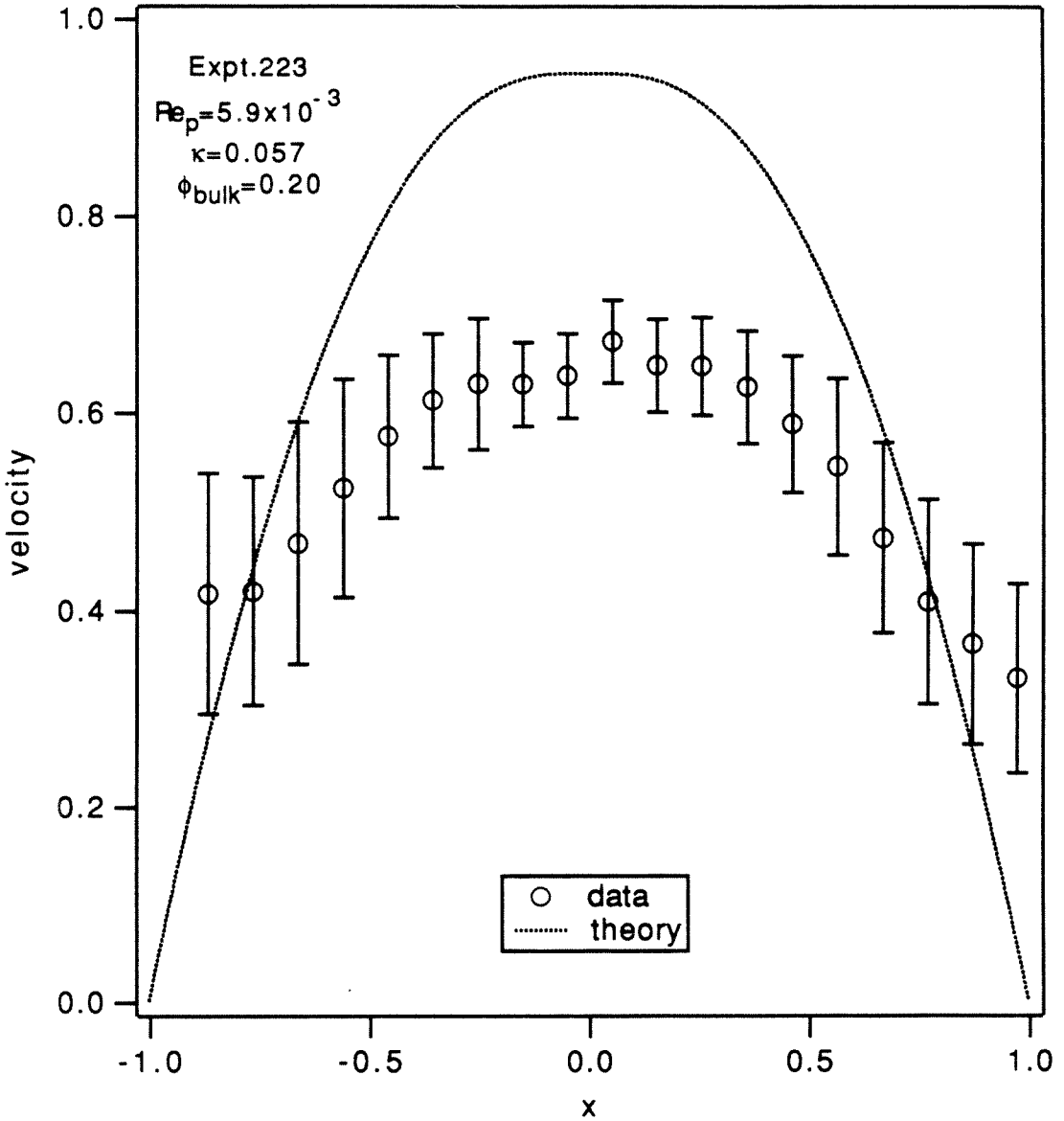
Comparison of theoretical prediction with experimental data.

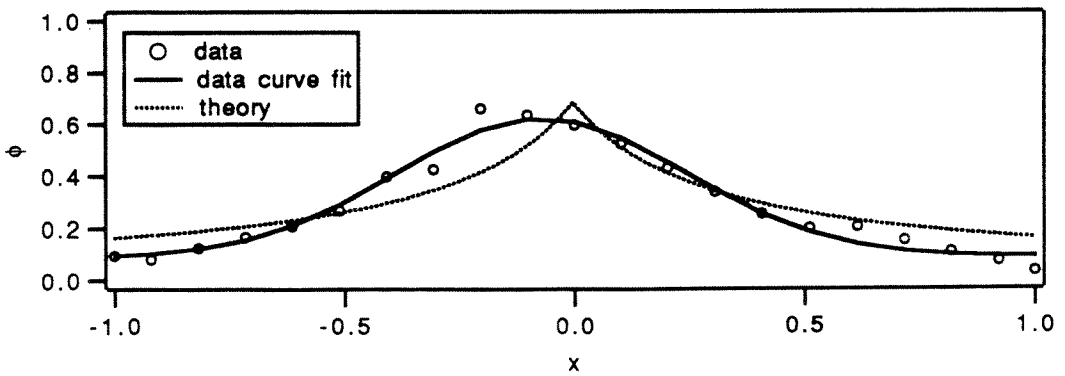
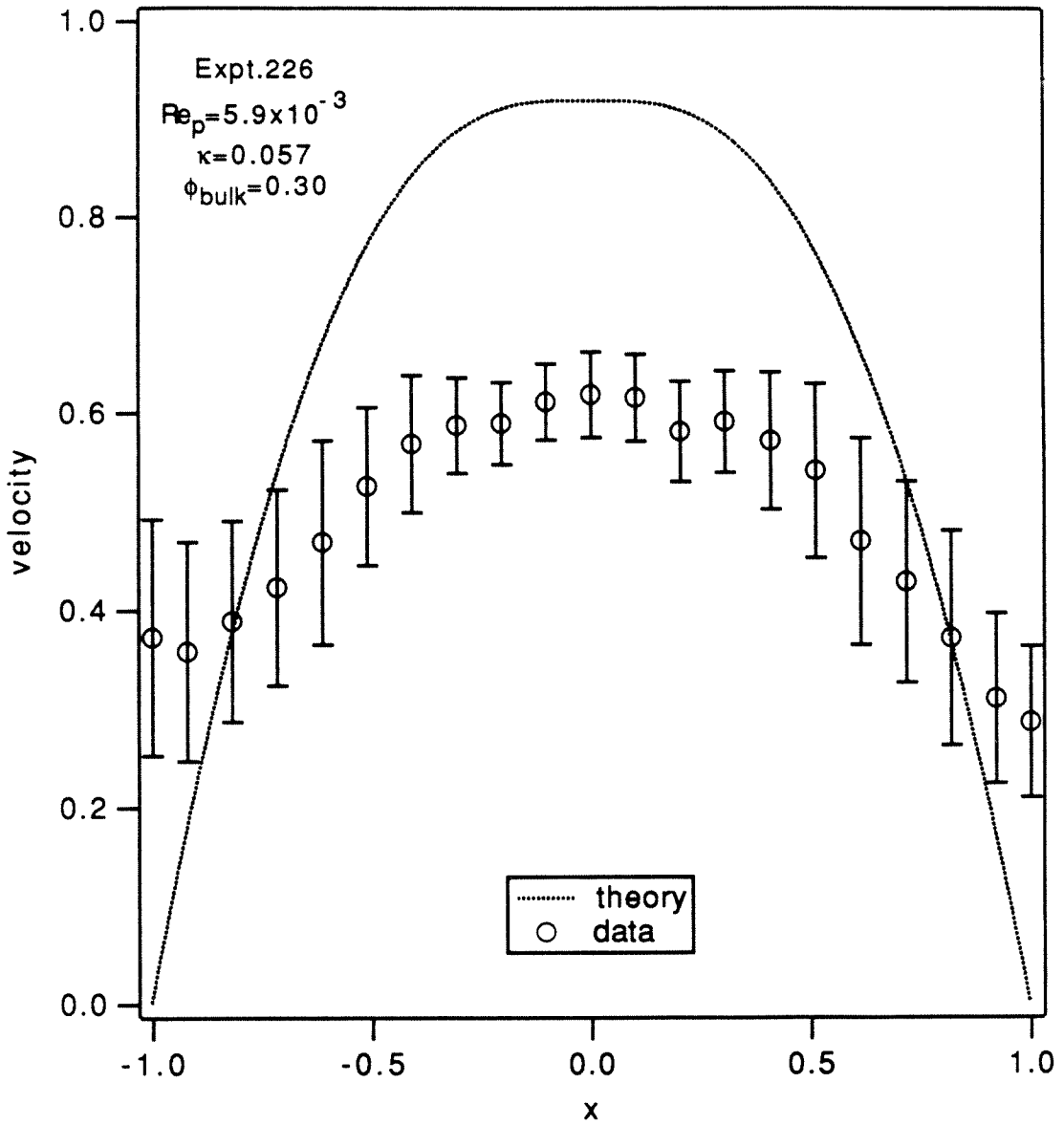












Chapter 4

Thesis Summary

This thesis consists of two parts; Part I deals with the stability of drop shapes in creeping flow and Part II concerns the flow of high concentration suspensions in a rectangular channel.

Chapter 1 is a numerical studies on the stability of drop shapes for translation through a quiescent fluid. Besides being a problem of fundamental interest, this study is motivated by the observation that the motion of viscous drops can provide a framework for understanding the dynamics of the deformation of biological cells and the behavior of aggregates of small particles. The specific problem we consider here is the translational motion of an initially nonspherical viscous drop through an unbounded and otherwise quiescent fluid in the creeping flow approximation. The two fluid phases are Newtonian, immiscible and the interface is characterized by a constant interfacial tension. The most important parameter in this problem is the capillary number

$$Ca \equiv u_c \nu a / \sigma \quad (4.1)$$

It is the ratio of two competing effects: viscous force which tends to deform the drop, and interfacial tension which tends to minimize deformation. The initial drop shapes are ellipsoidal and the magnitude of the deformation is characterized by the Taylor parameter

$$\Delta \equiv \frac{L - B}{L + B} \quad (4.2)$$

where L corresponds to the length along the axis of rotation and B to the breadth in the perpendicular direction.

The basic result of the numerical simulation is that for a given Ca , an initially nonspherical drop reverts back to a sphere as it translates provided that the initial deformation is small enough. However, if the initial deformation is above a critical value, the drop deforms continuously; we refer to such a drop as unstable. In particular, if the drop is initially a prolate ellipsoid, the front of the drop returns to a hemispherical shape while the rear of the drop develops a tail which increases in length as a function of time. Eventually, the tail begins to pinch and it appears likely that the drop will break as the tail separates from the parent drop. On the other hand, for initially unstable oblate drops, the type of deformation is qualitatively different. It is found that the front of the drop returns to a hemispherical shape; however, the rear of the drop develops a cavity which closes up on itself as the drop moves.

By performing simulations for various combinations of initial drop shapes and viscosity ratios, neutral stability curves as a function of viscosity ratio are constructed. The key features of the behavior of nonspherical viscous drops as they translate can be extracted from these stability curves. First, it is clear that for the same initial deformation, a more viscous prolate drop is more stable than a less viscous one; the contrary is true for initially oblate drops. Second, we find that the critical capillary number, above which the drop becomes unstable, depends on the viscosity ratio more strongly for initially oblate drops. Finally, these stability curves reemphasize the point that drops at nonzero Ca can be unstable to finite initial deformation. For a given Ca , the drop is unstable provided that the initial deformation is larger than some critical value (or vice versa, for a given initial deformation, the drop is unstable if the capillary number is above the critical capillary number).

In Chapter 2, we study the behavior of viscous drops translating in a quiescent fluid experimentally. The motivation of this investigation is three-fold. First, we

seek confirmation of the two distinct modes of unstable drop deformation discussed in Chapter 1. Second, the numerical studies only consider idealized initial drop shapes (axisymmetric ellipsoids); it is important to ascertain whether the qualitative behavior of drop deformation as discovered by the numerical studies would apply to real systems with non-ideal initial drop shapes. Finally, the limitation of the computer simulations precludes the analysis of drop dynamics beyond the point when a thin neck appears in the deformation of prolate drops or when the rear cavity closes up on itself in the deformation of oblate drops. Thus, the current experiment serves to explore the behavior of drop deformation beyond the limit of numerical simulations.

The experiments were performed with two types of fluids. Pale 1000 oil was used as the suspending fluid while various grades of Dow Corning 200 silicone fluid were used as the drop phase. These fluids were chosen so that the Reynolds number was small (to approximate the creeping flow limit of the numerical studies) and the capillary number in a range such that modestly deformed drops are unstable as found in Chapter 1 (*i.e.*, $1 < Ca < 5.5$).

The basic results of the experiments echoed those of the numerical studies. We found experimentally that the critical value of the capillary number increases monotonically as the degree of initial deformation is decreased. Furthermore, the experiments showed that for an initially unstable prolate drop, a tail was formed which eventually broke off from the parent drop. For the oblate case, a cavity was formed at the back of the drop as predicted by the numerical simulation. As the drop translated, the cavity became longer and narrower, and evolved into a skirt-like structure. Then, the bottom of the drop closed up on itself and eventually, the top portion of the drop broke off and multiple double-emulsion drops were formed.

From this study, the most remarkable result is that all the qualitative behavior of drop deformation discovered in the numerical studies (for perfect ellipsoids) is preserved in the experiments. This shows that the details of the initial drop shape play a very minor role in the drop deformation; only the overall shape (whether

prolate or oblate) determines the general behavior of an initially nonspherical drop as it translates.

In Chapter 3, we demonstrated that an adaptation of the well-known Laser Doppler Anemometry can be utilized to measure the particle velocity and concentration in a suspension flow through a rectangular channel. The key element in this experimental technique is that the refractive indices of the liquid and particulate phases are closely matched to reduce the optical turbidity of the suspension. Since we are interested in studying neutrally buoyant suspensions, a 3-component (1-chloronaphthalene, 1-methylnaphthalene and UCON oil) fluid mixture is required so that the density and the refractive index can be adjusted independently to match the properties of the solid polystyrene particles. By varying the composition of the fluid mixture, the refractive index of the suspending fluid is adjusted so that the turbidity of the suspension is minimized. Specifically, this is accomplished by performing optical turbidity experiments on bulk samples of the suspension.

We have measured particle velocity and concentration profiles of suspensions flowing through a rectangular channel. This specific geometry (as opposed to, say, a cylindrical tube) is chosen because it simplifies the optical setup of the experiment. Also, this relatively simple geometry can facilitate the interpretation of the experimental results. We have performed experiments for a range of relevant parameters: particle radius-to-gap size ratios ($0.01 < \kappa < 0.057$), particle Reynolds number ($0.002 < Re_p < 0.012$) and bulk particle concentration ($0.1 < \Phi_{\text{bulk}} < 0.3$). The basic observation from the experiment is that the particle velocity profile is blunted near the center of the flow channel. The degree of this blunting increases as either the bulk particle concentration or the particle radius-to-gap size ratio increases. The shape of the velocity profile is found to fit the following empirical formula quite well

$$v_z = v_{z,0}(1 - |x|^b) \quad (4.3)$$

b , the bluntness factor, increases as the velocity profile becomes more blunted. It ranges from about 1.9 to 3.5 for the experimental results reported here; its specific

value depends on both Φ_{bulk} and κ . For the relatively small range of particle Reynold number explored here, the data shows that the bluntness factor remains approximately constant within experimental error.

With respect to the local particle volume fraction, we found that it is generally nonuniform across the flow channel. Specifically, we find that the particles tend to concentrate near the center of the channel. In fact, it is observed that for the case of $\Phi_{\text{bulk}} = 0.3$, the particle volume fraction at the center approaches a value near 0.6. This particle volume fraction is approximately the maximum packing value, so that the particles are almost as close to each other as possible (the specific value of maximum packing depends on the way the particles are arranged; for example, it varies from 0.52 for a simple cubic structure to 0.74 for a hexagonal close pack).

We have also calculated the particle volumetric flowrate, Q_p , and compared it with the quantity $\Phi_{\text{bulk}}Q$. This latter quantity is the particle volumetric flowrate if the particles are uniformly distributed in the flow channel and the fluid velocity is identical to the particle velocity (*i.e.*, the slip velocity vanishes). The most interesting result from this comparison is that the the ratio $Q_p/\Phi_{\text{bulk}}Q$ can be significantly less than unity (as low as about 0.6). This means that the particles are moving, on the average, slower than the fluid and consequently, there must be a relatively large slip velocity between the particles and the fluid.

Finally, we have compared our experimental data with theoretical velocity and particle concentration profiles predicted by the shear-induced particle migration theory of Leighton and Acrivos (*cf.* Section 3.6). Quantitatively speaking, the theoretical prediction does not agree with the experimental data very well. As we have explained above, we found that there is a significant slip velocity between the particle and fluid. On the other hand, the theory assumes that the suspension can be treated as a Generalized Newtonian fluid and makes no distinction between particle and fluid velocities. However, it should be pointed out that the theory does predict a blunted velocity profile that becomes more blunted as the bulk particle concentration is increased, as qualitatively found in the experiment.

Comparison of the concentration profiles also shows that there is quantitative difference between the theoretical prediction and the experimental data. Although the theoretical concentration profiles also have a maximum at the center of the flow channel, as found in the experiment, it is shown that the theory predicts that Φ at the centerline always equals the maximum possible value, $\Phi_m = 0.68$. This effect is a manifestation of the assumption that the particles are mathematical points. By taking into account the finite dimensions of the particles, this artifact of the theory can be eliminated and the comparison with the experimental data should be improved.